EXPLORING THE SELF ASSEMBLY OF CADMIUM SELENIDE NANOPARTICLES IN LANGMUIR BLODGETT FILMS

by

Alexander John Giles

A dissertation submitted to the faculty of
The University of North Carolina at Charlotte
in partial fulfillment of the requirements
for the degree of Doctor of Philosophy in
Nanoscale Science

Charlotte

2013

Approved by:

_____
Dr. Edward Stokes

_____
Dr. Jordan Poler

_____
Dr. Stuart Smith

_____
Dr. Marcus Jones

_____
Dr. Faramarz Farahi

ABSTRACT

ALEXANDER JOHN GILES. Engineering quantum dot solids through self assembly in langmuir blodgett films. (Under the direction of DR. EDWARD STOKES)

The assembly of semiconductor nanocrystals into close packed films suitable for device engineering is critical to the development of next generation electronic and optoelectronic devices. These nanocrystals have nanometer dimensions and can be prepared by wet-chemical methods with tremendous control over their size and morphology. Thus far, limited techniques exist for the effective formation and deposition of single monolayer, large area films desired for advanced devices.

Such nanocrystal monolayers have been studied in this work with a Langmuir film trough. The Langmuir trough is a large (6 L) PTFE vessel filled with ultrapure water which nanoparticles can be spread onto. This technique exploits the nanocrystal stability at the air-water interface and controls the average interparticle spacing by varying the surface area available to the nanocrystal solution spread on the surface. The trough has been modified to perform both Langmuir Blodgett (vertical substrate) and Langmuir Schaffer (horizontal substrate) depositions. In addition to varying substrate orientation, film morphologies at varying surface pressures, subphase iconicity, and compression cycles were investigated. Both vertically and horizontally conductive devices were fabricated with sputter deposition and electron beam evaporation processes, with photolithographic techniques employed to write patterns for such devices. Furthermore, an atomic layer deposition system was constructed and developed to deposit current blocking layers in such devices.

Initial Langmuir isotherms exhibited collapse pressures at low pressures (30 mN/m) and extremely low coverage (0.001-0.005 monolayers), which was discovered to be a result of large quantities of unbound ligand in the nanocrystal spreading solution. Methods were developed to reduce the excess ligand concentration and nanocrystal films were realized at pressures as high as 55 mN/m and coverages above 0.1 monolayers. Devices showed both Schottky behavior with high resistivities (10^{5}-10^{9} Ωcm) as well as Ohmic behavior at lower resistivities (10^{-1} Ωcm), suggesting shorting due to insufficient film coverage.

While morphology remains a concern, methods were developed to produce robust, rigid nanocrystal films on air-water interfaces and transfer them onto conductive substrates. Understanding of the particle-particle and particle-substrate interactions allowed for efficient preparation of substrates and spreading solutions, improving both film quality and throughput.

DEDICATION

I dedicate this dissertation to my wonderful grandmothers, Phyllis Endicott and Mary Giles. Without their support this work would not have been possible.

ACKNOWLEDGMENTS

I would first like to acknowledge my advisor, Dr. Edward Stokes. Dr. Stokes took me on as a mentee soon after I began the graduate program at UNC Charlotte and has been a source of knowledge and support ever since. His expertise working in both industrial and academic environments has been invaluable to me, not just with my efforts toward this dissertation, but with my career development and ambitions after graduate school. I would not have the opportunities I have now without Dr. Stokes guidance and for that I am very grateful. I would also like to acknowledge Dr. Jordan Poler, who served as an instructor for a class I took as a first year graduate student and has acted as a mentor ever since. Dr. Poler's knowledge base and passion for understanding is something I always have and always will look up to. Furthermore, I would like to recognize Dr. Faramarz Farahi, who I was fortunate enough to work on a start up effort that aimed to commercialize technology developed at UNC Charlotte. Dr. Farahi's guidance and expertise afforded me a learning experience not found in a traditional classroom or laboratory and for that I am extremely grateful. I would also like to recognize the members of my dissertation committee for taking the time out of their schedules to serve in this capacity.

I would like to thank the enormous support provided to me by the Optics Center at UNC Charlotte, where much of the fabrication and characterization work for this dissertation was completed. Robert Hudgins, Lou Deguzman and Scott Williams all were extremely helpful in acquiring both the tools and the knowledge to carry out many of these experiments, this work would not have been possible without them. I would like to thank Jennifer Pagan, Kinnari Patel and Paolo Batoni of Dot Metrics Technologies, Inc,

for many enlightening technical conversations and encouragement. I would also like to thank all the graduate students I've had the pleasure of working with. Mike Forney, Sharonda Johnson, Ying Li, Kien Ly and others have provided valuable insights and assistance to me during the course of this research. Lastly, many materials used in this study were prepared by Dr. Marcus Jones' research group, particularly Scott Williams and Drew Tobias. Without their efforts much of this work would not have been possible and for that I am grateful.

I would like to thank Caroline Kennedy and Robin Burns for helping me through the daunting process of graduate school. I am eternally grateful for the funding support provided to me by the Chemistry department and am particularly grateful to Dr. Bernadette Donovan-Merkert's tireless efforts to secure such funding.

I would like to thank my wonderful girlfriend Caresse Duford who has encouraged and supported me throughout this process, patiently listening to my frustrations and waiting up for me on those late nights in the lab.

I would like to thank my family for their unbelievable support and encouragement. My brother, Jeremy Giles has always been there for a conversation and a laugh, sometimes much needed during my graduate career. Most importantly I would like to thank my parents, Thomas and Melissa Giles, who have inspired me with a thirst for knowledge from an early age. I never would have come this far without them and their undying encouragement.

TABLE OF CONTENTS

LIST OF TABLES

LIST OF FIGURES

LIST OF ABBREVIATIONS

ASTM	American society for testing and materials
AFM	atomic force microscopy
ALD	atomic layer deposition
BZ	brillouin zone
DI	deionized
DOS	density of states
DNQ	diazonaphthoquinone
fpm	feet per minute
FW	formula weight
HSAB	hard-soft acid-base
HDA	hexadecylamine
HDMS	hexamethyldisilazane
HOMO	highest occupied molecular orbital
ITO	indium tin oxide
ICP-AES	inductively coupled plasma - atomic electron spectroscopy
IR	infrared
LB	Langmuir Blodgett
LS	Langmuir Schaffer
LbL	layer by layer
LED	light emitting diode
LMA	limiting molecular area

LCD	liquid crystal display
LUMO	lowest unoccupied molecular orbital
MIT	Massachusetts Institute of Technology
MMA	mean molecular area
mph	miles per hour
NMP	n-methyl-2-pyrrolidone
TPD	n,n'-diphenyl-n,n'-di(o-tolyl) benzide
NC	nanocrystal
NIH	national institutes of health
NN	nearest neighbor
OA	oleic acid
PFA	perfluoroalfoxy
PPEI	perylene bis(phenethylimide)
PL	photoluminescence
PV	photovoltaic
POM	polyoxymethylene
PTFE	polytetrafluoroethylene
PMA	predicted molecular area
QD	quantum dot
SEM	scanning electron microscopy
TB	tight binding
TEM	transmission electron microscopy
TMA	trimethylaluminum

TOPO	trioctylphosphine oxide
UV	ultraviolet
ZnOOEP	zinc octakis(octyloxyethyl) polyphyrin

CHAPTER 1: INTRODUCTION

Semiconductor nanocrystals, commonly known as quantum dots (QDs) have been an active area of research for the past three decades. Semiconductors are macroscopic "molecules" in a sense, as their electronic properties arise from the coupling of individual atomic orbitals of closely spaced, ordered atoms in a lattice. This electronic coupling of atoms results in the formation of coherent energy bands, as are present in all covalent solids. Semiconductors possess a relatively low energy gap in their band structure, located between a full valence band and empty conduction band. This region has a density of states of zero (neglecting defects and other trap sites) where no allowed electronic states exist. Electronic activity across the band gap may involve a photon, this photon-electron interaction is the basis of optoelectronics. Because bulk semiconductors have so many atoms however, a change in the total number of atoms has no effect on the electronic bands provided the material remains larger than a minimum size. This is largely a good thing, as engineers can rely on constant electronic properties of a material regardless of shape or size. The downside to this is that with bulk semiconductors, engineers and scientists are somewhat limited in what materials they can use for a specific application. In contrast, nanostructured semiconductors have very few atoms (generally $< 10^4$) and adding or removing even a single atom will appreciably change the electronic structure. Nanocrystals with fewer atoms have more strongly confined charge carriers, which results in a more widely spaced the band gap, approaching the limit of a

single atom's highest occupied molecular orbital (HOMO) to lowest unoccupied molecular orbital (LUMO) transition. As these nanocrystals are nucleated and grown in solution, their size is simply a function of their growth time. With tightly controlled variables and an experienced chemist the entire visible spectrum and much of the NIR can be synthesized with only a few materials (ZnSe, CdSe, PbSe for example) in a matter of days or even hours. In optoelectronics this notion of nanoscale band gap engineering has been a paradigm shift in the last decade.

As size decreases, the ratio of surface atoms to interior atoms increases drastically. Surface atoms have, by definition, unfilled valence shells that may form covalent bonds with foreign atoms. These bonds often introduce carrier trap states within the nanocrystal, which can inhibit performance. This has largely been addressed by functionalizing the surfaces of QDs with organic ligands. These ligands typically have energy levels far outside of the NC band gap, electrically passivating the NC. Furthermore, the aliphatic and sterically large nature of many (not all) of these ligands renders the nanocrystal soluble in a variety of non-polar solvents. Once nanocrystals are cast into a film however, the nature of the ligand poses a huge problem for the same reasons it was previously effective: The scarcity of available states near the NC band edge creates a large potential barrier for electrons moving from one NC to another; and the size of many of these ligands results in huge interparticle distances (typically of the order of the size of the NC itself). Large distances and high potential barriers result in very low tunneling (hopping) rates and the electron transport properties of NC films are very poor.

There are numerous methods to fabricate devices from these nanomaterials, most of which rely on self assembly.[1] Researchers have demonstrated ordered, three dimensional superlattices[2], glassy spin cast films[3], layer-by-layer (LbL) monolayer deposition[4] and other techniques to achieve similar goals. A major consideration of any technique is the interparticle spacing, which is important not only in the self assembly but also a critical aspect of the final properties of any nanocrystal solid.[5] Reduced inter-particle distances are currently achieved via chemical methods, by exchanging the passivating ligands on the nanoparticle surface. Two dimensional nanoparticle films can also be formed using a Langmuir film trough. This has been shown to be feasible by several groups,[6-9] although using this technique to fabricate working devices has thus far been elusive.

This work seeks to address the difficultly in fabricating closely packed nanocrystal films by exploiting the Langmuir technique, highlight recent advances in the field and build on those to create a nanocrystal solid to be used in a device. Deposition techniques and electronic properties of these materials will be discussed, with a focus on which parameters are important to consider when fabricating devices, the goal of this research.

CHAPTER 2: SEMICONDUCTOR NANOCRYSTALS

2.1 Background and Theory

To understand the electronics of nanostructed systems, it is critical to recognize the distinction between traditional (bulk) semiconductor physics, where carriers behave as if they were essentially free (in most inorganic materials), and confined or molecular systems where carriers are electrostatically bound to one another (in most organic materials) Given the opposing charges on each carrier, the electron is attracted to the hole by the Coulomb potential energy $\frac{-e^2}{\varepsilon r}$ [2.1][12], where e the the charge on the electron, r is distance and ε is the permitivitty. In these excitonic systems (unlike the free carrier model) we see no net flow of charge (current) as carriers move about in the crystal, an important and fundamental difference from traditional (bulk) solar cell photophysics.

Frenkel and Peierls were the first two introduce this concept in 1931 and 1932, respectively, when studying how light energy is absorbed by solids (such as $Xe_{(s)}$ and $NaCl_{(s)}$). It is important to note that Frankel studied excitons in insulating solids where the dielectric constant is quite small compared to a semiconductor (or organic molecule), resulting in a significantly higher Coulombic energy (eq. 2.1) than their semiconductor counterparts. Furthermore, in the insulating solids studied by Frankel and Peierls, the radius of the lowest energy exciton is often comparable (or less) to the interatomic distance resulting in a somewhat localized exciton. These charge pairs form a class known as ‘Frankel’ excitons, tightly bound and localized within the crystal.

Realizing the limitations of Frenkel's approach, Mott and Wannier investigated the case of an exciton in a solid with delocalized valence electrons (i.e. Si, Ge, GaAs). As most semiconductors have a much higher density of states than ionic solids, we can see that the ionic solids merely represent a limiting case, one where the valence band is narrow and the bandgap is large. Mott showed that excitons in a covalent solid experience a much larger dielectric constant and therefore a much weaker Coulombic attraction (see eq. 2.1). The radii of these excitons are large, often covering hundreds of atomic sites. This concept of an exciton 'radius' is central to nanostructures, where an exciton is created in a particle smaller (in at least one dimension) than the excitonic radius, predictably and controllably increasing the exciton's energy gap. Using Bohr's quantum theory we arrive at a formula for the energy of the excitonic series: $E_n = E_\infty - \frac{R}{n^2}$ [2.2] where $n =$ 1,2,3 ...; and $R = \frac{m^* e^4}{2h^2\varepsilon^2}$ [2.3][12, 13], where m* is the reduced exciton mass and h is planck's constant. The excitonic series (eq. 2.2) can be seen in absorption measurements of semiconductors at low temperatures (figure 2.1). It should be noted that figure 2.1 is merely a cartoon of an *ideal* measurement at very low temperatures. As we increase T, the values of E_n are modified by the increasing vibration motion of the atoms within the crystal, spreading the excitonic absorption peaks considerably. Plugging the values for Silicon (ε_{Si} = 11.68, m_x*= 0.38 m_o)[10, 14] we can see that the predicted exciton binding energy in Silicon is on the order of the room temperature value of kT (≈ 25 meV) and therefore is too broad to be observed. In fact, this phenomenon is seen in nearly all inorganic bulk semiconductors at room temperature: The exciton binding energy is of the same order as kT and excitons are easily ionized to produce free carriers. This explains the photoconductivity seen in semiconductors: As light is absorbed, an exciton is formed

and then thermally ionized to produce free carriers, which lower the resistivity of the material.

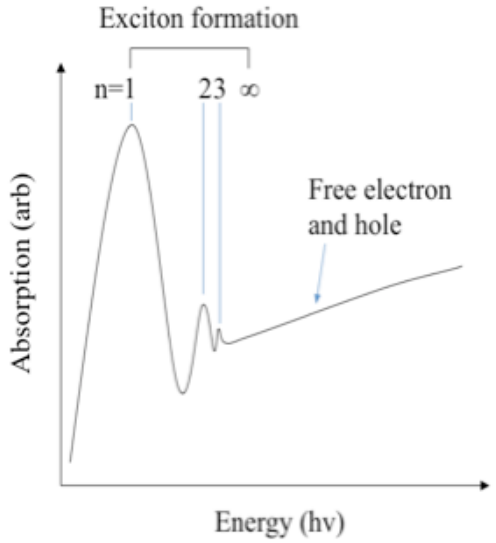

Figure 2.1: Expected absorption profile of an ideal semiconductor at low T. Strong absorption peaks at low energy are due to Mott excitons, while continuum behavior is seen at higher energies due to free carriers.

In materials with dimensions smaller than the excitonic radius, several interesting phenomena occur. The previously delocalized exciton (Mott-like) is now confined in one or more dimensions and thus behaves as a localized exciton (Frenkel-like)[15, 16]. Furthermore the Coulomb attraction increases as the inverse of the radius (eq. 2.2), blue shifting the 1st excitonic absorption energy as the dimensions are decreased. In addition to the Coulombic contribution, quantum effects and solvation energy loss must be accounted for in confined systems. In a seminal work , Brus et al. proposed the following relationship for excitonic energies:[11]

$$E_x = \frac{h^2}{8m_0R^2}\left(\frac{1}{m_e^*}+\frac{1}{m_h^*}\right) - \frac{1.8e^2}{4\pi\varepsilon_0\varepsilon_r R} + \frac{(-0.248)4\pi^2e^4m_0}{(4\pi\varepsilon_0\varepsilon_r)^2h^2\left(\frac{1}{m_e^*}+\frac{1}{m_h^*}\right)} \quad [2.4]$$

Where ε_o and ε_r are the absolute and relative permitivitties, respectively; R is the nanoparticle radius; m_o, is the electron rest mass; and m^*_e, and m^*_h are the reduced exciton, electron and hole masses, respectively.

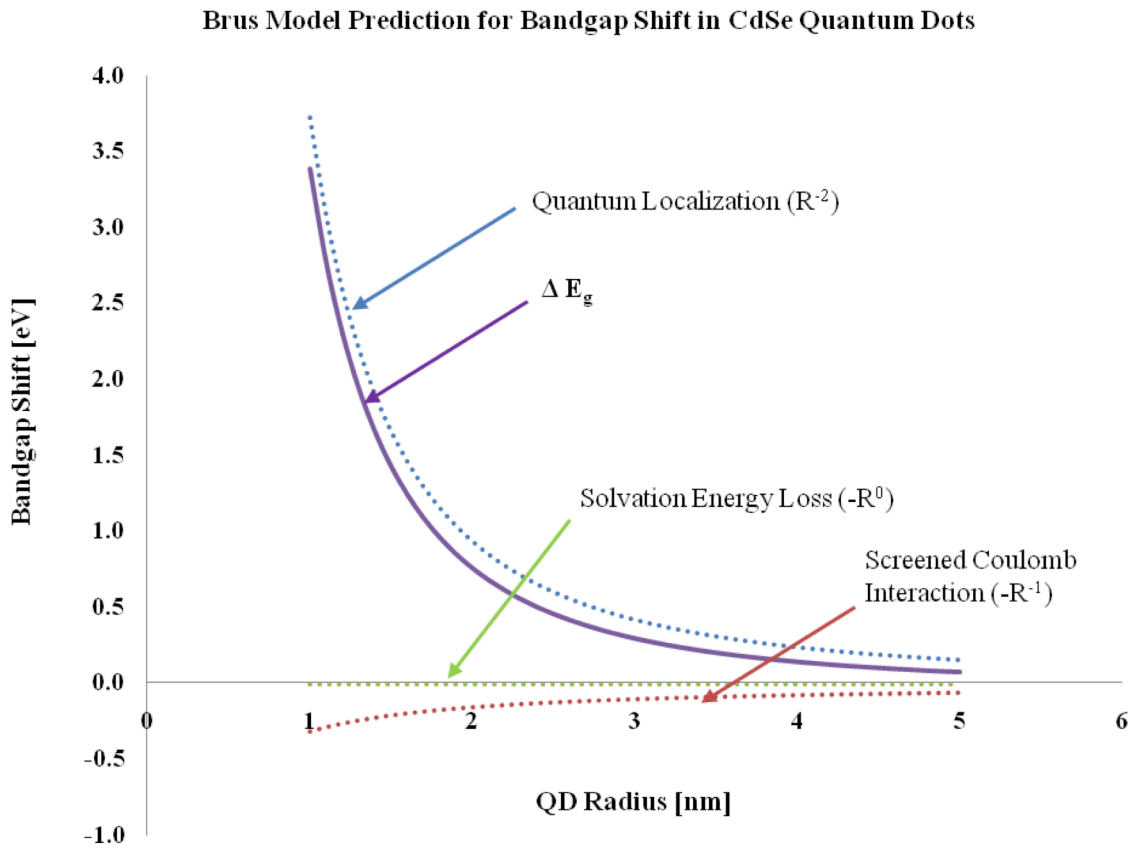

Figure 2.2: Plot of the Brus et al. relationship[1b] (equation 2.4, ΔE_g) and individual terms: Quantum localization (first term), screened Coulomb interaction (second term), and solvation energy loss (third term.

In this model we can relatively easily assign a physical meaning to each term. The first term on the right hand side represents the quantum energy of localization (the kinetic term), which shifts $E_x(R)$ to higher energies as R^{-2}. The second term represents the Coulomb attraction, accounting for the screened electromagnetic attraction between the electron and hole, shifting $E_x(R)$ to lower energies as R^{-1}. The third (size independent) term is the solvation energy loss, which is quite small in semiconductors. More than a decade after Brus proposed his model researchers began synthesizing quantum dots in the liquid phase, allowing for widespread characterization and study.[17, 18] The model has been successful in predicting behavior experimentally for several decades, even in complex heterostructures.[19] While it does not exactly predict the band gap shifts (tends to overestimate) for nanocrystals, it provides a useful model and identifies important parameters (dielectric constant, effective) when considering different types of QDs. A more accurate model for predicting bandgaps in CdSe particles was proposed by Yu et al. which expresses the diameter of a dot as a quartic function of the first exciton absorption peak. The empirical formula is: [20]

$$D = (1.6122 * 10^{-9})\lambda^4 - (2.6575 * 10^{-6})\lambda^3 + (1.6242 * 10^{-3})\lambda^2 - (0.4277)\lambda + 41.57 \quad [2.5]$$

Where D is the particle diameter and λ is the peak wavelength of the first exciton absorption.

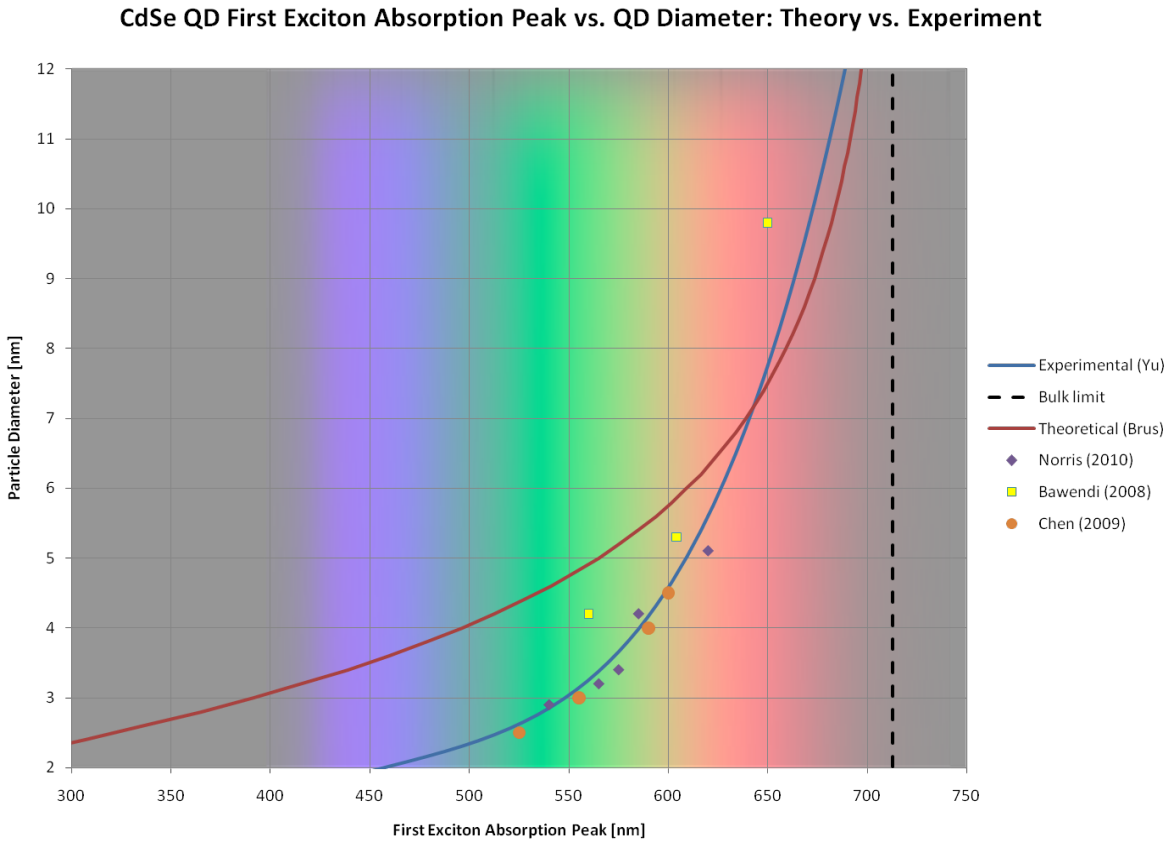

Figure 2.3: Plot of first exciton absorption peak vs. particle diameter in CdSe nanocrystals. Solid lines are models proposed by Brus et al. (theoretical, 1983)[11] and Yu et al. (empirical, 2003)[20] . Data points show improved accuracy of Yu's theory[21].

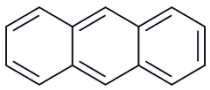

Figure 2.4: Anthracene structure ($C_{14}H_{10}$)

Because of these higher energies in confined systems, absorption of a sufficiently energetic photon results in a transiently localized excited state that cannot thermally

dissociate ($E_x >> kT$).[16] This yields a fundamentally different method of photovoltaic phenomena which cannot be described by p-n junction theory. The first report of a excitonic photovoltaic device was in 1959 by Kallman and Pope,[22] using an anthracene ($C_{14}H_{10}$,) crystal separating two solutions of NaCl.

Kallman found that by illuminating one side of the anthracene crystal (5 μm thick), a photovoltage of 200 mV was generated between the two solutions. When the other side was illuminated, the same 200 mV was observed with opposite polarity (the illuminated side always charged negative). While they were not able to propose a mechanism at the time, further experiments led them to conclude that the majority of the photocurrent was due to (1) the creation of excitons at the illuminated interface and (2) favorable electron injection (vs. hole injection) into the electrolyte.[16, 22-24] Unfortunately, these studies went nearly unnoticed. A modified version of this experiment was conducted in 1989 by Gregg et al.[25] with zinc octakis(octyloxyethyl) polyphyrin (ZnOOEP) as the absorber and ITO as the electrodes. The cell was symmetrical, the liquid crystal was isotropic and was contacted by identical electrodes, hence there could be no electric field present nor a built in voltage ($V_{bi} = 0$). Traditional p-n junction theory suggests that the open circuit voltage is less than the built in voltage ($V_{OC} < V_{bi}$), and that we would not expect this cell to have any photovoltaic response. The cell produced a strong photovoltaic response however, with $V_{OC} = -0.3V$ and $I_{SC} = 0.3$ mA/cm^{-2}.[25] This work, building on Kallman and Pope's models, was explained with a purely kinetic model: Light was incident on only one side of this device (2-5 μm thick), hence excitons are produced on only one side of the electrode. Furthermore, exciton dissociation at the interface must be kinetically asymmetric, and one type of carrier must

be more favorably injected than the other. In this case (and also in the Kallman experiments) electrons are the more favorably injected carriers. With only those two assumptions, the operation of the cell can be explained. As electrons are injected into the electrode however, an electric field would build up that opposed further charge separation, inhibiting current. This is in fact what happens under open circuit conditions: electron injection into the electrode creates an electric field that inhibits further current flow. We can express the local electric field in this excitonic PV cell as $E = qV_{OC}$ [2.6],[16, 25] where q is the electron charge. If this kinetic model is correct, one would expect further "encourage" or "discourage" carrier injection by using carrier selective contacts, *N,N'*-diphenyl-*N,N'*-di(o-tolyl)benzidine (TPD) is a well known hole conductor with its HOMO level in between perylene bis(phenylethylimide)'s (PPEI) HOMO and the work function of ITO. Its LUMO level however, is well above the LUMO of PPEI and the work function of ITO. This facilitates rapid hole transport from the PPEI into the ITO, while forcing electrons to tunnel through the TPD to get to the ITO contact. These hole selective contacts have been shown to enhance photovoltaic response in films where they are applied to the majority hole-diffusing side of the excitonic material by discouraging electron diffusion into the (electro-positive) ITO contact. When a hole diffusing contact is applied to a majority electron diffusing side it has been shown to reverse the polarity of the device, forcing electrons to diffuse on the opposite side (the In contact in this case). These contacts are typically only a few nm thick and do not pose a significant absorption threat. Furthermore these selective contacts are organic molecules and can be depositied without damaging the underlying QD film, a problem we have

previously had trying to grow (epitaxially) inorganic semiconductors onto deposited QD films.

The enormous tunability of a quantum dot provides a very attractive "building block" for designing optoelectronic devices in both the emitting and detecting arenas. By controlling the size and spacing of these "artificial atoms," we can control luminescence, absorption, coupling, carrier transport properties and more. These benefits however, come at a cost. A bulk semiconductor consists of anywhere between 10^{10} to 10^{30} atoms, of which interior atoms far outnumber those on the surface. In a quantum dot however, many of the atoms are on the surface, giving rise to large density of surface traps. It is critical to passivate these surface atoms to prevent mid gap states and non-radiative recombination pathways. This is accomplished with either an organic ligand shell or a wide band gap inorganic shell. The inorganic shell (CdSe(ZnS) for example) provides for excellent electronic passivation, confining carriers to the core with a type-I ("straddling gap") heterojunction. This results in significant overlap between the electron and hole wavefunctions, resulting in high rates of radiative recombination and quantum yields near unity.[15, 27-30] While this is a desirable condition for emitters (LEDs, lasers, etc), detectors (solar cells, photosensors) require that carriers be separated and used in an external circuit before they have an opportunity to recombine within the QD. Furthermore, a passivating shell creates a potential barrier for a carrier at the band edge. Significant effort has been spent on minimizing this potential barrier as a method of demonstrating stronger electron coupling and efficient charge transport between neighboring quantum dots.[15, 16, 28, 29, 31-33] Many groups have explored functionalizing CdSe QDs with either oxidizing[34] or reducing[35] ligands, demonstrating ultrafast exciton

dissociation lifetimes on the order of 1ps, several orders of magnitude faster than the competing radiative recombination lifetimes. Another technique explored by researchers is coupling QDs to wide bandgap semiconductors (i.e. ZnO, TiO_2) in an effort to capture lower energy photons for which the wide bandgap material would otherwise be transparent.[10, 28, 36, 37] This is primarily accomplished by engineering the QD-TiO_2 interface with bifunctional ligands. Applying Pearson's hard-soft acid-base theory[38] (HSAB), we can identify function groups that will more readily react with different materials. The theory states that "soft" acids will react faster and form stronger bonds with "soft bases," while "hard" acids will preferentially interact with "hard" bases. Cd^{2+} and Se^{2-} are considered "soft" ions, and will form bonds more favorably with other "soft" ions (thiols, amines, phosphine oxides) than with "hard" ions (carboxylics)[10]. Exploiting this phenomenon, researchers have used a HS-R-COOH ligand (mercaptopropionic acid in one instance) to couple CdSe QDs to a TiO_2 surface without aggregation of the QDs pre-adsorption.[37] While these bifunctional ligands are very effective at physically coupling QD to other materials, the electronic coupling remains weak. While the sp^3 hybridization is an understandably poor conductor, efforts to use organic ligands with sp^2 hybridization (mainly heterocyclic compounds: pyridine, thiophene, thiophene thiol, etc.) have yet to demonstrate themselves as efficient charge transport pathways. Furthermore, these sensitization techniques require a electrolytic solution in contact with a counter electrode to maintain charge neutrality within the QDs. Unlike bulk semiconductors, QDs are very sensitive to single electron addition / subtraction and will exhibit drastically different electronic properties in the +1 or -1 charge state. This results from a combination of electron-electron repulsion in a small volume ($F_{Coulomb} \rightarrow \infty$ as $r \rightarrow 0$) and

a discretization of energy levels at the band edge. These electrolytic solutions (I/I_3, Na_2S/S, etc) have their own exciton dissociation lifetimes and can be the limiting rate in the charge transfer reaction. It is becoming more apparent that the most critical factor in maximizing charge transport from a QD to another material (another QD, substrate, etc) is the interdot distance. While the electronic nature of the ligand and dielectric constant of the surrounding medium certainly play a role, minimizing the dot-dot distance is critical.

2.2 The Ligand Shell

CdSe QDs synthesized via the hot-injection method pioneered by Murray, Norris and Bawendi[18] are functionalized with tri-octyl phosphine oxide (TOPO) ligands. The phosphine oxide group binds strongly (via the oxygen) to the Cd sites, while the bulky, saturated octyl tails have a large steric hindrance, repelling foreign molecules.[10] While these TOPO ligands do an excellent job controlling growth and physically protecting the QD surface from attack, they reasonably poor electronic passivators, as their large footprint prevents them from passivating every surface site, leaving large numbers of surface traps. Recently, researchers have explored a variety of ligands in an effort to better understand the effect they have on the QD's electronic nature,[10, 13, 16, 19, 27, 29-31, 37, 39-48] yielding experimental evidence suggesting that a sterically small ligand is advantageous for two reasons: As mentioned before, reducing the inter-dot spacing is the single most important factor in promoting efficient inter-dot charge transport. The inter-dot spacing is a direct function of the length of the ligand, therefore smaller ligands will allow for more closely spaced QDs. Secondly, smaller ligands will load on the QD surface more densely than larger ligands. This allows for better electronic passivation, as

there are fewer un-bonded surface atoms and thus fewer surface traps. Additionally, this higher loading density creates more highly absorbing films as the density of CdSe per unit area is increased. Chen, et al. showed a 1.7x increase in optical density after replacing TOPO ligands with oleic acid (OA) ligands on 3 nm CdSe QDs[10] (figure 2.4). OA and TOPO have similar molar extinction coefficients and OA and TOPO capped QDs have similar inter-dot spacing, so the increase in optical absorption is purely a function of increased loading on the QD surface. Exploiting this idea, Talapin et al. have demonstrated hydrazine (N_2H_4) as an effective ligand to both electronically passivate QDs and decrease inter-dot spacing in QD films.[47] The hydrazine ligands, which adopt a Gauche conformation, (figure 2.5) are the simplest diamines, with two amino groups directly bonded to each other (no carbon atoms). Hydrazine is Brönsted base that binds weakly

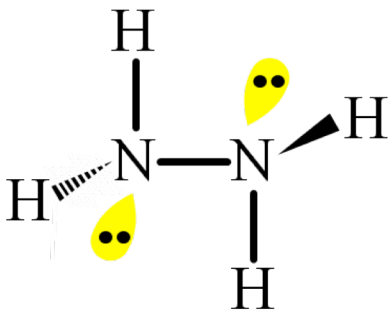

Figure 2.5: Hydrazine molecule showing Gauche conformation and lone electron pairs

(~100 kJ/mol)[46] to CdSe nanocrystals, while also a strong Lewis base with lone pairs of electrons that saturate dangling bonds at the nanocrystals surface. Because of its reductive nature, hydrazine has been shown to repair oxidized Se sites (demonstrated in a

PbSe system)[49], reducing/ eliminating any mid gap levels, in addition to functioning as a charge transfer n-type "dopant," observed in PbSe nanowires[47] and carbon nanotubes[50].

Schapotschinov et al. has done recent work on the binding characteristics of amines, thiols, thiolates, phosphines and phosphine oxides using molecular dynamics and Monte Carlo simulations[46]. Binding energies for TOPO-CdSe (313.6 kJ/mol) are significantly stronger than binding energies for RNH_2-CdSe (86.8 kJ/mol), consistent with HSAB theory[38] as the soft "-PO" functional group binds strongly to soft CdSe while the hard "-NH_2" group is weakly interacting. Furthermore, TOPO has a large steric hindrance, repelling foreign molecules such as hydrazine. To realize a hydrazine exchange on TOPO capped CdSe QDs, we must expect a low rate of ligand exchange. As there are no reports of direct exchanges from TOPO capped CdSe QDs to hydrazine capped QDs, we intend to pursue a two-pronged strategy: Initially we will perform a ligand swap from TOPO to oleic acid (OA) in solution, a straightforward and common procedure outlined as follows:

Table 2.1: Ligand replacement procedure for TOPO capped CdSe nanocrystals.

1.	Starting from a solution of TOPO-capped CdSe QDs in toluene, add methanol to precipitate QDs from solution.
2.	Centrifuge the sample and discard the supernatant.
3.	Vacuum dry the CdSe QDs.
4.	Dissolve the sample in a solution of oleic acid in toluene.
5.	Sonicate overnight @ 75^{o} C.
6.	Add methanol to precipitate the QDs from solution.
7.	Centrifuge and discard the supernatant
8.	Rinse QDs with methanol, removing excess ligand.
9.	Vacuum dry the CdSe QDs.
10.	Dissolve the sample in toluene.

The above procedure renders the CdSe QDs more susceptible to attack from the hydrazine ligand as the oleic acid ligands are far less bulky than their TOPO counterparts (figure 2.6), while the oleic acid ligands maintain the QDs hydrophobicity and stability in a Langmuir film. Post Langmuir deposition, we will evaluate the effectiveness of the hydrazine treatment on both the OA capped QDs and the original TOPO capes samples. If the samples behave similarly there may be no need for the TOPO-OA ligand swap procedure, but we expect a faster reaction rate with OA capped QDs.

2.3 Nanocrystal Solids

The discretization of energy levels in nanocrystals leads to controllable and predictable properties not only for individual particles, but for coupled systems as well. As nanocrystals have similar discrete energy levels (leading to the pseudonym "artificial atoms"), one would expect interesting properties to arise from solids consisting of a closely coupled ensemble of nanocrystals. Furthermore, the LUMO of a II-VI nanoparticle has no nodal plane (filling the entire nanocrystal), analogous to an "s" orbital in atomic physics, allowing us to apply the same principles to QD solids. Electron occupation is also of importance in these systems as different crystal structures possess different degeneracies (table 2.1). While pseudo-potential, tight-binding and other theoretical approximations tend to overestimate the band gap shift due to quantum

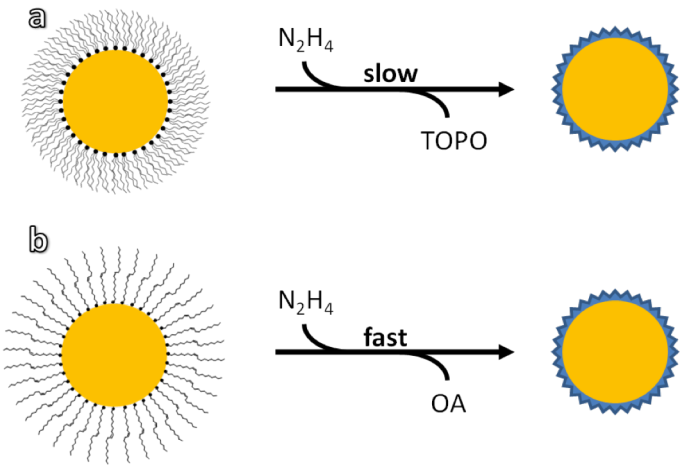

Figure 2.6: (a) A cartoon of a TOPO capped QD, showing the steric hindrance provided by the tertiary alkyl groups. (b) A cartoon of a OA capped QD, showing the more accessible QD surface. In ligand exchange reactions, (b) will have a faster rate constant as the OA capped surface is more susceptible to attack from foreign molecules.

confinement, all methods agree on the symmetry and degeneracy of the first conduction energy levels.[33]

How nanoparticles are arranged in a solid is obviously of great concern. While the artificial atom concept paints a simple and favorable picture, individual nanocrystals are all unique with varying sizes and morphologies, resulting in a far more complex system than a single crystal semiconductor. The size dispersion of the ensemble of QDs, measured by the width of the PL (in solution), is thus a very important parameter in engineering a QD solid. While a size distribution with $\sigma < 5\%$ is generally considered the "gold standard" among synthetic chemists[16, 18, 39], we need to characterize the distribution in terms of the site energy dispersion (QD-QD band offsets). Ideally, an ensemble of QDs used to prepare a solid should have a site energy dispersion less than the available thermal energy in order to allow coherent inter-dot transport (figure 15).

Table 2.2: Degeneracy as function of orbital (s,p,d) and crystal symmetry (wurtzite, rock-salt).

	Wurtzite (CdSe)	Rock Salt (PbSe)
s	2 fold	8 fold
p	6 fold	24 told
d	8 fold	40-fold

Furthermore, if $\Delta\alpha$ is larger than the exchange coupling energy (β, to be discussed in the next section), Anderson localization will dominate[47], inhibiting carrier transport. Figure 16 shows the absorption and photoluminescence spectra of commercially available

QDs (left, Evident Technologies) and QDs synthesized using the Murray method[18]. Even with monodispersities below 5% RMS, significant amounts of QDs will have site energy offsets greater than 26 meV. While this can certainly be improved, this magnitude of site dispersion energy is widely considered acceptable in the literature and improving synthetic methods (in hopes of reducing this energy) will not be a focus of this work.

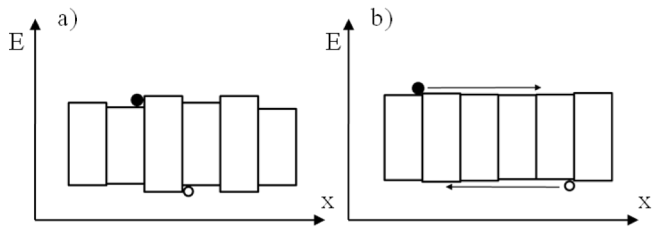

Figure 2.7: a) Band diagram of a QD solid with a large Δα, seen as misaligned energy levels. b) Band diagram of a QD solid with a small Δα, seen as aligned and nearly continuous energy levels.

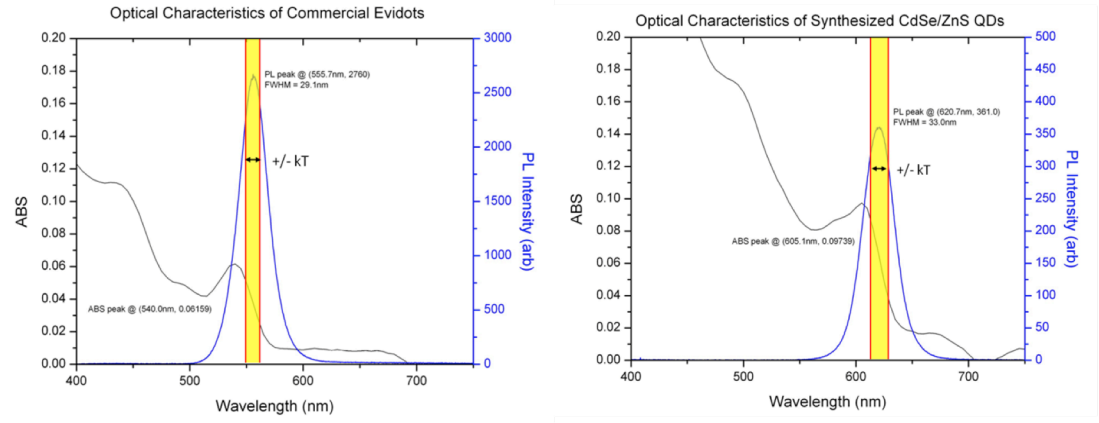

Figure 2.8: Left: Absorption and PL data of commercially purchased CdSe/ZnS QDs (Evident Technologies). Right: Absorption and PL data of in-house synthesized CdSe/ZnS QDs. Highlighted yellow areas represent the range defined by $E_g \pm k_BT$, showing the narrow size distribution required in an effective QD solid.

Arguably the most fundamental property of a high quality nanocrystal solid is the degree to which the particles are electronically coupled to each other. Quantum dots are accurately understood as a physical example of the "particle in a 3-D finite well" problem in quantum mechanics. Brus[11] was one of the first to solve this problem, making an important distinction that differentiates this from the textbook exercise. Solving the Schrodinger equation for a particle in a spherical square well is a straightforward problem with the familiar conditions imposed by quantum mechanics. Traditionally, another condition states that the first derivative of the wave function be continuous at all points, but that assumes a constant carrier effective mass throughout all space, which clearly is not the case for a nanocrystal. Brus, with the suggestions of others, modified the condition to scale for the difference in effective masses of carriers inside and outside the crystal:

$$\frac{1}{m^*}\frac{\partial \psi'}{\partial r} = \frac{1}{m_o}\frac{\partial \psi''}{\partial r}. \qquad [2.8]$$

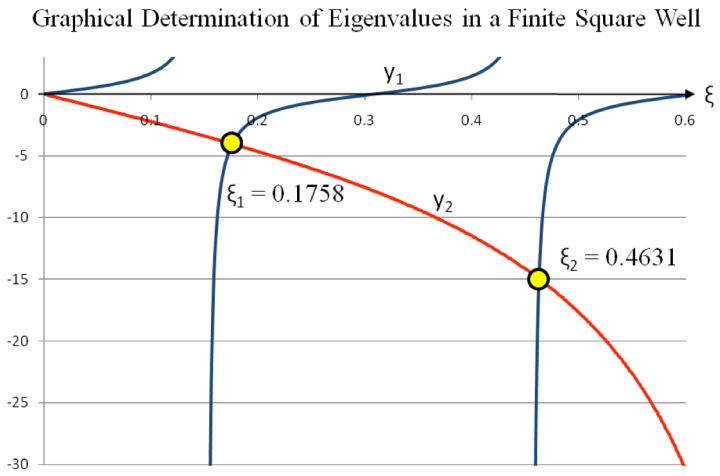

Figure 2.9: Eigenvalues of ξ_n for n=1,2; l=0. R=2.5 nm, V_o=5 eV. Y_1 are Y_2 are described in equation 12.

Where ψ is the electron wavefunction. This correction allowed for accurate modeling of the electron's "leakage" outside of the nanocrystal and yields a set of eigenvalues (figure 17). While many colloidal nanocrystals are engineered to minimize such leakage (namely QDs for use in emitters) to improve quantum efficiency and minimize surface trapping, it is essential for QDs in nanocrystal solids to exhibit this behavior. The bound states in a semiconductor nanocrystal can be determined by finding the values of ξ that satisfy the equation:

$$\tan(x_o\xi) = f_l(x_o, \xi). \qquad [2.9]$$

Where l represents angular momentum and x_o is the unitless "size" of the well:

$$x_o{}^2 = \frac{2mV_oR^2}{\hbar^2}\,. \qquad [2.10]$$

The problem becomes more tedious but no more complex as we consider in the discontinuity due to the effective mass offset (eq. 11), yielding us the S (l=0) eigenfunction:

$$f_o(x_o, \xi) = \frac{x_o\xi}{1-\zeta\left(1-x_o\sqrt{1-\xi^2/\zeta}\right)}\,; \quad [2.11]$$

where $\zeta = m^*/m_o$. The 1S and 2S bound states are thus described by a spherical Bessel function inside the nanocrystal and a spherical Hankel function outside:

$$\psi_o(r) = \frac{A \sin(k_n r)}{r} \qquad r < R; \qquad [2.12]$$

$$\psi_o(r) = \frac{Be^{-\aleph_n r}}{r} \qquad r > R; \qquad [2.13]$$

where k_n and $\aleph_n$ are defined as:

$$k_n = \frac{\sqrt{2mV_o}}{\hbar}\xi_n\,; \qquad [2.14]$$

$$\aleph_n = \frac{\sqrt{2mV_o}}{\hbar}\sqrt{1-\xi_n}\quad . \qquad [2.15]$$

Note that as ξ_n is increased, $\aleph_n$ is actually decreased, resulting in more of the electron's wavefunction existing outside of the nanocrystal. The practical consequence of this is that higher energy states (n > 1) (despite their short lifetimes) will couple far more strongly to both neighboring nanocrystals or underlying substrates or contacts.[11, 51]

A further consideration that is not widely discussed in the literature is the effect of the dielectric constant of the surrounding medium on nanoparticle coupling. This is understood theoretically as the energy loss due to solvation (recall equation 9). Classical electrostatics predicts a dielectric sphere in an infinite dielectric medium will have a loss of solvation energy dependant on both dielectric constants and the size of the sphere.

$$P\ \alpha\ \frac{\epsilon_{out}-1}{\epsilon_{in}R} \quad [2.16]$$

A more rigorous expression of P reveals an expansion that it is dependent on the radial electric field, but we neglect that as it is a weak effect in semiconductor nanocrystals and the above relationship has been understood to be sufficient[11]. We understand the potential barrier at the nanocrystal surface to be:

$$V_o = LUMO_{ligand} - LUMO_{NC} - P. \qquad [2.17]$$

Where As the dielectric value of the surrounding medium (ϵ_{out}) is increased, P is increased proportionately. This reduces the effective potential (V_0) seen by a confined electron, relaxing the confinement and promoting stronger coupling with neighboring nanoparticles or substrates.

As neighboring QDs are brought into close contact with each other their wavefunctions begin to overlap, allowing for charge transfer to occur. As Hankel functions (eq 16) describe the amount of wavefunction leakage, this dependence is highly exponential and considers both QD size and interparticle spacing. Talapin et al.[30] and others suggest an energy scaling of the solid as the exchange coupling energy:

$$\beta \sim e^{[-\kappa(d+\delta)]} \qquad [2.18]$$

Where κ^{-1} describes the length scale of the wave function leakage, d is the diameter of the dot and δ is the interparticle spacing. This relationship is consistent with the overlap integral of adjacent Hankel functions and is somewhat intuitive: the further the wavefunctions extend outside the nanocrystal and the closer together the nanocrystals are, the stronger the electronic coupling will be. Note the exponential term is dimensionless and any consistent unit (i.e. nm, Å) may be used. A further consequence of the increased electronic coupling is the band shift observed in the QD solid. Just as atomic wavefunctions in solids couple to form lower energy bands, similar behavior is observed in QD solids, albeit to a far lesser extent. The tight-binding model, traditionally used to

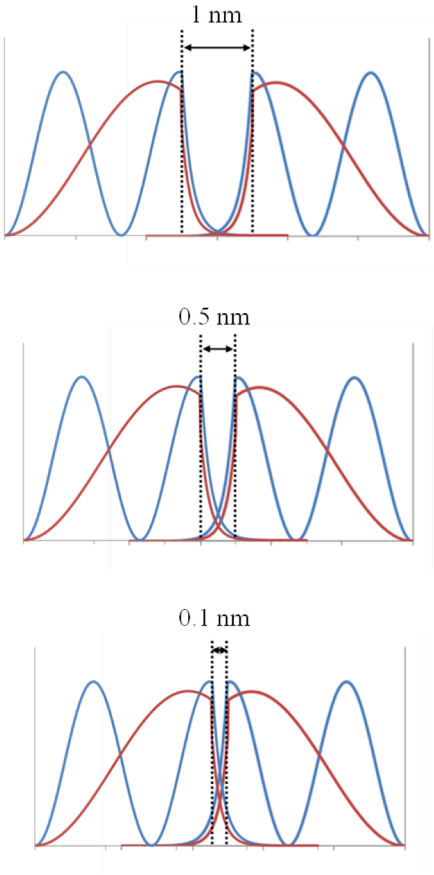

Figure 2.10: Probability distribution of 1S(red) and 2S(blue) electrons in adjacent d=5 nm CdSe QDs with an ε=2 dielectric gap with varying interparticle distances. Numerical values indicate interparticle spacing distance (δ). D=5 nm, V_o=5 eV.

calculate the electronic band structure in solids, can be extended to QD solids as the underlying principles are the same. The TB model is a one-electron that assumes electrons are tightly bound to the atom (or QD in our case) and thus have a limited interaction with surrounding atoms (QDs). The Huckel approximation uses a linear combination of atomic orbitals, superimposing wavefunctions for isolated atoms (QDs) at each site. An important aspect of the TB model is the band broadening that occurs as individual atoms (QDs) are coupled together. Following Gerstein and Smith[52] we determine the Schrödinger equation to be:

$$(E_o - E)A_o + \beta \sum_{n=1}^{Z} A_n = 0; \qquad [2.19]$$

where A_0 is the amplitude on a given site and A_n are the amplitudes on Z neighboring sites, with β defined as the exchange coupling energy (specifically, the off-diagonal (tunneling) matrix elements):

$$\langle 1|H|2\rangle = \beta. \qquad [2.20]$$

Returning to equation 21 we consider the maxima and minima of the Schrodinger equation across the Brillouin zone. As A_n is related to A_o by phase factors, there will be points on the BZ where the sum of these factors is 1 (a maximum) and other points where the sum is -1 (a minimum). Solving for these values yields:

$$E_{max} = E_o + Z\beta \qquad [2.21]$$

$$E_{min} = E_o - Z\beta \qquad [2.22]$$

Elucidating a width of the energy band given by:

$$B = 2Z\beta. \qquad [2.23]$$

This important result tells us that we should expect a reduction in the 1st excitonic absorption peak in strongly coupled films proportional to the number of nearest neighbors (Z) and the exchange coupling energy (β). In a three dimensional close packed QD solid, each nanoparticle has 12 NNs, resulting in a expected redshift of:

$$\Delta E_{3D} = 24\beta \; ; \qquad [2.24]$$

While in a two dimensional solid the number of NNs is 6, yielding:

$$\Delta E_{2D} = 12\beta \; ; \qquad [2.25]$$

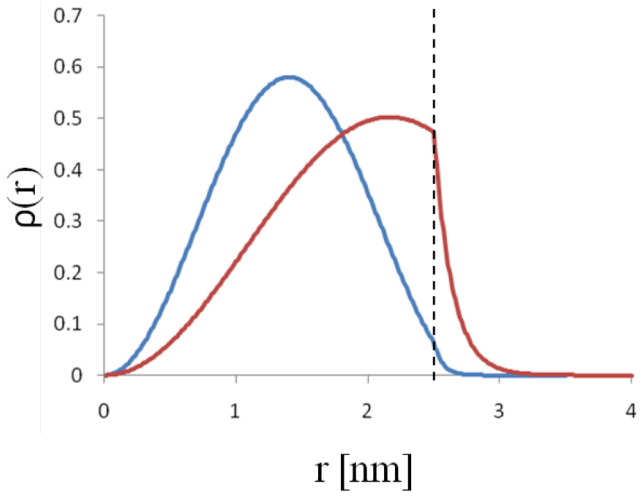

Figure 2.11: Probability distribution for a 1S electron (red) and a 1S hole (blue) in a D = 5 nm CdSe QD. The dotted line shows the boundary between the QD and surrounding medium. Calculated using Brus' methods.[11]

It is important to realize however, that the coupling between electrons and holes is different and depends largely on the effective mass of the carrier. The effective mass of an electron in CdSe is $m_e^* = 0.13m_o$,[53] although values in the literature range from as high as $0.15m_o$ to as low as $0.11m_o$.[51] The values for heavy and light holes are generally agreed upon as $m_{hh}^* = 2.5m_o$ and $m_{lh}^* = 0.45m_o$, respectively[53]. Plugging these effective values into equation 13 yields eigenvalues which show the difference in probability distribution for a 1S electron vs. a 1S hole in a D = 5 nm CdSe nanoparticle (figure 2.18). Of primary important is the stronger confinement of the hole due to its large effective mass. This results in significantly less of the hole's wavefunction existing outside the nanocrystal and therefore much weaker coupling with neighboring particles or substrates. For a 5 nm diameter CdSe QD surrounded by a $V_0 = 5$ eV potential well, the

probability of the electron existing outside the nanocrystal is 15.33 times greater than the probability of the hole existing outside the nanocrystal:

$$\frac{\int_R^\infty r^2 \psi_e^* \psi_e \, dr}{\int_R^\infty r^2 \psi_h^* \psi_h \, dr} = 15.33129, \quad [2.26]$$

seen clearly in figure 2.10. Furthermore, the electron's wavefunction extends much further beyond the boundary than the hole's, promoting stronger coupling at greater distances. This motivates us to understand β as a property of the charge carriers, with different values of β_e and β_h, much like the effective mass property. Assuming β scales with the probability density of the carrier outside the nanocrystal, we can understand that

$$\beta_e = (15.33)\beta_h \quad [2.27]$$

for the specific case of a R = 2.5 nm CdSe QD surrounded by a 5 eV square well potential. Note that for a material with $m_e \approx m_h$ (i.e. PbSe), it can be assumed that $\beta_e \approx \beta_h$.[54] Expanding on the ideas of equations 2.20-2.25, we can understand the red-shift of the first exciton absorption peak as films become more strongly coupled. As tight-binding theory predicts a band-broadening proportional to the exchange coupling energy (eq 2.24), we expect to see a difference in the broadening of the valence band with respect to the conduction band in CdSe, illustrated in figure 2.19. Expanding equation 2.24 to account for varying coupling energies between electrons and holes yields the following relationship[52, 54]:

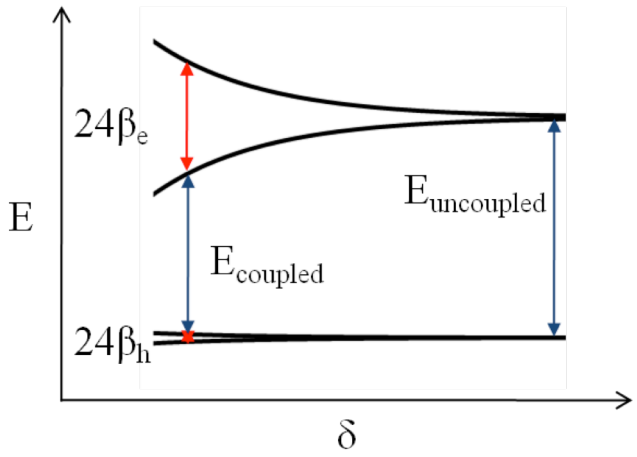

Figure 2.12: Illustration of band broadening due to coupling in CdSe nanocrystals. Due to the smaller effective mass of the electron in CdSe, the conduction bands are more strongly coupled than the valence bands as the interparticle distance (δ) is decreased. As $E_{coupled} < E_{uncoupled}$, a red shift is observed in the 1st exciton absorption peak.

$$E_{coupled} = E_{uncoupled} - (12|\beta_e| + 12|\beta_h|) \quad [2.28]$$

Substituting equation 2.27 results in our special case of the 5 nm CdSe QD in a 5 eV deep well:

$$E_{coupled} = E_{uncoupled} - 12.78|\beta_e| \quad [2.29]$$

allowing us to experimentally determine the exchange coupling energy of a nanocrystal film. When dealing with electron transfer in nanostructured systems, Marcus electron transfer theory is often used:

$$k_{ET} = \frac{2\pi}{\hbar}|H_{AB}|^2 \frac{1}{\sqrt{4\pi\lambda k_B T}} e^{\frac{-(\lambda+\Delta G)^2}{4\lambda k_B T}} \qquad [2.30]$$

Where H_{AB} is the electronic coupling of the initial and final states (equation 2.18), ΔG is the change in free energy (energy level offsets) and λ is the system's reorganizational energy. Quantum dots have extremely high surface area to volume ratios and when a QD becomes charged (either donating or accepting an electron) some nuclear rearrangements will occur to minimize the system's energy. The energy cost of these rearrangements is the reorganizational energy, thought to be roughly 100 meV in semiconductor quantum dots. While smaller λ values will increase the rate of electron transfer, the strength of this relationship ultimately will vary from QD to QD and largely be out of our control from an engineering perspective. The two important factors in equation 2.30 are the coupling energy H_{AB} and the change in free energy ΔG. Equation 2.30 however, only deals with electrons transferring from one specific state to another specific state. In a quantum dot optoelectronic device, the nanostructures will inevitable have to be coupled some bulk substrate which has a continuum of states. Figure 2.13 illustrates this idea, showing discrete energy levels in a CdSe QD coupled to continuous bands in an ITO substrate. We can modify equation 2.30 by including the density of available states (the conduction band of ITO) for the electron to transfer to:

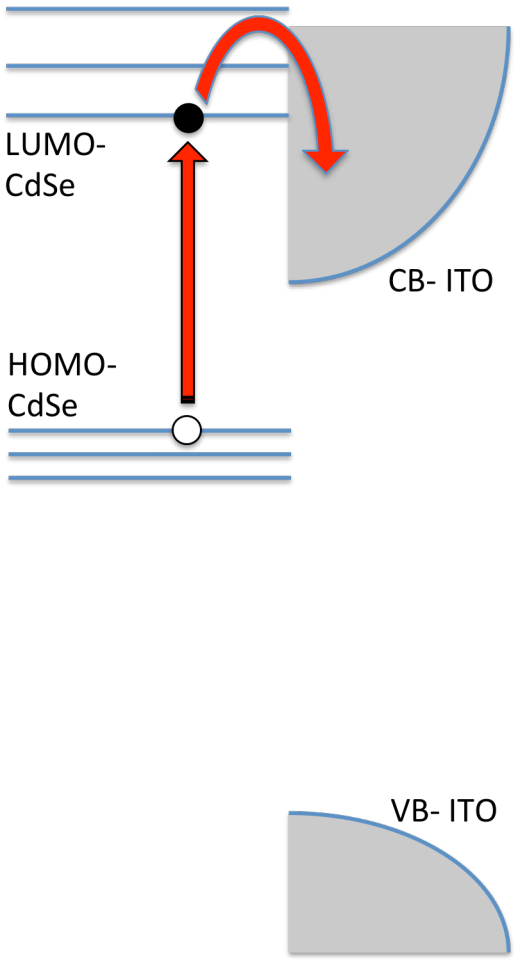

Figure 2.13: An illustration of the discrete levels of a 4.2 nm CdSe QD (left) with the continuous bands of ITO (right)

$$k_{ET} = \frac{2\pi}{\hbar} \int_{-\infty}^{\infty} \rho(E) |H_{AB}|^2 \frac{1}{\sqrt{4\pi\lambda k_B T}} e^{\frac{-(\lambda+\Delta G)^2}{4\lambda k_B T}} \qquad [2.31]$$

Where ρ(E) is the available density of states in the conduction band of ITO:

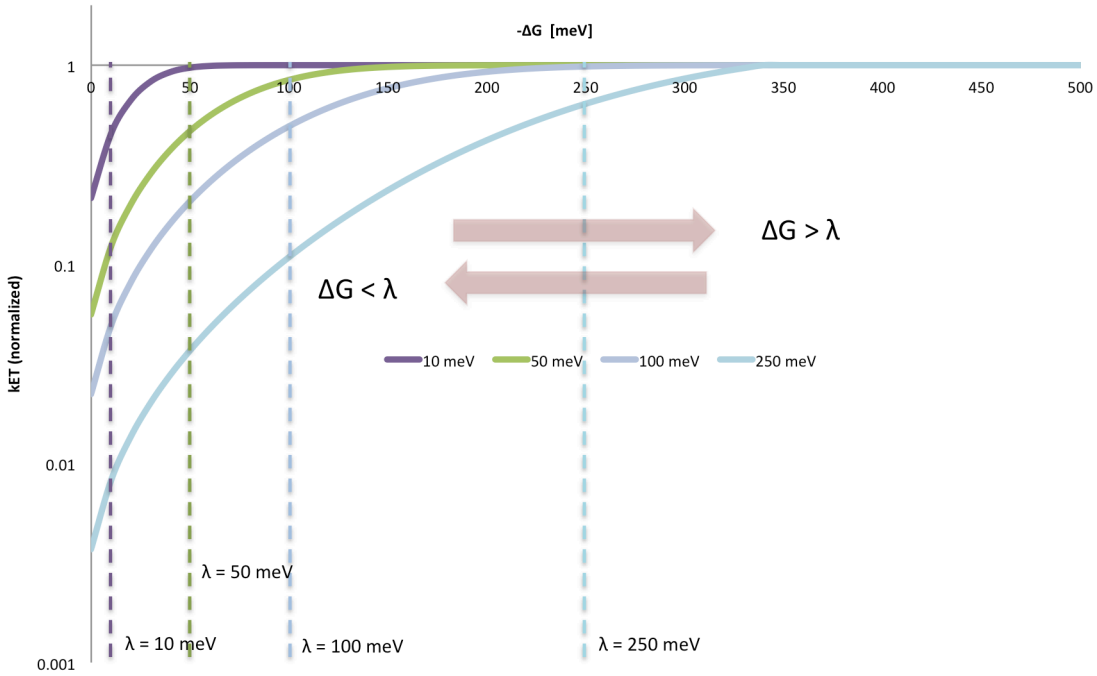

Figure 2.14: Four plots of k_{ET} as a function of –ΔG with varying values of λ (10 meV, 50 meV, 100 meV, 250 meV). When –ΔG < λ the dominant influence on k_{ET} is the reorganizational energy (λ). When –ΔG > λ the dominant influence on electron transfer rate is the available density of states, subsequent increases in ΔG have little effect on k_{ET} far beyond this point.

$$\rho(E) = \frac{8\pi\sqrt{2}}{h^3} m^{*3/2} \sqrt{(E - E_c)}\,. \qquad [2.32]$$

It is evident from equation 2.31 that maximizing the -ΔG is critical to having high rates of electron transfer. What is less obvious however is that the electron transfer rate has two general regimes, one in which it is dominated by the density of available states (-ΔG > λ) and another in which it is dominated by the reorganizational energy (-ΔG < λ). This

becomes clear when we graph equation 2.32 using different values for λ (10 meV, 50 meV, 100 meV, 250 meV) in figure 2.14. ΔG arises from three main energetic changes in an electron transfer event in a quantum dot. $\Delta G_{CHARGING}$ represents the change in energy between a neutral initial state and a charged (+/-1) final state, $\Delta G_{COULOMB}$ represents the energy required to spatially separate the electron and hole (the coloumb attraction, equation 6) and $\Delta G_{ELECTRONIC}$ represents the energy level offset between the initial (LUMO of QD) and final (CB of substrate) states. ΔG is the sum of these three terms and is critical to consider when choosing materials to interface with QD films. The CdSe-ITO system has been proposed for this work to an extent as a result of its large ΔG ($\Delta G_{ELECTRONIC}$ ~ 1 eV, ΔG ~ 0.5 eV).

2.4 Density of States Derivation

Assuming a square potential with depth V_0 and macroscopic length L (figure 1), we

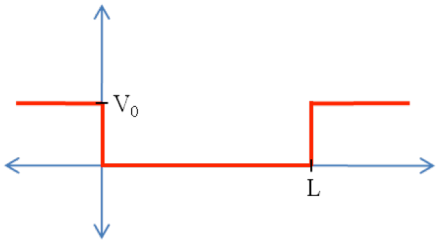

Figure 2.15: A potential well of depth V_0 and length L (L = 1 μm).

understand the solutions to the wave equation when V(x) = 0 to be:

$$\Psi(x) = A\sin(k_x x) + B\cos(k_x x). \qquad [2.33]$$

With the following boundary conditions:

$$\Psi(x) = 0; \;\; @ \;\; x = 0, L. \qquad [2.34]$$

Which yields the following solutions:

$$\Psi(x) = A\sin(k_{nx} x); \text{ such that } k_{nx} = \frac{n\pi}{L}. \qquad [2.35]$$

To calculate the density of states (DOS) we must count the number of states in the reciprocal lattice. The reciprocal lattice is formed by taking the Fourier transform of the physical lattice and can be thought of as a group of points that represent allowed values

of wavevectors. Within the reciprocal lattice, each state occupies a volume corresponding to a cube with side length k_n, where n=1. We can therefore express the volume of an individual state as:

$$V_{state} = \left(\frac{n\pi}{L}\right)^3 = \left(\frac{\pi}{L}\right)^3. \qquad [2.36]$$

And the volume of the allowed states as one-eighth of a sphere with radius k:

$$V_{allowed} = \frac{1}{8}\frac{4}{3}\pi k^3 = \frac{1}{6}\pi k^3. \qquad [2.37]$$

To find the *number* of allowed states, we can simply divide the allowed volume by the individual state volume and multiply by two to account for spin degeneracy (see figure 2.16):

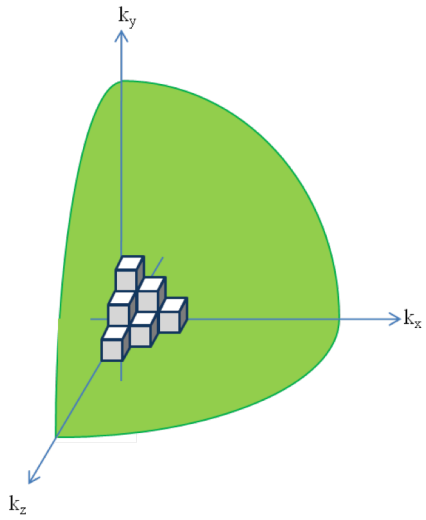

Figure 2.16: A graphical representation of individual states (shaded cubes at the origin) and the reciprocal space in which they are allowed (the green spherical volume) in three dimensions.

$$N = 2\frac{V_{allowed}}{V_{state}} = \frac{1}{3}\pi k^3 \left(\frac{L}{\pi}\right)^3. \qquad [2.38]$$

The DOS has units of [Energy^{-1}Volume^{-1}] and therefore is a density both volumetrically and energetically. Finding the volumetric density is straightforward as we simply divide the number of states by volume:

$$D = \frac{N}{V} = \frac{1}{3}\pi k^3 \left(\frac{L}{\pi}\right)^3 \frac{1}{L^3} = \frac{k^3}{3\pi^2}. \qquad [2.39]$$

Finding the energetic density is more complex, as we need to use the chain rule to find dD/dE:

$$g(E) = \frac{dD}{dk}\frac{dk}{dE} = \frac{k^2}{\pi^2}\frac{dk}{dE}. \qquad [2.40]$$

Which requires us to express k in terms of E:

$$k = \frac{\sqrt{2m^*(E-E_c)}}{\hbar}. \qquad [2.41]$$

Where E_c is the conduction band edge. Now we derive, re-writing E in terms of k:

$$\frac{dk}{dE} = \frac{\sqrt{2m^*}}{\hbar}\left(\frac{1}{2\sqrt{(E-E_c)}}\right) = \frac{m^*}{\hbar^2}\frac{\hbar}{\sqrt{2m^*(E-E_c)}} = \frac{m^*}{\hbar^2 k}. \qquad [2.42]$$

Substituting back into equation 8 yields the density of states. The effective mass accounts for the periodic lattice potential seen by the charge carriers, allowing this expression to describe a variety of systems:

$$g(E) = \frac{k^2}{\pi^2}\frac{m^*}{\hbar^2 k} = \frac{km^*}{\hbar^2\pi^2} = \frac{km^*}{\hbar^2\pi^2}. \qquad [2.43]$$

Expressing k in terms of E and replacing the reduced Planck's constant with Planck's constant yields the familiar form:

$$g(E) = \frac{km^*}{\hbar^2\pi^2}\frac{1}{k}\frac{\sqrt{2m^*(E-E_c)}}{\hbar} = \frac{\sqrt{2(E-E_c)}}{\hbar^3\pi^2}{m^*}^{3}\!/_{2} = \frac{\hbar^3}{h^3}(2\pi)^3\frac{\sqrt{2(E-E_c)}}{\hbar^3\pi^2}{m^*}^{3}\!/_{2} =$$

$$\frac{8\pi\sqrt{2}}{h^3}{m^*}^{3}\!/_{2}\sqrt{(E-E_c)}. \qquad [2.44]$$

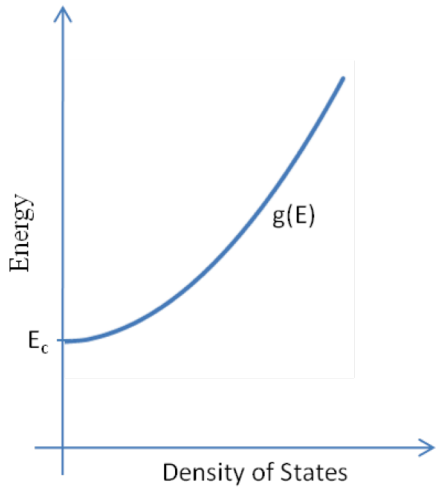

Figure 2.17: A plot of equation 2.44.

For an electron in the conduction band of a semiconductor we know that the DOS below E_c is zero:

$$g(E) = \frac{8\pi\sqrt{2}}{h^3}{m^*}^{3}\!/_{2}\sqrt{E-E_c}\ ; \qquad E \geq E_c$$

$$g(E) = 0\ ; \qquad E < E_c.$$

[2.45]

Plotting equation 2.44 gives us the familiar picture of the parabolic bulk density of states above the conduction band edge in a semiconductor.

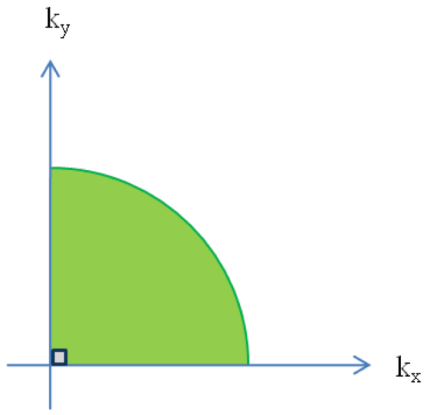

Figure 2.18: A graphical representation of individual states (shaded circle at the origin) and the reciprocal space in which they are allowed (the green circular area) in two dimensions.

In a system with dimensions smaller than the electron's mean free path, electronic motion is confined to those larger dimensions. In the case of a (1 nm, 1 µm, 1 µm) box, the electron is confined to two dimensions. Returning to equation 4 and noting that instead of a 3-d reciprocal volume we now have a 2-d area (figure 4), we derive the 2-d density of states. Instead of a state's volume, they now have an area:

$$A_{state} = \left(\frac{n\pi}{L}\right)^2 = \left(\frac{\pi}{L}\right)^2. \qquad [2.46]$$

We write the area of the reciprocal space as one-fourth of a circle with radius k:

$$A_{allowed} = \frac{1}{4}\pi k^2. \qquad [2.47]$$

To find the number of allowed states:

$$N = 2\frac{A_{allowed}}{A_{state}} = \frac{1}{2}\pi k^2 \left(\frac{L}{\pi}\right)^2. \qquad [2.48]$$

Finding the spatial density:

$$D = \frac{N}{A} = \frac{1}{2}\pi k^2 \left(\frac{L}{\pi}\right)^2 \frac{1}{L^2} = \frac{k^2}{2\pi}. \qquad [2.49]$$

Finding the energetic density:

$$g(E)_{2D} = \frac{dD}{dk}\frac{dk}{dE} = \frac{k}{\pi^2}\frac{dk}{dE}. \qquad [2.50]$$

Substituting equation 10 into 18, we find a remarkable result, a 2-d DOS independent of energy:

$$g(E)_{2D} = \frac{k}{\pi^2}\frac{m^*}{\hbar^2 k} = \frac{m^*}{\pi^2\hbar^2} = \frac{4m^*}{h^2}. \qquad [2.51]$$

Mathematically this is described by a Heaviside function, yielding a staircase like band structure for a two dimensional structure like a quantum well. In figure 5, the three dimensional DOS function (blue curve) is included with the two dimensional DOS function (red staircase) for illustrative purposes. Taking the analysis one step further, we see in figure 5 that every "step" in energy is quadratic: the second step is four times the

energy of the first, the third is nine times the first, so on and so forth. This arises as the energy levels are scaled according to the quantized wave vector (in this case k_x):

$$\frac{E}{E_0} = {k_x}^2, \; k_x = 1,2,3 \ldots \qquad [2.52]$$

While this is relatively straightforward for a two-dimensional semiconductor (no degenerate states), the above relationship has important consequences for energy level spacing and higher degeneracy in lower dimensional structures.

Now we consider the case of a (1 nm, 1 nm, 1 μm) box, where the electron is confined to one dimension. We now have a 1-d length in reciprocal space and can derive the 1-d density of states:

$$L_{state} = \frac{n\pi}{L} = \frac{\pi}{L}. \qquad [2.53]$$

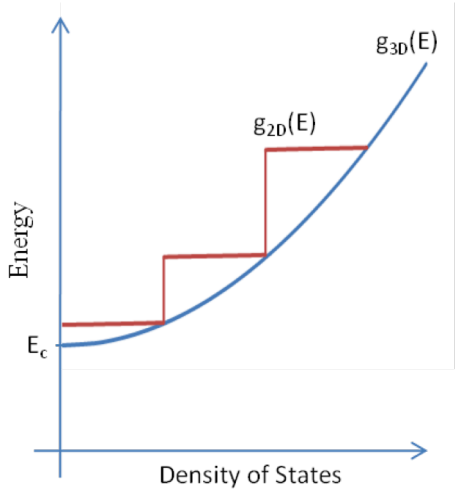

Figure 2.19: A plot of E vs. DOS for 2-d and 3-d structures

We write the length of the reciprocal space as a line of length k:

$$L_{allowed} = k. \qquad [2.54]$$

Figure 2.20: A graphical representation of individual states (black line at the origin) and the reciprocal space in which they are allowed (the green line) in one dimension.

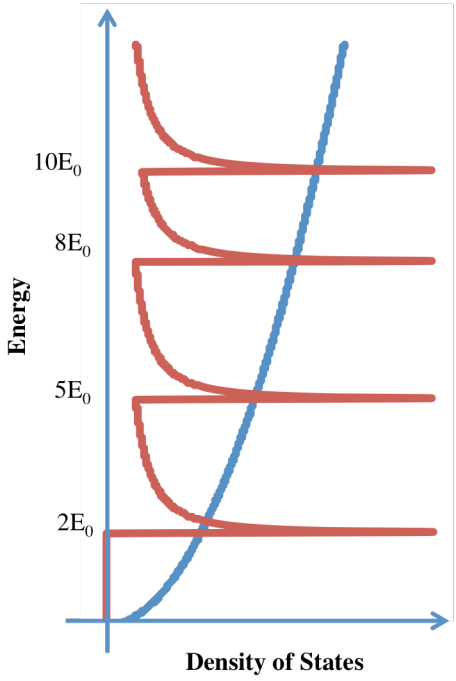

Figure 2.21: A plot of E vs. DOS for 1-d and 3-d structures. Note the energy level spacings shown on the vertical axis.

To find the number of allowed states:

$$N = 2\frac{L_{allowed}}{L_{state}} = k\frac{L}{\pi}. \qquad [2.55]$$

Finding the spatial density:

$$D = \frac{N}{L} = k\frac{L}{\pi}\frac{1}{L}. \qquad [2.56]$$

Finding the energetic density:

$$g(E)_{1D} = \frac{dD}{dk}\frac{dk}{dE} = \frac{1}{\pi}\frac{dk}{dE}. \qquad [2.57]$$

Substituting equation 10 into 24, we find the 1-d DOS:

$$g(E)_{1D} = \frac{1}{\pi}\frac{m^*}{\hbar^2 k} = \frac{m^*}{\pi\hbar^2 k} = \frac{1}{\hbar\pi}\sqrt{\frac{m^*}{2E}} = \frac{1}{h}\sqrt{\frac{2m^*}{E}} \qquad [2.58]$$

This band structure is inversely dependent on energy, with the maximum densities of states occurring at the band edge (not unlike the 2-d system). As this system is confined in two dimensions (k_x and k_y), the energy level scaling is more complex than before:

$$\frac{E}{E_0} = {k_x}^2 + {k_y}^2,\ k_x, k_y = 1,2,3 \ldots \qquad [2.59]$$

Energy level spacing is thus 2 (1^2+1^2), 5 (1^2+2^2), 8 (2^2+2^2) and 10 (1^2+3^2) for the first four levels. Note also that the second and fourth energy levels have a two-fold degeneracy of while the first and third do not.

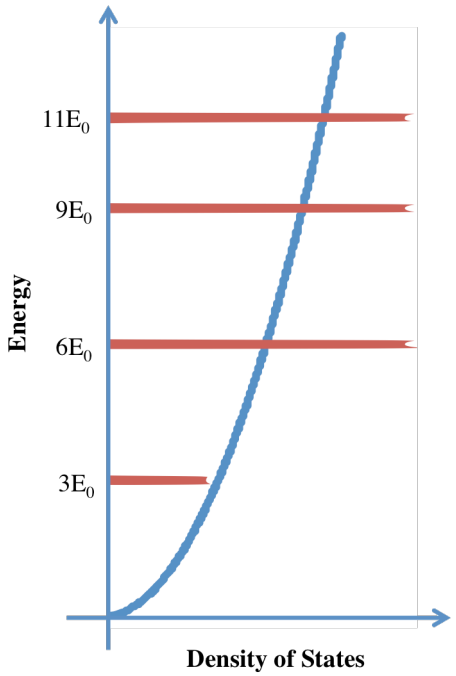

Figure 2.22: A plot of E vs. DOS for 0-d and 3-d structures. Note the energy level spacings shown on the vertical axis.

Now we consider the case of a (1 nm, 1 nm, 1 nm) box, where the electron is confined to zero dimensions (no free motion possible). As no motion is allowed, no reciprocal space exists to be filled with electrons. Therefore, all available states only exist at specific, discrete energy levels, conveniently described by a delta function (figure 2.22).

$$g(E)_{0D} = 2\delta(E_A). \qquad [2.60]$$

Where E_A is an allowed energy. In this case the electron is confined in three dimensions and the energy scaling is:

$$\frac{E}{E_0} = {k_x}^2 + {k_y}^2,\ k_x, k_y = 1,2,3 \ldots \qquad [2.59]$$

The first four energy level spacings are thus 3 ($1^2+1^2+1^2$), 6 ($1^2+1^2+2^2$), 9 ($1^2+2^2+2^2$) and 11 ($1^2+1^2+3^2$). Note the first level has no degeneracy (analogous to an "s" atomic orbital) while the subsequent orbitals have 3-fold degeneracy (analogous to "p" atomic orbitals).

A dimensional analysis of equations 2.43, 2.50, 2.57 and 2.60 (DOSs for 3-d, 2-d, 1-d, and 0-d, respectively) show the following units:

$$g(E)_{3D} = \left[\frac{s^2}{kg\ m^5}\right] = \text{Energy}^{-1}\text{Volume}^{-1}$$

$$g(E)_{2D} = \left[\frac{s^2}{kg\ m^4}\right] = \text{Energy}^{-1}\text{Area}^{-1}$$

$$g(E)_{1D} = \left[\frac{s^2}{kg\ m^3}\right] = \text{Energy}^{-1}\text{Length}^{-1}$$

$$g(E)_{0D} = \left[\frac{s^2}{kg\ m^2}\right] = \text{Energy}^{-1}$$

[2.61-2.64]

To obtain a meaningful density of states ($eV^{-1}cm^{-3}$) we therefore need to multiply the 2-d, 1-d and 0-d equations by length^{-1}, area^{-1} and volume^{-1}, respectively. Physically, this is simply the quantum well depth, the nanowire cross-sectional area and the quantum dot volume, respectively. Plugging these values in gives us expressions for calculable DOSs over all 4 cases:

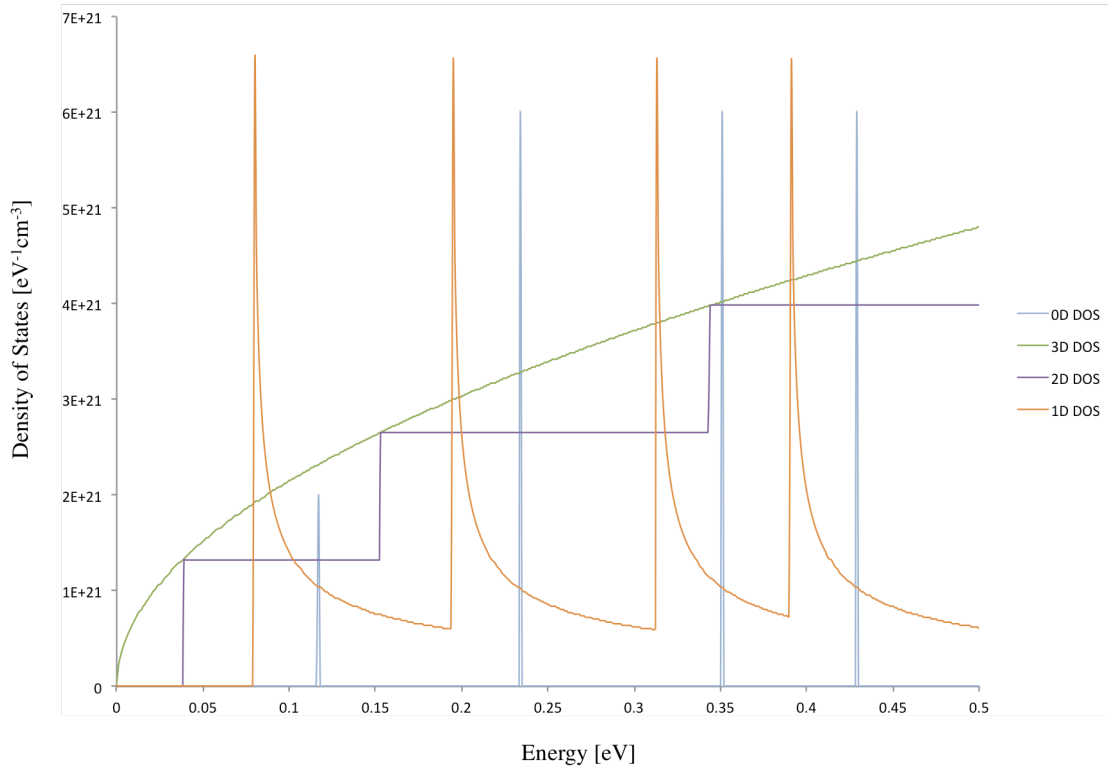

Figure 2.23: A plot of E vs. DOS for 0-d, 1-d, 2-d and 3-d structures ((a,a,a);(a,a,L);(a,L,L);(L,L,L), L = 1 μm, a = 1 nm). Effective mass (m*) is assumed to be rest mass (m_0).

$$g(E)_{3D} = \frac{8\pi\sqrt{2}}{h^3} m^{*3/2}\sqrt{(E - E_c)}$$

$$g(E)_{2D} = \frac{4m^*}{h^2}\frac{1}{a_x}$$

$$g(E)_{1D} = \frac{1}{h}\sqrt{\frac{2m^*}{E}}\frac{1}{a_x a_y}$$

$$g(E)_{0D} = 2\delta(E_A)\frac{1}{a_x a_y a_z}$$

[2.65-2.68]

In our system, $a_x = a_y = a_z = 1$ nm $= 10^{-7}$ cm. Plugging in these values and assuming $m^*=m_0$ we see the relationship shown in figure 2.23.

2.5 Characterization

The strongly size dependent optical properties of CdSe quantum dots has been extensively studied over the past two decades[20, 55-57], allowing for rapid characterization of samples of devices by relatively straightforward spectroscopic methods. While photoluminescence studies have been performed, this process is highly dependent on surface chemistry (passivating epitaxial shell, capping ligand) sometimes yielding results that are difficult to interpret as many recombination pathways exist for excited charge carriers. Absorption measurements are preferred as these experiments more directly probe the photon-QD interaction and are largely insensitive to ligand character or the presence of a passivating shell.[20, 55] Absorption spectra are taken of solutions of CdSe dots in a solvent and can be used to determine both dot size and sample concentration, the latter being a critical parameter for quantitative processes such as Langmuir Films.

2.5.1 Size Determination

The assignment of the first exciton (1Se-1Sh) transition is straightforward in CdSe absorption spectra as it is the lowest energy peak observed. Furthermore, the position of this peak can be used to quickly determine the size of quantum dots present in the sample. As discussed earlier, Brus et al. developed an early theoretical model for this relationship[2] and Yu et al. followed up with an empirical relationship[20] using a fourth order polynomial to determine the size as a function of wavelength. Recently, Jasieniak et al. revisited these relations and found Yu's equations to be in good agreement with both their theoretical and experimental findings[55] (figure 2.23).

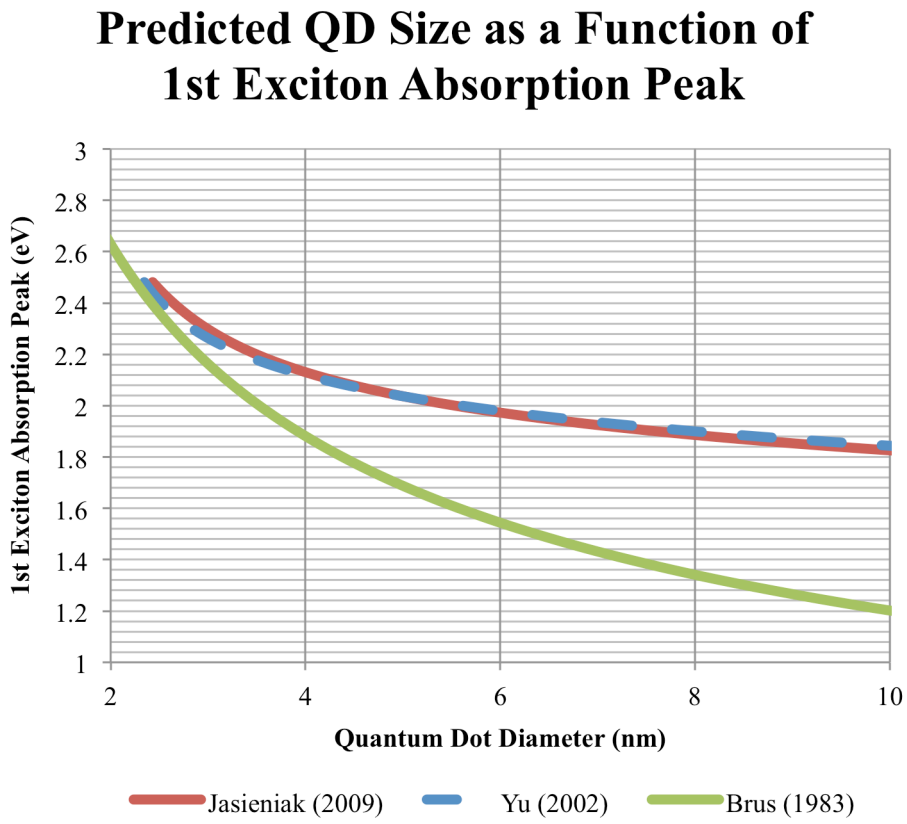

Figure 2.24: Comparison of predicted QD diameters using the 1st exciton peak from the absorption spectra. Note the excellent agreement between the Yu amd Jasieniak relationships, both determined empirically and independently.

While this size determination is consistent and well understood, understanding the concentration of the sample is more difficult, with significant variation in the published literature as to agreed upon methods and values.

2.5.2 Molar Absorptivity of CdSe Quantum Dots

The molar absorptivity (synonymous with molar absorption coefficient and molar extinction coefficient) is the measure of how strongly a species absorbs light. This value is intrinsic to chemical species and obviously is a function of energy, giving rise to characteristic absorption peaks and valley unique to individual compounds. The impact of quantum confinement however, is not well understood with respect to the extinction coefficient of CdSe nanomaterials. Understanding this effect and determining accurate values for ε at the 1st exciton absorption peak is critical to determining the concentration and ultimately forming monolayer films of these materials.

By using Beer's law we see a simple relationship for interpreting spectroscopy data:

$$A = \varepsilon CL \qquad [2.69]$$

Where A is the absorbance of the sample, C is the concentration (in units of molarity), L is the path length (in units of cm) and ε is the molar absorptivity (in units of $M^{-1}cm^{-1}$). While the extinction coefficient is a function of energy, it is typically characterized and used in computations at a certain value, typically at the first exciton absorption peak. A notable exception to this convention is the work done by Leatherdale et al., where the molar absorptivity relation is calculated at 350 nm for all sizes of CdSe particles.[56]

Leatherdale et al. were some of the earliest reports for values of ε as a function of nanocrystal size[56]. The work actually reported the absorption cross section (σ, in units of

cm^2) of the nanocrystals, which can be easily converted to molar absorptivity by the following relation:

$$\varepsilon = \frac{\sigma N_A}{1000\, ln(10)} = (2.615 * 10^{20})\, \sigma \qquad [2.70]$$

While the units may appear confusing initially, recalling the relationship between liters and cubic centimeters (1 L = 1000 cm^3) elucidates the relationship:

$$\varepsilon \left[\frac{1}{M\ cm}\right] = \sigma\ [cm^2]\ N_A \left[\frac{1}{mol}\right] \left[\frac{L}{1000\ cm^3}\right] \frac{1}{ln(10)} \qquad [2.71]$$

And further allows us to take the Leatherdale expression:

$$\sigma_{350\ nm,\ Leatherdale} = (5.501 * 10^5)\ a_{cm}{}^3 \qquad [2.72]$$

Where a is the quantum dot radius in cm, and express it as a molar absorptivity:

$$\varepsilon_{350\ nm,\ Leatherdale} = (1.439 * 10^{25})\ a_{cm}{}^3 \qquad [2.73]$$

For convenience and sense of scale, let us use nm as the unit for QD radius:

$$\varepsilon_{350\ nm,\ Leatherdale} = (1.439 * 10^4)\ a_{nm}{}^3 \qquad [2.74]$$

As noted earlier, it is important to recognize this relationship determines a value for molar absorptivity at 350 nm, while subsequent studies define ε at the first exciton absorption peak.

Approximately two years after the Leatherdale report, Yu et al. published a study which became a well accepted reference for CdSe size calculations based on the absorption spectra. As such, we initially used their empirically determined formula(s) to also determine the molar absorptivity and thus the concentration of our samples. Yu noted that these values were size dependent, proposing two relations for molar absorptivity, one dependent on the particle's size and first exciton absorption peak (equation 2.75); the other only on the particle's size (equation 2.76):

$$\varepsilon_{1s,Yu.1} = 1600\ \Delta E\ (D^3) \qquad [2.75]$$

$$\varepsilon_{1s,Yu.2} = 5857\ (D^{2.65}) \qquad [2.76]$$

The reason for these two relations was a desire to fit the absorption to a 3rd power dependence on size (similar to Leatherdale), a relation previously postulated in a theoretical effort.[58] It should be noted that both relationships are extremely close to each other (within 10% deviation for particles < 10 nm in diameter) and the second relation (equation 2.71) is merely provided for convenience.

Initial studies done with Yu's calculations proved troublesome as we measured far lower concentrations on a Langmuir film surface. Further investigation determined that the problem may lie within the Yu expression itself. The Yu relationship yielded significantly different molar absorptivities than those arrived at via Leatherdale's method,

causing concern as to the viability of a such a concentration dependent procedure without proper characterization methods. Our own analysis via Langmuir film methods suggested we had lower concentrations than Yu (closer to Leatherdale's relation) but at the time unrealized problems with our films (discussed further in Chapter 4) resulted in difficulties in verifying either method.

Jasieniak and others undertook a rigorous review of the current understanding of size dependent absorption coefficients in CdSe quantum dots in late 2009, combining transmission electron microscopy (TEM) with inductively coupled plasma atomic emission spectroscopy (ICP-AES) as well as traditional spectroscopic methods to determine the true absorptive properties of these particles.[55] As mentioned, the prediction for particle size based on absorption was largely consistent with earlier findings (figure 2.23), arriving at an empirically determined 4th order polynomial relationship for the size based on the first exciton absorption peak (in units of nm):

$$D = 59.60816 - 0.54736\,\lambda + (1.8873 * 10^{-3})\,\lambda^2 + (2.85743 * 10^{-6})\,\lambda^3 + (1.62974 * 10^{-9})\,\lambda^4 \qquad [2.77]$$

However the determination of the extinction coefficient produced markedly different results (figure 2.24). Jasieniak et al. suggested a size dependant exponential relation between the 1st exciton absorption energy and exctinction coefficient, deviating from the cubic (or near cubic in eq 2.76) relations posed earlier by Leatherdale and Yu:

$$\varepsilon_{1s,Jasieniak} = 155507 + (6.67054 * 10^{13})\,e^{\left(-\frac{E_{1S}}{0.10551}\right)} \qquad [2.78]$$

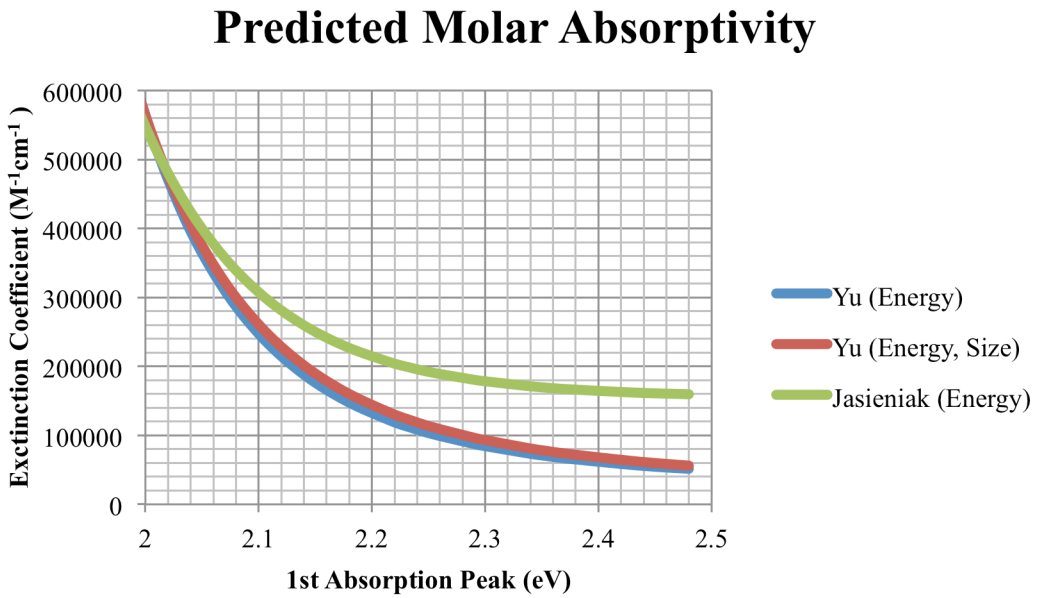

Figure 2.25: Predicted molar absorptivity found empirically by Yu (2002) and later by Jasieniak (2009) this deviation observed for particles with E1s > 2.1 is significant when characterizing spreading solutions for use in Langmuir films.

While not directly comparable to the Leatherdale relation (as the latter determines the extinction coefficient at 350 nm, while the former determines it at the band edge), Analysis of our own absorption data (figure 2.26) showed good agreement between Leatherdale and Jasieniak, both of which were closer to what we were measuring in the Langmuir trough. Furthermore, flaws in the Yu methodology were revealed (such as the implication of >100% reaction yields), so we proceeded using the Jasieniak model for determining concentrations.

2.5.3 Non linear least squares fitting method

Figure 2.26 illustrates a sample absorption spectra for CdSe-TOPO quantum dots dispersed in toluene. A nonlinear least squares method (Gauss-Newton) was used to fit the data to multiple Gaussian peaks for the E < 2.90 eV region using MATLAB® software.[59] We chose to model the absorption data with three Gaussian peaks and found excellent agreement with our data (R^2 = 0.9999, figure 2.27) Fitting further Gaussian peaks (up to eight) introduced some finer structure into the existing peaks but did not appreciably improve the quality of the fit. This was expected, as three main peaks ($1S_{3/2}$-$1S_e$, $2S_{3/2}$-$1S_e$, $1P_{3/2}$-$1P_e$,) were shown to dominate the absorption spectra of such nanocrystals in Norris and Bawendi's initial study of these materials.[57] The fitting method used does not have a closed solution (as it's linear counterpart does) so initial conditions are chosen and the final fits are obtained iteratively. It should be noted that the Jasieniak, Yu and Leatherdale methods are all empirical: When the authors reference a particular peak they are referencing the physical data, not the individual Gaussian component of the fit. In many instances these values are substantially different, such as larger nanocrystals with greater overlap between the 1S-1S and 1S-2S peaks, and can introduce error if not followed properly.

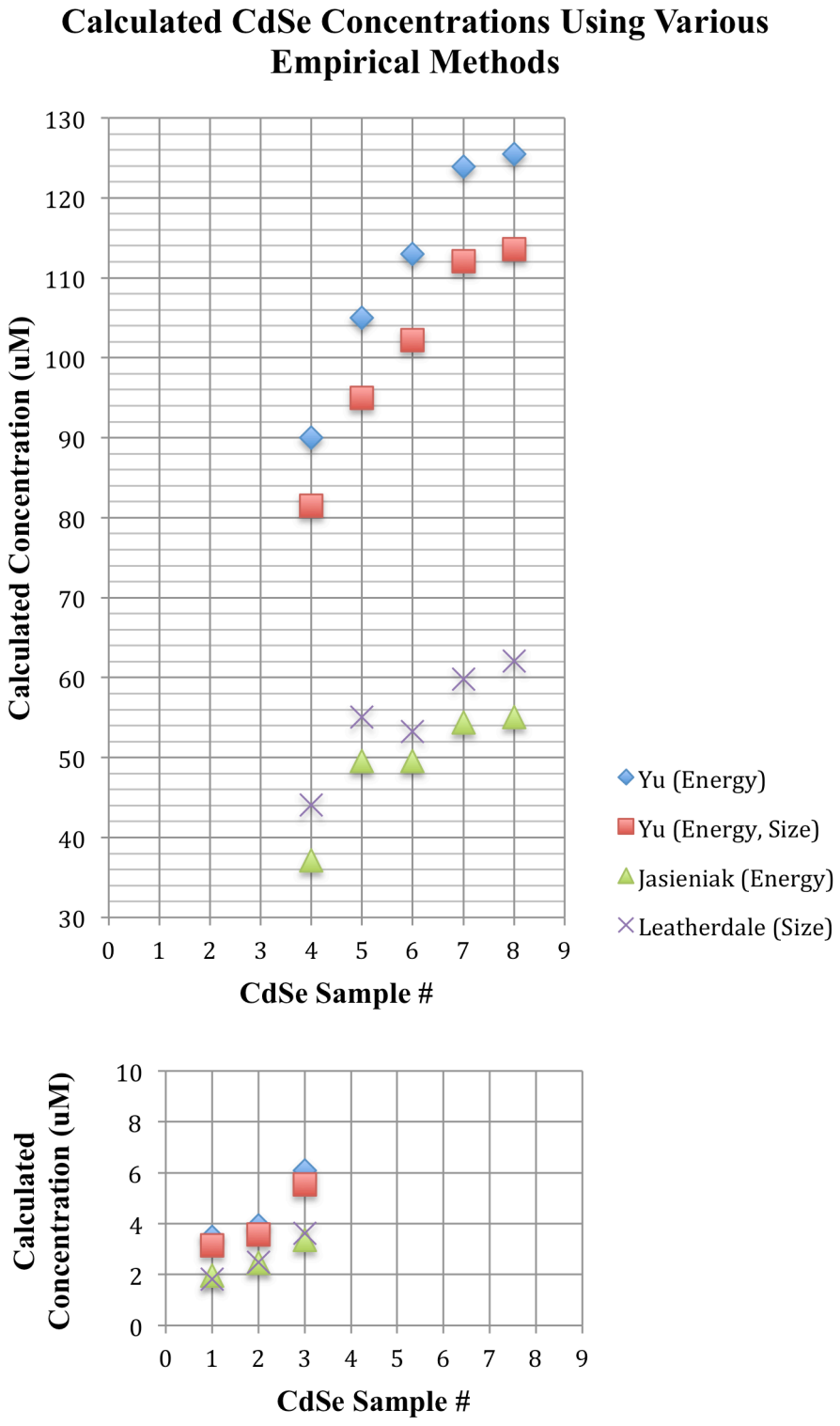

Figure 2.26: Analysis of nine samples of CdSe-TOPO QD spreading solutions and their calculated concentrations using various empirical methods.

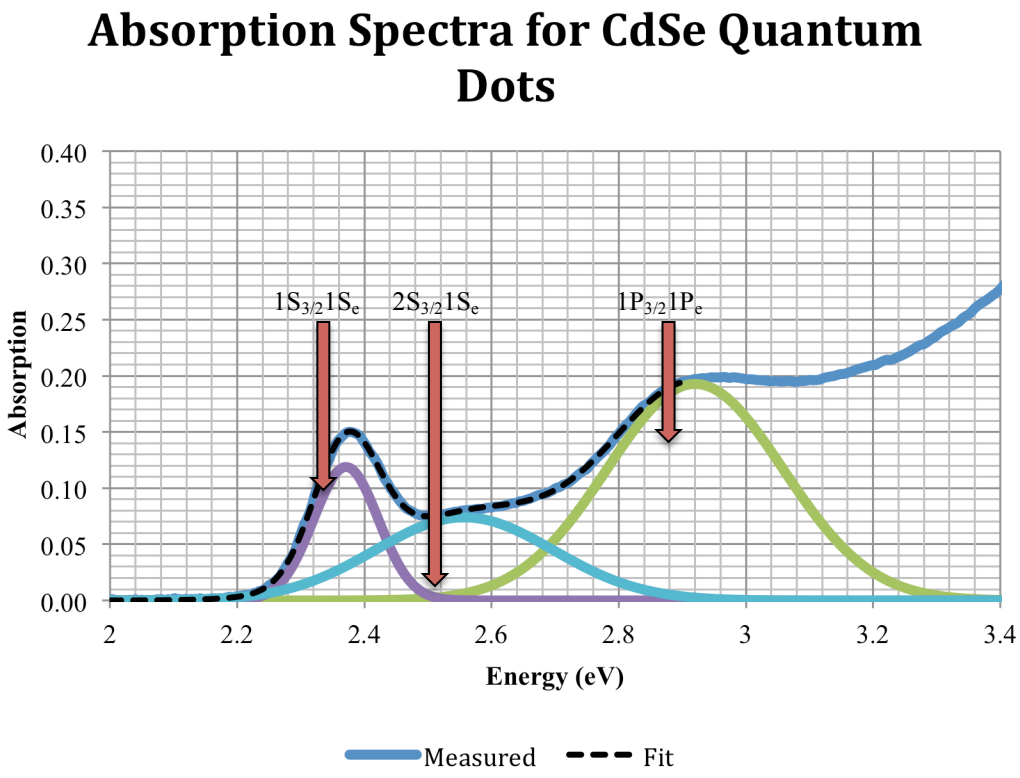

Figure 2.27: Sample absorption spectra with non-linear least squares Gaussian fitting for the three dominant transistions. $R^2 = 0.9999$.

CHAPTER 3: LANGMUIR FILMS OF AMPHIPHILIC MOLECULES

The Langmuir film process involves spreading a thin film of nanoparticles in an organic solvent on a subphase (usually water) surface and allowing the solvent to evaporate. As the solvent evaporates, a monolayer array of nanoparticles nucleates at the raised center of the subphase surface and propagates smoothly outward. Barriers are compressed to reduce the surface area of the array, packing the nanoparticles more closely together. The goal is that the resulting monolayer is a well ordered, densely packed, two dimensional hexagonal close packed array.[60]

3.1 Introduction and Background

Observations of the behavior of oil on water date back to Pliny the Elder in 79 AD, while the first scientific studies of such films came from Benjamin Franklin in 1773:

> "I went to the windward side, where [waves] began to form; and there the oil, though not more than a teaspoon full, produced an instant calm over a space several yards square, which spread amazingly, and extended itself gradually till it reached the lee side, making all that quarter of the pond, perhaps half an acre, as smooth as a looking glass. … In these experiments, one circumstance struck me with particular surprise. This was the sudden, wide, and forcible spreading of a drop of oil on the face of the water, which I do not know that any body has hitherto considered."
>
> Benjamin Franklin, letter to William Brownrigg, London, November 7, 1773.[61]

While his efforts were aimed at reducing drag on shipping vessels, his observation that one teaspoon (5 ml) spread out to approximately half an acre (2000 m^2) suggested a film only 2 nm thick, the first report of an organic monolayer on an aqueous subphase (this was not realized at the time by Franklin). Not until a century later was this observation expanded on, when Lord Rayleigh and Agnes Pockels performed a series of quantitative studies on such phenomenon.[62] Pockels noted that very small amounts of oil on a water surface had little to no effect on surface tension, but that the surface tension began to decrease suddenly when the amount of oil per unit area was increased beyond a certain limit. Rayleigh theorized that the point where surface tension falls likely corresponded to a "one molecule deep" film. While most of this work was done in Pockels' kitchen sink, her correspondences with Rayleigh led to the work being published in Nature in 1891, laying the groundwork for the extensive studies done by Langmuir in the coming years.

Among other observations, Irving Langmuir determined the cross sectional areas of many surfactants, noting that these areas were "substantially independent" of the length of the hydrocarbon to which the "active" head groups were attached.[63] Furthermore, Langmuir determined the vertical lengths of these molecules, confirming his beliefs as to the orientation and morphology of such films: polar head groups submerged in the subphase with hydrophobic tails protruding vertically into the air (figure 3.1).

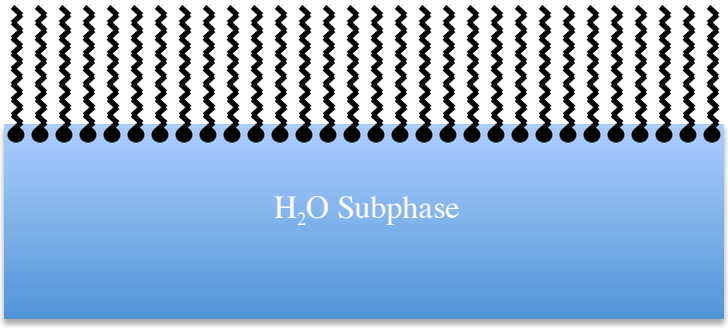

Figure 3.1: Diagram of Langmuir's proposed model of surfactant self-assembly at a water-air interface. Polar head groups (circles) are submerged in the water while hydrophobic tails protrude vertically into the air.

Katherine Blodgett, working with Langmuir, later demonstrated that a solid substrate introduced to a compressed monolayer would be coated homogenously, allowing for large area depositions of monolayer molecular films.[64] Blodgett explored this "Langmuir-Blodgett" technique extensively, producing multilayers of organic molecules and even developing early anti reflective coatings on glass. Beyond the understanding of the film's morphology, cross sectional area, Langmuir was able to understand the relationship between the surface tension and molecular area. Before discussing this in detail, it is important to understand how the surface tension is measured using the Wilhelmy plate technique.

3.2 The Wilhelmy Plate

There are several ways to characterize this nanoparticle film, which vary greatly from one trough to another. The first and most common metric is surface pressure, measured with a Wilhelmy plate. This is a well-known method with a high sensitivity (±0.01 mN/m) that uses a hydrophilic platinum plate partially immersed in the subphase. This is connected to a sensitive electrobalance, which measures the downward force

exerted by the liquid meniscus on the plate (see figure 3.2). Surface tension can be calculated using the following equation:

$$F = (mg) + 2(t + w)\gamma_L \cos\theta - hwt\rho_L \qquad [3.1]$$

Where γ_L and ρ_L are the surface tension and density (respectively) of the liquid subphase. Equation 3.1 can be understood as the sum of three factors: The first term represents the gravitational force on the plate itself, the second term represents the additional downward force due to the water wicking up the plate, while the third term accounts for the (upward) buoyant force on the Wilhemly plate. As the first and third terms are constants, we can simplify the relationship by expressing things in terms of ΔF:

$$\Delta F = 2(t + w)\Delta\gamma \cos\theta \qquad [3.2]$$

As θ is assumed to be zero (perfect wetting), the surface tension of the subphase is merely a linear function of the force measured by the balance. In Langmuir's method, the reported variable is the surface pressure (i.e. the force exhibited directly on a movable barrier), which can be defined in terms of surface tension (the variable measured):

$$\prod = \gamma_o - \gamma_L = -\Delta\gamma = \frac{-\Delta F}{2(t+w)\cos\theta} \qquad [3.3]$$

Note that the surface pressure is actually a function of the *negative* change in surface tension.

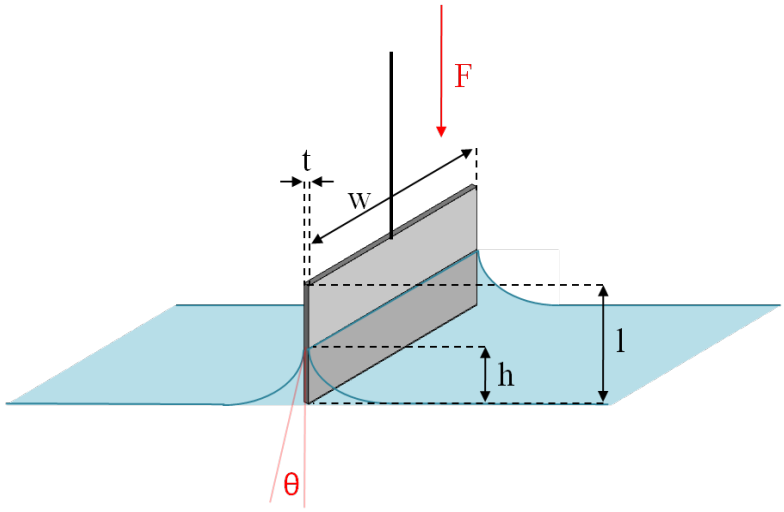

Figure 3.2: Diagram of a Wilhelmy Plate immersed in a water subphase. F is the downward force measured by the balance while θ is the contact angle of the subphase on the plate (assumed to θ=0 for water at Pt). w, h, l, and t are plate dimensions: width, immersion depth, length and thickness, respectively.

To derive the net vertical force on a cylinder immersed in a liquid we will first describe the system (figures 3.3, 3.4). The three important spatial variables are the radius of the cylinder (r), the height of the cylinder (h) and the submerged depth of the cylinder (d) (figure 3.3). The cylinder has a density ρ_C and the liquid has a density ρ_L and surface tension σ. The liquid makes contact with the cylinder at an angle θ, which is a function of the Young equation:

$$\gamma_{SG} - \gamma_{LG} - \gamma_{LV}\cos\theta = 0 \qquad [3.6]$$

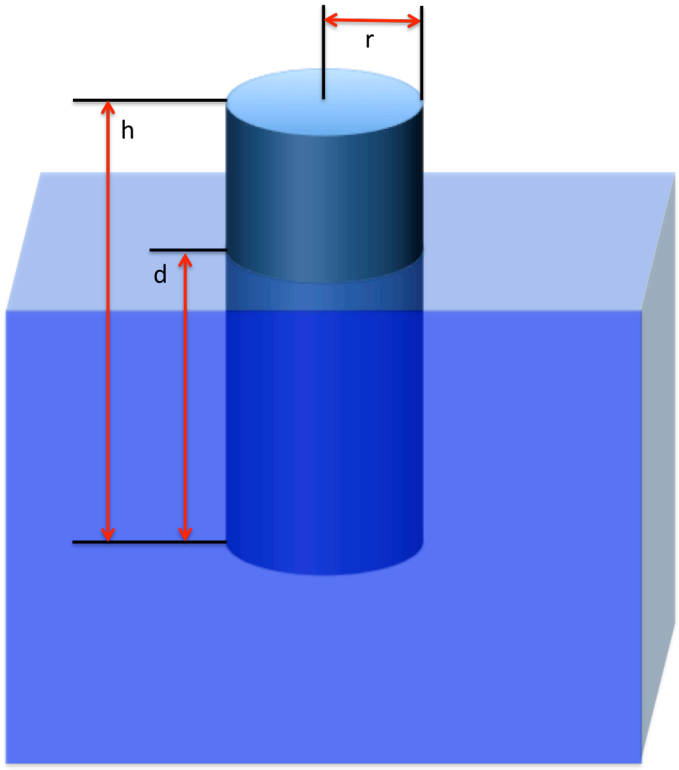

Figure 3.3: Diagram of a cylinder of radius r, height h and submerged depth d immersed in a liquid.

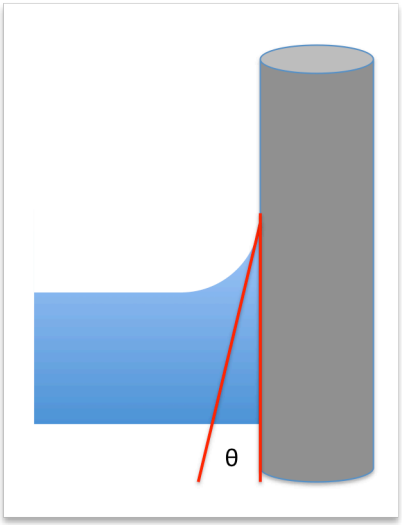

Figure 3.4: Diagram of the liquid contact angle θ with an immersed cylinder.

Where γ_{SG}, γ_{LG}, and γ_{LV} are the interfacial energies between the solid-gas, liquid-gas and liquid-vapor phases, respectively. There are three main components to the vertical force on the cylinder: (1) The gravitational pull on its mass (negative), (2) the buoyant force of the liquid (positive) and (3) the gravitational effects of the liquid wicking up the side of the cylinder (figure 2). The gravitational effect on the cylinder is straightforward:

$$F_g = -mg = -\pi r^2 h \rho_C g. \qquad [3.7]$$

As is the buoyant force, equal to the gravitational effects of displacing a volume of liquid equal to the submerged part of the cylinder:

$$F_B = m_L g = \pi r^2 d \rho_L g \qquad [3.8]$$

To determine the contribution of the liquid wetting the cylinder we must recognize that this is a surface energy phenomenon. The lower the energy of the cylinder, the higher the contact angle will be and conversely high energy surfaces will see very small contact angles. As surface energy has units of [Force.Length^{-1}] we need to multiply it by a length to yield a usable force term. This length we need to multiply by is simply the perimeter of whatever object is immersed in the liquid, in our case the circumference of the cylinder. To understand how the contact angle θ factors in, we need to look at boundary conditions. When the liquid forms a contact angle less than 90°, there is a net downforce on the cylinder; and when the liquid forms a contact angle more that 90°, there is a net upforce on the cylinder (when θ = 90° there is no force). This behavior is well described by the cosine function, yielding the familiar Wilhelmy equation:

$$F_W = -\sigma\, l \cos\theta. \qquad [3.9]$$

Where σ is the surface tension of the liquid and l is the cross sectional length on which the liquid is contacting the solid. Putting these equations (3.7, 3.8, 3.9) together gives us the total vertical force on a cylinder immersed in a liquid:

$$F_{net} = F_g + F_B + F_W = \pi r^2 d\rho_L g - \pi r^2 h\rho_C g - \sigma\, \pi r^2 \cos\theta\,. \qquad [3.10]$$

In an experimental setup, high energy surfaces are used for measurements as θ can be assumed to be zero (complete wetting). Furthermore, the liquid is typically water (ρ_L = 1) and the mass of the object is known, simplifying equation 10 considerably:

$$F_{net} = \pi r^2 dg - mg - \sigma \pi r^2 \qquad [3.11]$$

It should be noted that F_{net} will be negative so long as the cylinder has a density greater than that of the liquid. In the event that this was not the case the cylinder would be buoyant and the net vertical force zero.

3.3 Langmuir Isotherm Theory

Matter is well described by distinct phases in which physical properties are essentially uniform. Solids, liquids and gases are commonly cited as the three common phases of matter, but many others exist (liquid crystals, plamsas) that have unique definitions based on orientational and translation order.[65] Furthermore, further subdivisions exist (amorphous vs. crystalline solids) that are useful in describing morphology and behavior. A brief discussion of these phases is useful before proceeding to the two dimensional Langmuir analogy.

The gaseous state is characterized by weak intermolecular forces insufficient to hold molecules together, resulting in a uniform spreading of the molecules to occupy a container, regardless of its size. As the molecules are far apart and act weakly on each other, it takes relatively little force to compress a gas. The liquid phase, similar to the gas phase, has sufficient molecular energy for free movement and diffusion, but occupies a fixed volume and is highly incompressible. Liquids exhibit isotropic behavior

and have no long-range order. Solids are characterized by intermolecular interactions strong enough that molecules can only vibrate, resulting in a stable, fixed shape that can only be changed by force. It is important to note that while some phase changes have sharp transitions (i.e the melting of solid ice into liquid water) many do not (i.e. organic materials used in LCD displays), passing through one or more intermediate phases.

Experimentally, only a certain number of properties of a pure substance can be given a pure value. The relationship between these values is termed an equation of state and, for an ideal gas, is:

$$PV = nRT \qquad [3.12]$$

Where P is pressure, V is volume, T is temperature, n is the number of moles and R is the ideal gas constant. It follows that for a fixed amount of an ideal gas kept a fixed temperature, pressure and volume are inversely proportional. This relationship is known as Boyle's law and is the basis for the study of isothermal processes. Equations of state exist for liquids and solids as well, such as the one derived by van der Waals for liquids and solids:

$$\left(P + \frac{a}{v^2}\right)(v - b) = RT \qquad [3.13]$$

Where a and b are constants for gases and liquids, respectively. Solids generally have nearly linear isothermal relationships, a simple equation of state might be:

$$v = l + mT + nP \qquad [3.14]$$

A graphical representation of equations 3.12-3.14 is shown in figure 3.5 and accurately describes the pressure vs. molar volume relationship for bulk materials.

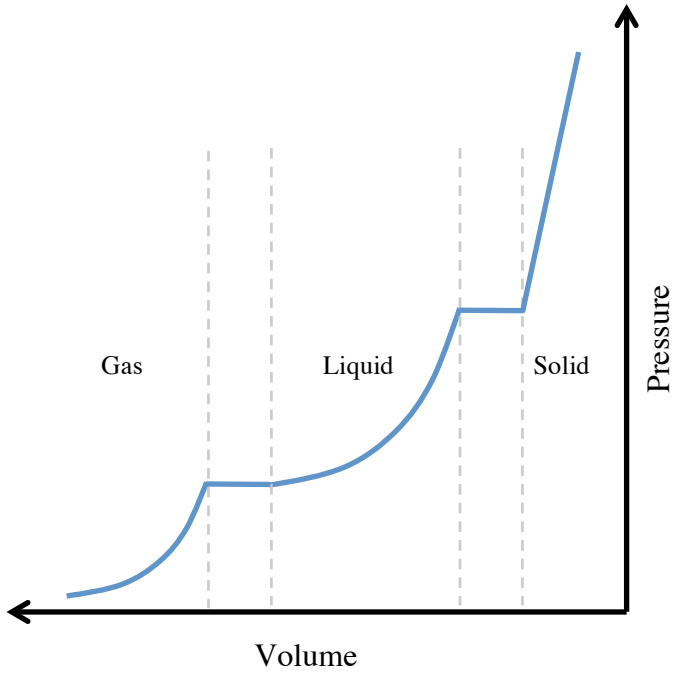

Figure 3.5: Graphical representation of the equations of state for the gaseous phase (eq 3.12), liquid phase (eq 3.13) and solid phase (eq 3.14) for an isothermal process. Constant pressure regions represent phase transitions.

To this point we have discussed three dimensional systems with the familiar solid, liquid and gas phases. While Langmuir films exist in two dimensions, a nearly analogous situation is observed when comparing the available surface area and surface pressure of the monolayer. Traditional Langmuir monolayers are comprised of amphiphillic molecules, species that exhibit both a polar group and non-polar group. As

the water molecule is highly polar such amphiphiles will organize at the water-air interface with their polar "head" groups submerged and non-polar "tails" extending out of the water subphase (figure 3.1). As the monolayer is compressed on a liquid surface, it will undergo phase transformations nearly analogous to those described in figure 3.5. The two dimensional equivalent of the pressure-volume isotherm is the surface pressure vs. surface area isotherm. For a typical long chain amphiphile, this relationship (figure 3.6) is nearly identical to the phase transitions for a three dimensional bulk solid.

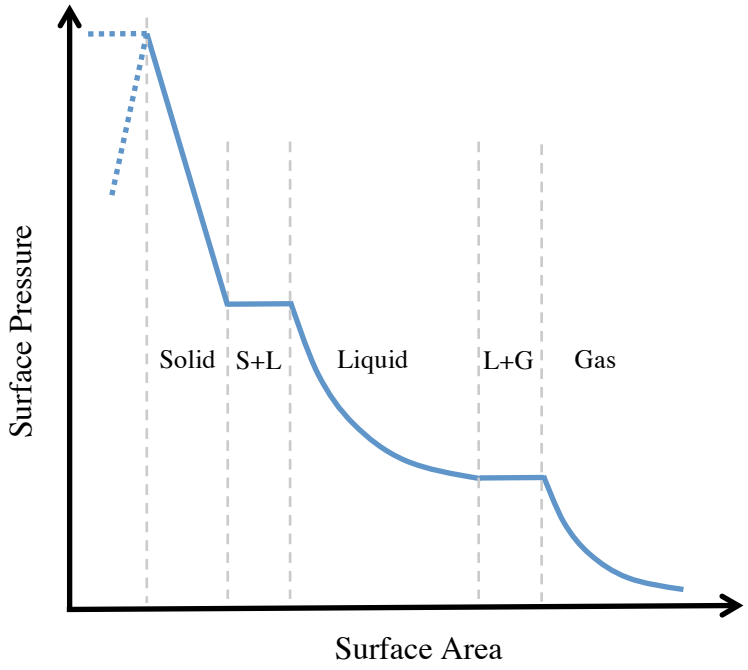

Figure 3.6: Surface pressure vs. surface area isotherm for a hypothetical long chain amphiphilic molecule.

Typically, the x axis (surface area) is divided by the total number of molecules deposited and expressed as a mean molecular area (MMA). The calculation is straightforward:

$$\mathrm{MMA} = \frac{[\mathrm{Area}]}{[\mathrm{Molarity}][\mathrm{Volume}][\mathrm{N_A}]} \qquad [3.15]$$

In the "gas" phase, the molecules are far enough apart that they exhibit minimal force on each other (figure 3.7a). As the surface area of the monolayer is reduced, the hydrophobic tails of the amphiphiles begin to interact with one another as the film enters the "liquid" phase, characterized by strongly interacting but randomly oriented hydrocarbon tails (figure 3.7b). The character of this liquid phase is highly dependent on the nature of the monolayer material in question; often multiple liquid phases appear as the monolayer undergoes orientational/entropic changes characterized by constant surface pressure regions (similar to those observed between solid, liquid and gas phases). The final phase of monolayer formation is the solid phase (figure 3.7c), characterized by a steep and nearly linear rise in surface pressure. After the maximum pressure is exceeded the monolayer will collapse (figure 3.7d), with varying degress of order highly dependent on the nature of the amphiphile. Two main types of collapse are observed in Langmuir films: "Constant pressure" collapse, where the pressure remains constant as the film is compressed beyond its minimum molecular area. This is indicated by a horizontal region of the isotherm at small areas and indicates material is removed from the monolayer under further compression, either aggregating at the trough edges / barriers, forming a disordered second layer atop the original monolayer, or dissolving in the subphase (dependent on the nature of the monolayer material). The second behavior observed post collapse is "constant area" collapse, where the pressure falls off drastically as the film is further compressed. This indicates a fracture into multilayered structures (figure 3.7d) and will, upon further compression, form ordered bi and trilayers depending on the mechanical properties of the molecule.

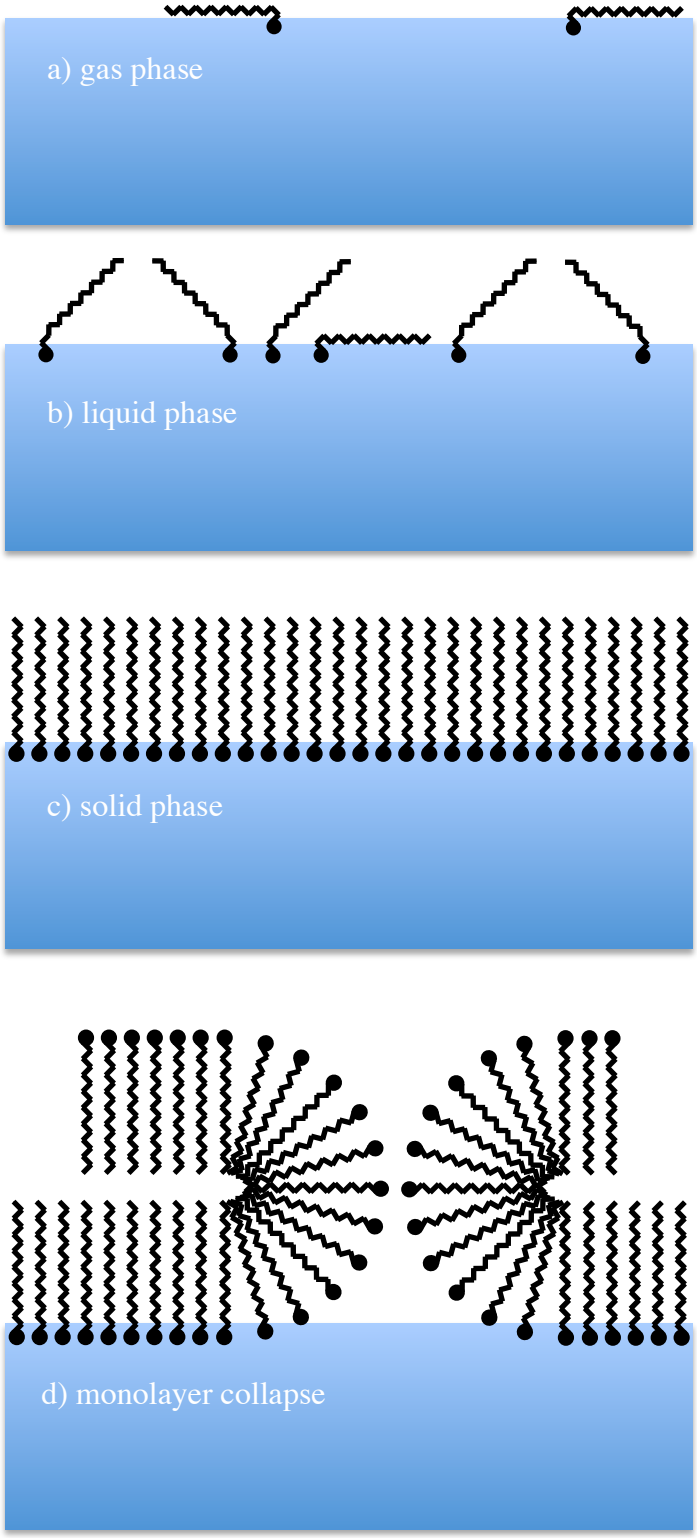

Figure 3.7: Stages of monolayer compression illustrating the gas, liquid and solid phases and eventual collapse.

3.4 Procedure for Isotherm Measurement

The Langmuir technique is one that requires exceptionally clean and pure surfaces and substances. Monolayers are extremely sensitive to surface contamination at concentrations as low as parts per million, so great care must be taken to minimize such contaminants. The UNC Charlotte Langmuir measurement setup is housed in a 4' free standing vertical laminar flow hood with a 90 fpm airflow through a 99.99% HEPA filter. Additionally, we have fabricated and installed a 48" x 36" acrylic sash on the front of the hood, fixed to ball bearing slides and a pulley system allowing both access to the trough area when the sash is raised and nearly complete isolation of the trough area when the sash is lowered. This setup affords us a Class 100 Cleanroom Classification ISO 5 environment to conduct our experiments. Housed within the hood is a KSV Nima Alternate Layer Deposition Trough placed on a granite surface on a (sub-hertz) vibration isolation table. This trough is actually comprised of two identical, isolated surfaces sharing a common subphase, each measuring 775 x 120 mm for a maximum spreading area of 930 cm^2. The minimum spreading area (barriers compressed fully) is 150 cm^2. The balance has a resolution of 4 μN/m and a range of 150 mN/m. The shared subphase has a volume of 6000 ml, allowing samples as large as 3 x 114 x 129 mm (i.e. a 4" wafer) to be passed through the dipping well. The trough is made from a single block of pure polytetrafluoroethylene (PTFE, "Teflon"), eliminating any possible contamination from glues or joint sealants. Further the hydrophobicity and non-reactivity of PTFE aids in maintaining a clean surface through the lifetime of the system. The barriers are made from polyoxymethylene (POM, "Delrin"), a thermoplastic with extremely high stiffness and dimensional stability.

The first step in the experimental procedure is cleaning the system. 20 ml of acetone is used to remove any initial contaminants in a quick wipe down of all surfaces with a lint free cloth. Following the acetone wipe, 50 ml of methanol is used to more thoroughly clean the trough and barriers (using fresh cloths), visually inspecting for any trace of contamination. Following the methanol clean the trough is quickly rinsed with DI water which is removed via aspiration and then a final wipe down with a dry lint free cloth. This procedure, while simple, is critical to the success of the experiment and must be done thoroughly and carefully.

After cleaning, the system is filled with 6000 ml of deionized (DI) water. Both ultrapure water (15 MΩ-cm) from a dedicated purification system as well as ASTM type II water (> 1.0 MΩ-cm) from a dedicated tap in Grigg Hall have been used. We have found nNo difference has been found between the two water sources in our experiments and have mainly used the ASTM II water as the source is in close proximity to our Langmuir system. This result is not surprising as 15 MΩ-cm water is an excellent solvent, easily contaminated by atmospheric gases. Ultrapure water exposed to atmosphere will dissolve CO_2 and reach a resistivity below 5 MΩ-cm within an hour[66], eventually reaching an equilibrium resistivity of 1.3 MΩ-cm due to the dissolved HCO_3^- and CO_3^{2-} ions.[67] The high surface area of the Langmuir system makes this technique even more susceptible to CO_2 dissolution, therefore ASTM II water will suffice. In order to reduce contamination further, 15' of perflouroalfoxy (PFA) tubing was plumbed from the DI water tap to the hood housing the system (previously we had (re)used 4 L polyethylene bottles).

Filling the trough with water should be done with the barriers in their closed position to minimize the initial area available for surface contamination. The trough should be filled to a slight meniscus above the trough edge (2-3 mm) as it will be cleaned by suction such that its final height will be even with the trough edge. Once the subphase is filled to a meniscus, the surface between the barriers is cleaned with an aspirator pump to remove any contaminants. Two to four minutes should be spent on this process, taking care to vacuum both the center of the trough and areas near the barriers as contaminants may have aggregated near the trough surfaces. Once cleaned sufficiently the barriers are opened and the Wilhelmy plate is installed to monitor surface tension. While the paper Wilhelmy plates are frequently replaced, no noticeable effect is seen as a function of age: a Wilhelmy plate previously used in several experiments produced the same results as a fresh one.

Once the barriers are fully open, the balance is zeroed, reading a surface pressure of 0.00 mN/m. Compressing the barriers on a clean surface should not change this value so long as no contaminants exist. In practice, a surface that exhibited a change of less than 0.30 mN/m was considered “clean” and produced repeatable and verifiable experimental results. If the change in surface pressure is measured to be higher than 0.30 mN/m, the barriers are recompressed and the area between them is further cleaned with the aspirator. This is repeated until the surface pressure change upon compression fell below the minimum threshold. It should be noted that the flow hood is kept “on” at all times during cleaning and setup in order to minimize outside contamination and did introduce +/- 0.10 mN/m uncertainty into our measurement, presumably the results of air currents acting on the low mass paper Wilhelmy probe. When the hood’s fans are turned

off, any noise in the system remains below the software's resolution of 0.01 mN/m. Another important aspect to note is the importance of the initial cleaning on the trough itself (prior to filling with water). During initial experiments it quickly became apparent that a thorough effort at this stage would significantly reduce the need for extensive surface cleanings and recompressions. An experienced user should be able reach the sub 0.30 mN/m threshold with only one aspirator cleaning round provided the initial solvent clean is done thoroughly and properly.

3.5 The Spreading Solution

Monolayer materials are dispersed in a suitable solvent (chloroform, toluene) which is then introduced to the subphase via a syringe or micropipette. Care should be taken when introducing the spreading solution onto the subphase surface, gently bringing the syringe in contact with the surface. The spreading solution will form a planar film on the surface, the solvent quickly evaporating leaving a sub monolayer of the surfactant molecules. It is helpful to understand the physical dimensions of this spreading layer when considering solvent evaporation. As our initial (fully expanded) trough area is 930 cm^2, we can determine film thickness as a function of volume deposited:

$$\text{film thickness (nm)} = 10.75 * \text{volume deposited (µl)} \qquad [3.16]$$

Spreading solutions are typically 5-100 µl, resulting in submicron spreading solutions. It is important to consider this dimension as the solvent's evaporation time is a function of

the layer thickness. Evaporation of solvents from a non-boiling liquid pool has been described with the following relationship:[68]

$$E = (4.66 * 10^{-6})u^{0.75}T_F M_w \left(\frac{P_S}{P_H}\right) \quad [3.17]$$

With variables defined as such:

E Evaporation rate [lbs/min/ft^2]

u Wind speed [mph]

P_S Vapor pressure of solvent [mm Hg]

P_H Vapor pressure of hydrazine [mm Hg]

M_w Molecular weight of solvent [g/mol]

T_F Solvent temperature correction factor:

$$T_F = \begin{cases} 1 & T_P < 0\ C \\ 1 + 4.3(10^{-3})T_P & T_P > 0\ C \end{cases} \quad [3.18]$$

Where T_P = solvent pool temperature [C]. The original authors used hydrazine as a reference, whose vapor pressure is well defined by:

$$\ln(P_H) = 65.3319 - \frac{7245.2}{T_H} - 8.22\ln(T_H) + 6.1557(10^{-3})T_H \quad [3.19]$$

Shown in figure 3.8. Note that T_H is the temperature of hydrazine in degrees kelvin.

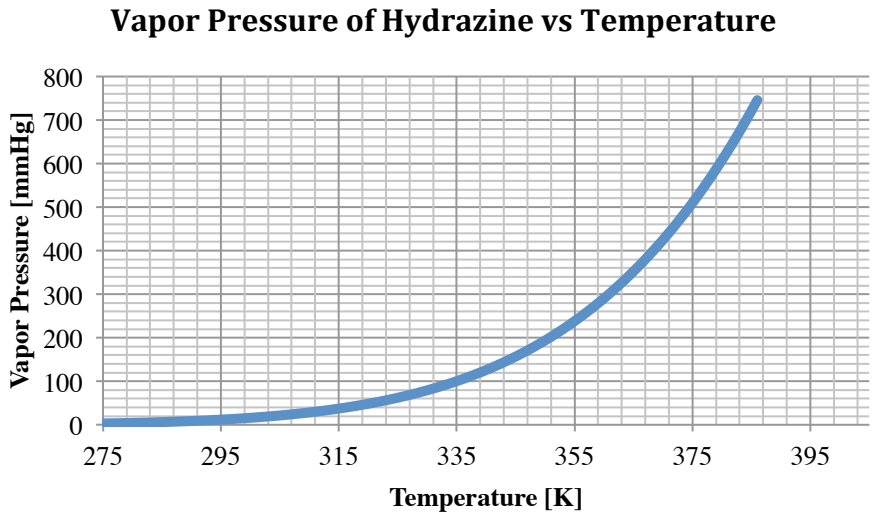

Figure 3.8: Empirically Determined Vapor Pressure of Hydrazine vs. Temperature, calculated from equation 3.19

Our Langmuir Blodgett trough is housed in a 90 fpm (1.02 mph) laminar flow hood kept at 24 ^{o}C, yielding the following relationship:

$$E = (1.29 * 10^{-6})M_w P_S \qquad [3.20]$$

We can therefore determine evaporation rates purely as a function of molecular weight and vapor pressure for spreading materials used in our experiments. For a 930 cm^2 spreading area we can determine volumetric evaporation rates for a variety of spreading materials (figure 3.9).

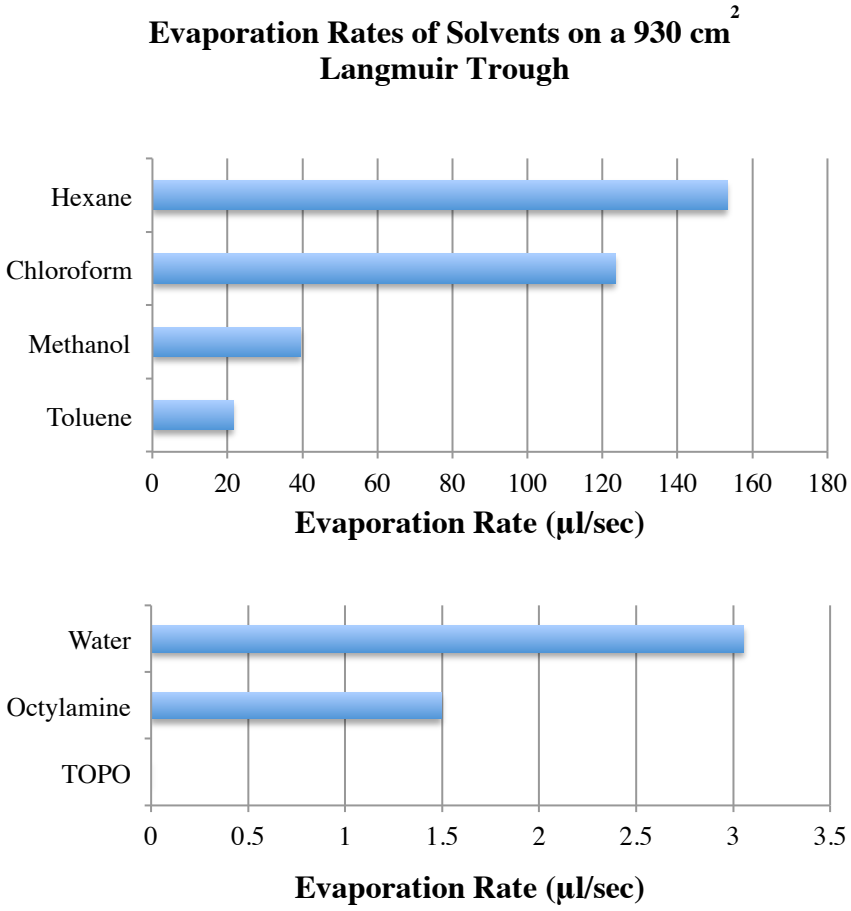

Figure 3.9: Evaporation rates of common solvents and ligands on a 930 cm^2 area. Temperature and airflow assumed to be 24°C and 90 fpm, respectively, simulating the conditions at the Langmuir trough surface.

We have experimentally verified these evaporation rates by monitoring surface pressure as a function of time after depositing large amounts of pure solvents. We begin by preparing a clean surface as previously described and depositing 2500 µl of pure solvent passed through a 0.2 µm filter. Recalling equation 3.16, a 2500 µl film on a 930 cm^2 surface is 27 µm thick. The solvent layer on top of the water subphase affects the surface pressure, allowing us to detect the presence of the liquid phase solvent layer by monitoring the surface pressure reading and ultimately determine evaporation rates. The

surface pressure returning to 0 mN/m (the value measured on a clean water subphase) is a result of the absence of any solvent layers, indicating complete evaporation. Figure 3.10 depicts such an experiment using 2500 µl of toluene deposited at t = 38 s.

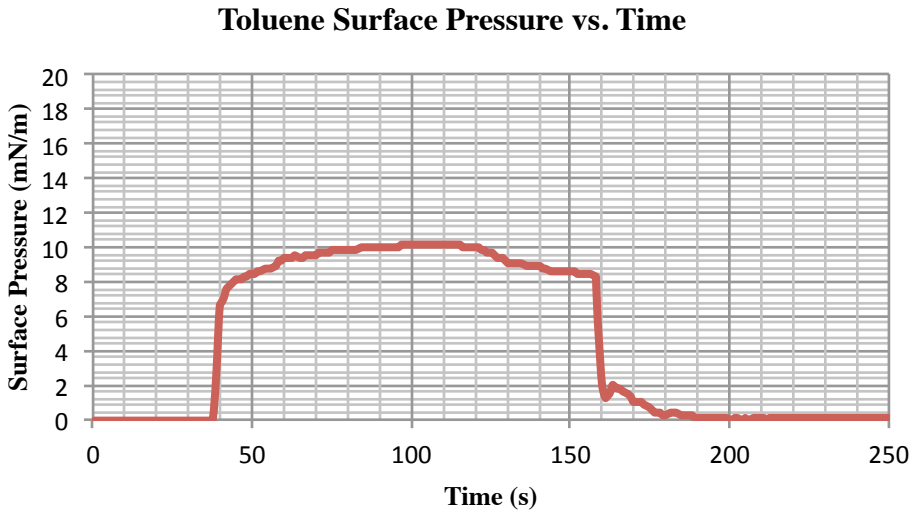

Figure 3.10: 2500 µl of pure toluene was deposited on a clean water subphase at t = 38 s. Complete evaporation of the solvent is indicated by the steep drop in surface pressure at t = 159 s.

In this experiment we measured an evaporation rate of 20.7 µl/sec, close to our predicted value of 21.5 µl/sec using equation 3.20. This is an important result as it illustrates the speed with which a solvent with relatively low volatility will evaporate. Note that chloroform, another common solvent in spreading solutions, will evaporate at nearly six times the rate of toluene. The end result is that with the low volumes of spreading solutions we are using (< 100 µl) the solvent spends very little time on the subphase surface before evaporating.

3.6 Results and Discussion

A common monolayer material used to characterize Langmuir systems is octadecanoic (stearic) acid. This saturated carboxylic acid forms highly ordered monolayers on pure water subphases before a sharp collapse (figure 3.11) at approximately 55 mN/m. Initially a 0.01 M stearic acid solution was prepared by dissolving 2.85 g stearic acid in 100 ml of chloroform (yielding a 0.1 M solution) and then further diluted 10:1 to yield a 0.01 M solution. 22 µl of this solution was deposited on a clean Langmuir trough and compressed at 30 mm/min while monitoring the surface pressure.

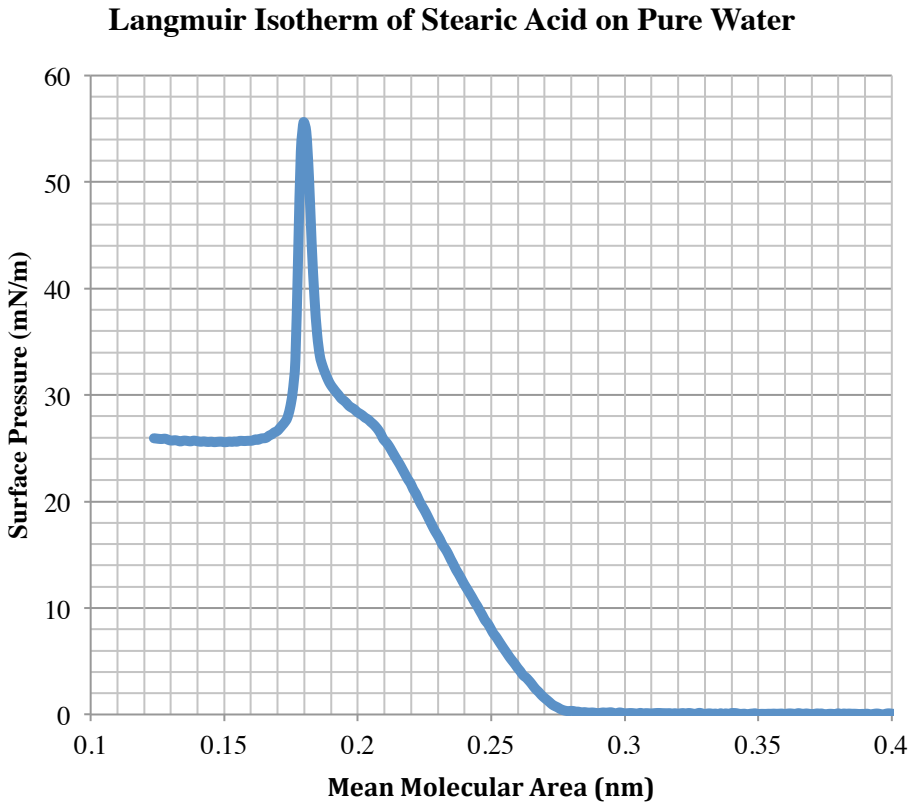

Figure 3.11: Langmuir isotherm of stearic acid on pure water subphase. Monolayer exhibits constant area collapse behavior.

The stearic acid isotherm in figure 3.11 clearly shows the phases seen in a typical amphiphilic isotherm. Above mean molecular areas of 0.3 nm^2/molecule, the stearic acid is in the gas phase with surface pressures well below 1 mN/m. Between 0.27 and 0.21 nm^2/molecule, the film is in the liquid (expanded) phase where the molecules begin to interact with each other (figure 3.7b). The solid phase between 0.18 – 0.19 nm^2/molecule corresponds to the highest density of any phase, with the hydrocarbon chains aligned and sticking out of the water subphase. The behavior beyond this collapse shows constant area behavior, exhibiting a steep collapse beyond 0.18 nm^2/molecule, indicating film fracture during multilayer formation (figure 3.7c).

An interesting property of stearic acid monolayers is their ionic nature and strong dependence on the subphase composition. While a stearic acid monolayer on a pure water subphase exhibits constant area collapse behavior, the same monolayer placed on a 0.5 mM $MnCl_2$ subphase exhibits significantly different constant pressure collapse behavior (figure 3.12). The $MnCl_2$ in the subphase will react with the surface groups of the stearic acid monolayer:

$$2\ CH_3(CH_2)_{16}COOH + MnCl_2 = Mn(CH_3(CH_2)_{16}COO^-)_2 + HCl \qquad [3.21]$$

The interaction of the divalent cation with the stearate head groups stabilizes the monolayer, preventing the constant area collapse behavior seen in figure 3.11. The stearic acid film instead exhibits constant pressure collapse behavior, maintaining high

surface pressures that suggest a stable surface layer upon further compression (figure 3.12).

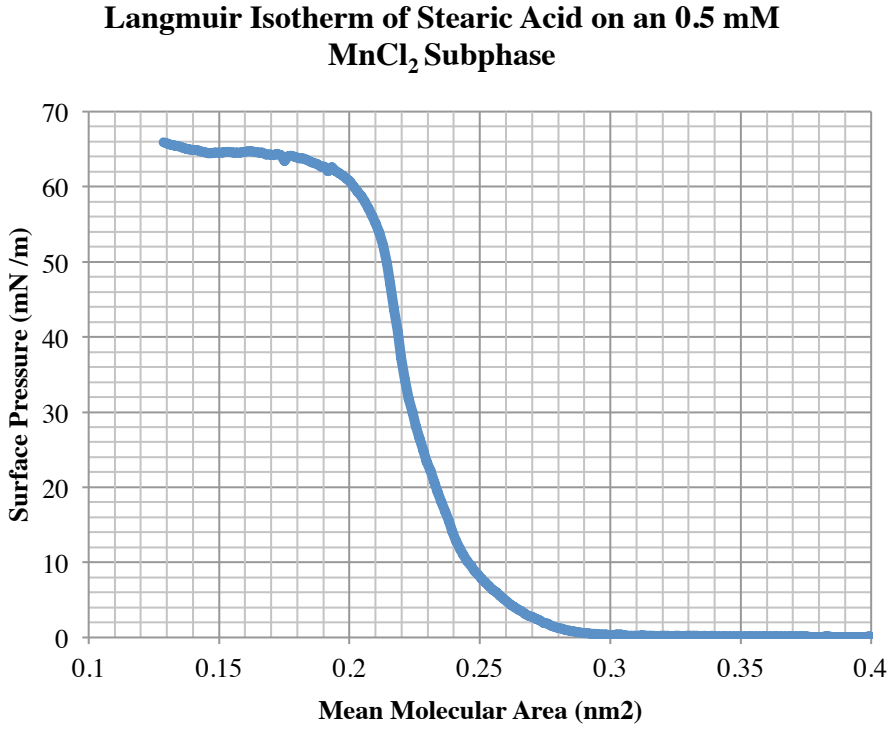

Figure 3.12: Langmuir isotherm of stearic acid on 0.5 mM $MnCl_2$ subphase. Monolayer exhibits constant pressure collapse behavior.

The stearate salt formation is favored by a high pH, so we would expect an acidic subphase to display constant area collapse behavior regardless of salt concentration. We prepared a 0.001 M HCl subphase (pH = 3) and measured the monolayer behavior of stearic acid both with and without the addition of manganese chloride to the subphase, shown in figure 3.13:

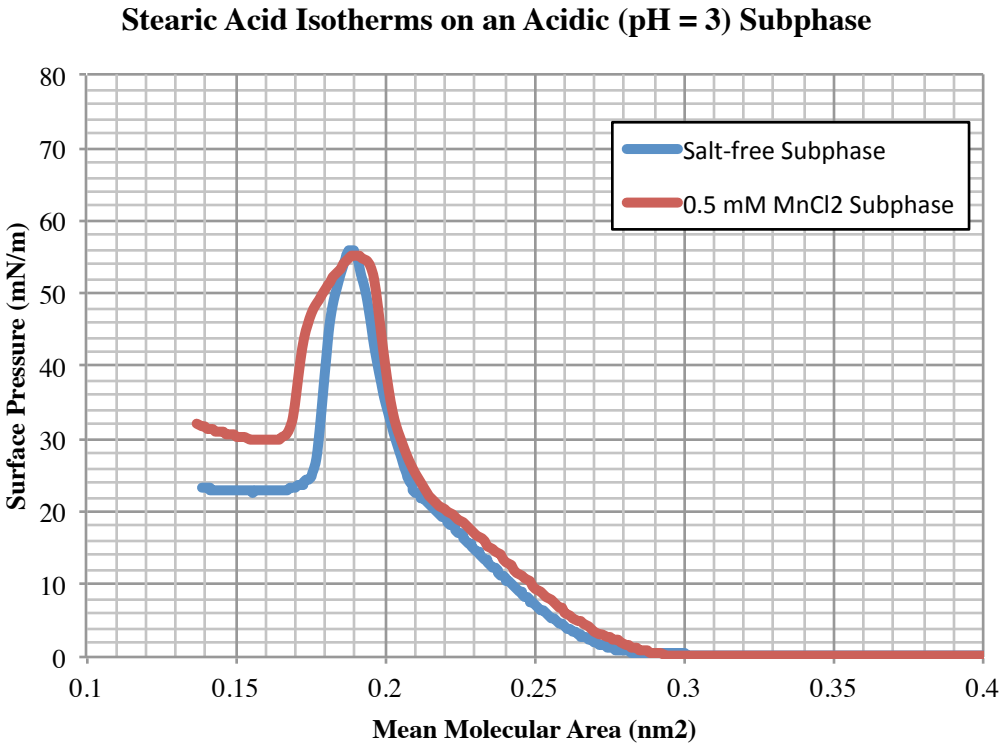

Figure 3.13: Langmuir isotherm of stearic acid on an acidic subphase (0.001 M HCl). Monolayer exhibits constant area collapse behavior regardless of the presence of salts in the subphase.

Furthermore, subphases with high pH values should encourage salt formation and thus more stable monolayers exhibiting constant pressure collapse behavior. We prepared a 0.001 M KOH (pH = 11) subphase and measured the monolayer behavior of stearic acid both with and without the addition of manganese chloride to the subphase, shown in figure 3.14:

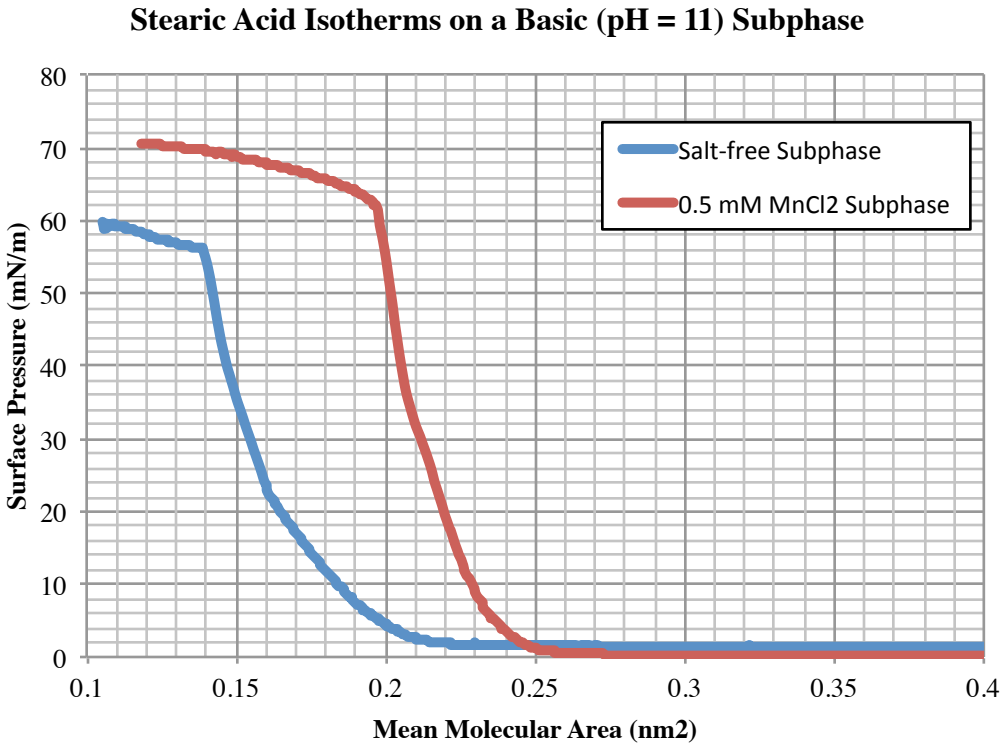

Figure 3.14: Langmuir isotherm of stearic acid on an basic subphase (0.001 M KOH). Monolayer exhibits constant pressure collapse behavior regardless of the presence of salts in the subphase.

A notable feature of the salt-free basic subphase isotherm is the drastically lower collapse area (0.14 nm^2) compared with the typical ~0.20 nm^2 area characteristics of stearic acid. As this smaller area is not physically realistic this can be interpreted as a loss of materials from the subphase, likely due to the enhanced solubility in basic solutions.

Another monolayer material relevant to our studies is trioctylphosphine oxide (TOPO), a common ligand used to passivate cadmium selenide (CdSe) nanocrystals. TOPO passivated CdSe nanocrystals in solution require an excess of free TOPO to enhance stability, so it is important to understand the behavior of this free TOPO as a monolayer material. Unlike the easily dissociated stearic acid, the polar phosphine oxide head group is extremely stable and insensitive to changes in pH or ionic strength of the subphase. Figure 3.15 shows several TOPO isotherms with varying subphase pH and salt concentrations. Unlike stearic acid films, TOPO monolayers exhibit no clear distinctions between phases and show constant pressure collapse behavior regardless of the subphase: Variations in pH and ionic strength have little effect on the isotherm. In addition to the uncharged head group (responsible for the constant pressure collapse behavior) the large, sterically demanding nature of the aliphatic tails results in a lack of a clear phase transition between the liquid (expanded) and solid (compressed) states.

The final amphiphilic monolayers we analyzed were mixed isotherms containing both TOPO and stearic acid monolayers in varying molar fractions. Understanding the behavior of mixed isotherms is critical to understanding the behavior of nanocrystal isotherms, as nanocrystal spreading solutions will typically have excess free ligands in solution. If the concentrations and mean molecular areas of the constituent monolayer materials are known, we can predict the mean molecular area of the resulting mixed monolayer:

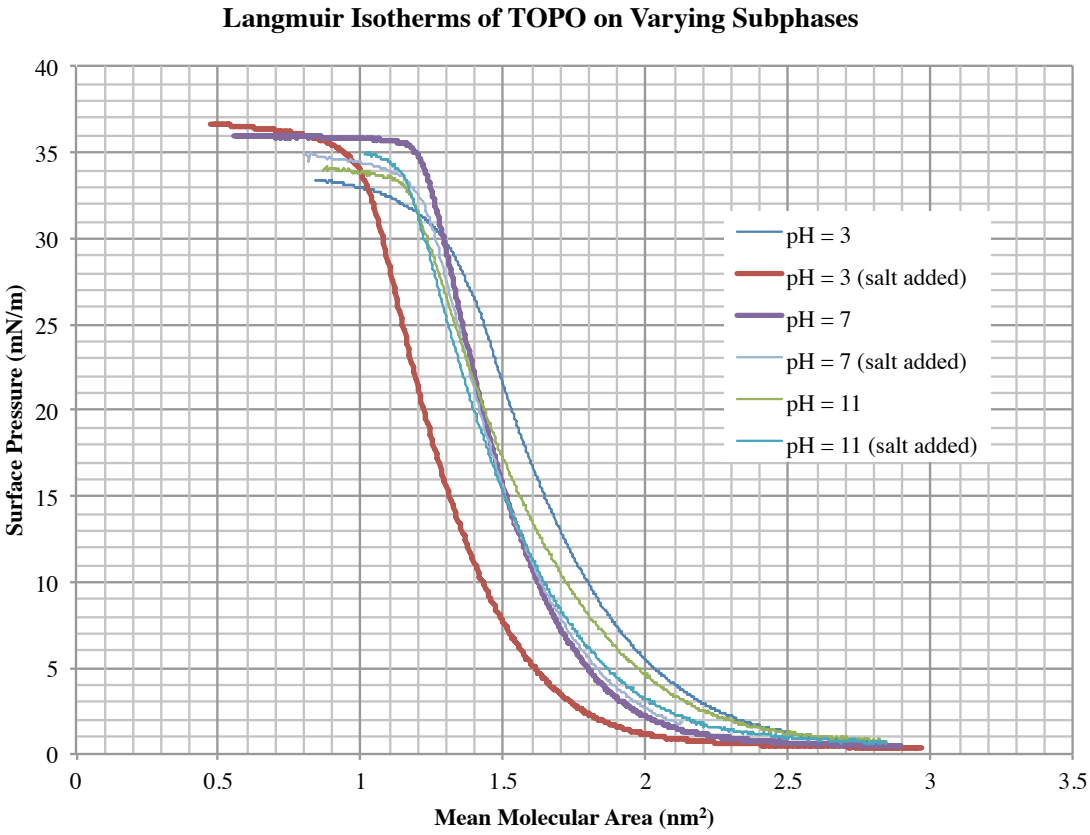

Figure 3.15: Langmuir isotherms of TOPO on varying subphases. Both pure and salt containing subphases were examined at acidic, neutral and basic pH values.

If the concentrations and mean molecular areas of the constituent monolayer materials are known, we can predict the mean molecular area of the resulting mixed monolayer:

$$a_{1n} = x_1 a_1 + x_2 a_2 + x_3 a_3 + \cdots x_n a_n \qquad [3.22]$$

For an n component film where a is the molecular area and x is the molar fraction. For our purposes we will be using the two component form of equation 3.22:

$$a_{12} = x_1 a_1 + x_2 a_2 \qquad [3.23]$$

A film comprised of TOPO (molecular area = 1.7 nm) and stearic acid (molecular area = 0.2 nm) thus should have predictable molecular areas based on the relative concentrations of the materials. Figure 3.16 depicts eleven isotherms of such mixed films, varying in molar concentration from 100% TOPO to 0% TOPO (100% stearic acid) in 10% intervals. These films were studied by preparing 0.1 M concentrations of both stearic acid and TOPO in toluene. These solutions were combined in the appropriate ratios and further diluted with fresh toluene to produce solutions with a total molarity of 1.0 mM.

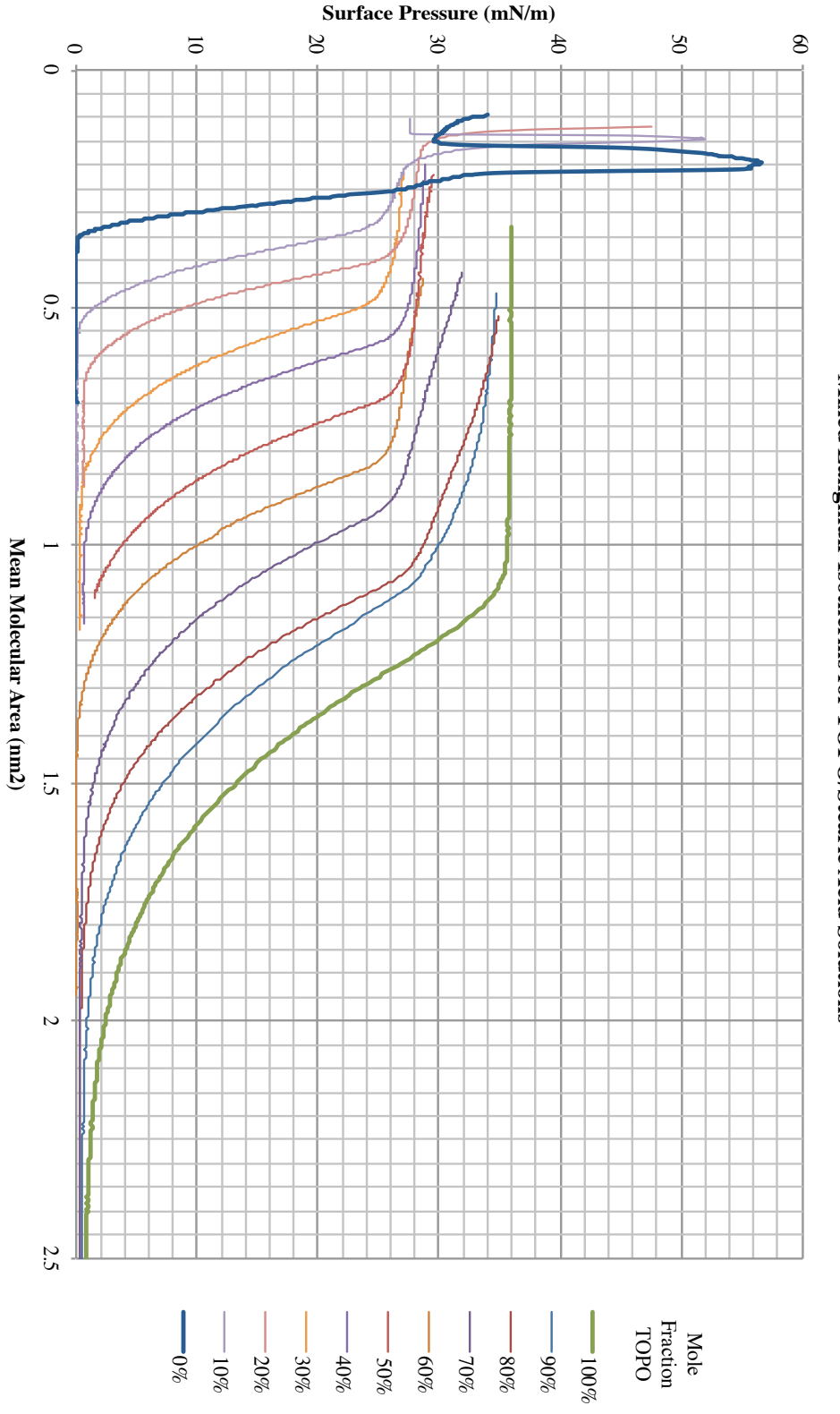

Figure 3.16: Langmuir isotherms of mixed TOPO / stearic acid monolayers of varying molar fractions.

The isotherms in figure 3.16 have limiting molecular areas (defined as the x intercept of the steepest portion of the isotherm) predicted by equation 3.23:

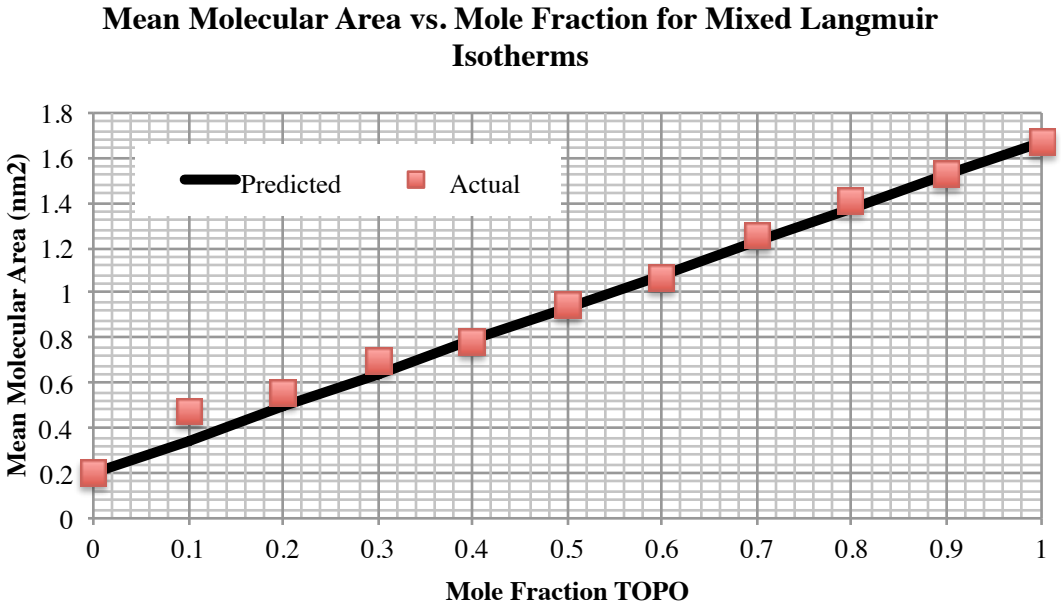

Figure 3.17: Observed limiting molecular areas for monolayer films composed of TOPO and stearic acid in toluene.

A final aspect of the Langmuir isotherm to consider is the compressibility (C) of the film. Again using the analogy of a three dimensional bulk material, we can evaluate C from the slope of the surface pressure – surface area isotherm:[65]

$$C = -\frac{1}{a}\left(\frac{\partial a}{\partial \Pi}\right)_{T,P,n} \qquad [3.24]$$

Where a is the surface area and Π is the surface pressure. Temperature, pressure and the number of molecules (T, P, and n respectively) are held constant. Compressibility gives us a quantitative measure of the different phases of a monolayer and can be useful when comparing different types of molecular monolayers. Revisiting the stearic acid monolayer behavior we can apply equation 3.24 and plot these relationships in figures 3.18 and 3.19.

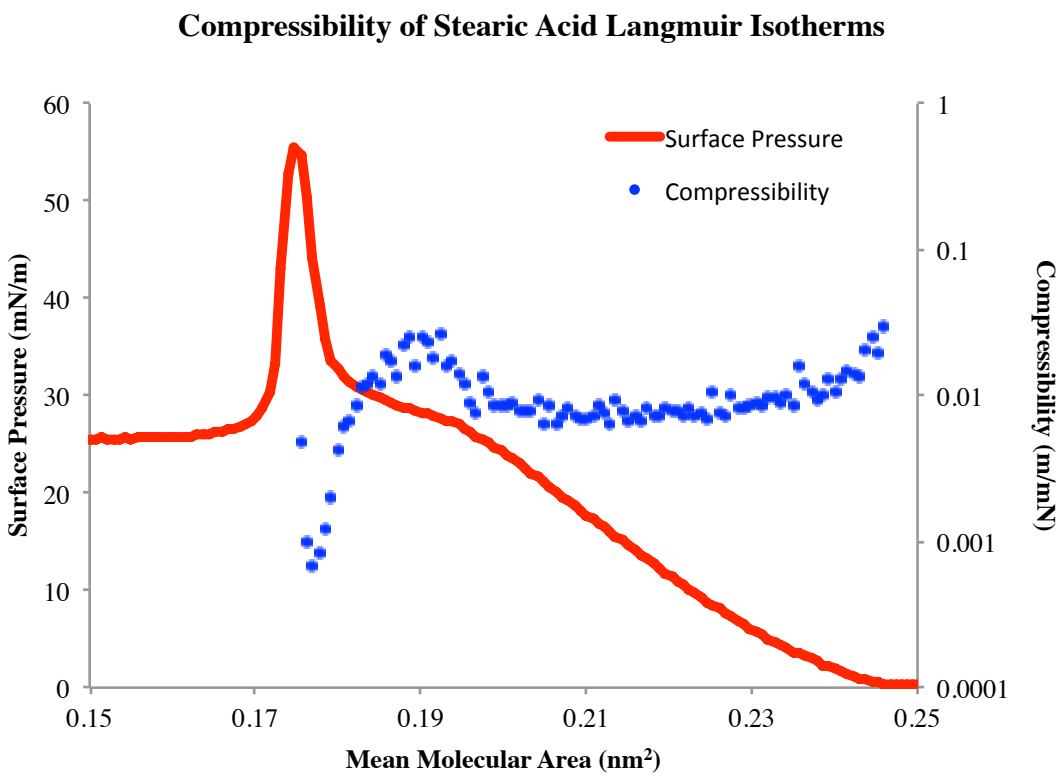

Figure 3.18: Compressibility of stearic acid monolayers on a pure water subphase.

Compressibility is typically reported as the minimum compressibility (maximum slope) of a given isotherm or region of an isotherm. In our studies, stearic acid on pure water exhibits a compressibility of 6.5 x 10^{-3} m/mN in the expanded phase and 6.7 x 10^{-4} m/mN in the condensed phase (figure 3.18). Minimum compressibility varied within ± 1.0 x 10^{-4} m/mN across separate isotherms. These values are consistent with other similar carboxylic acids reported by other groups in the literature.[69] Addition of salt to the subphase results in a less rigid monolayer, with a measured minimum compressibility of 2.1 x 10^{-3} m/mN (figure 3.19). This is consistent with our understanding of the divalent cation interaction with the dissociated carboxylate head group on the water surface: bridging action by Mn^{2+} ions in solution result in larger intermolecular distances (between neighboring stearic acid molecules) than seen in pure water subphases. These films therefore exhibit slightly more compressibility than their closer packed pure water counterparts. Note that discernable phases do appear in the compressibility data in figure 3.19, suggesting that while phase transitions are not as well defined as on pure water subphases, expanded and compressed regions of the monolayer still exist in these films.

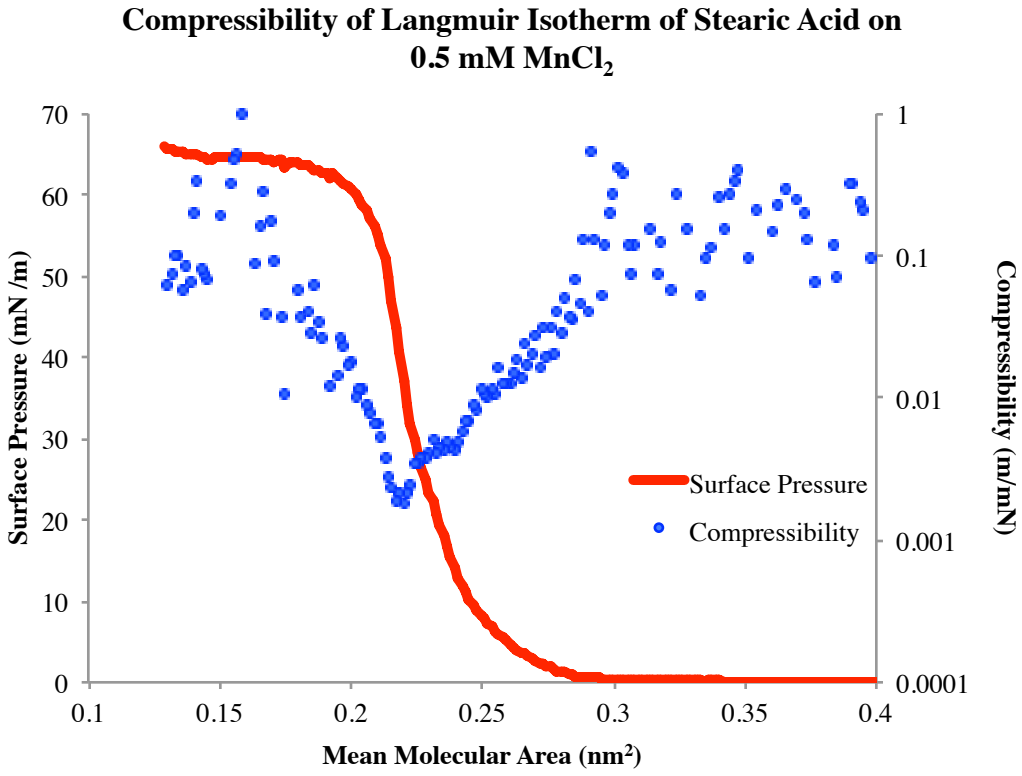

Figure 3.19: Compressibility of stearic acid monolayers on an ionic subphase.

TOPO isotherms exhibit significantly higher compressibility than stearic acid due to the sterically demanding nature of the three octyl chains (figure 3.21). While stearic acid monolayer compression is ultimately limited by repulsion of the head groups, TOPO monolayer compression is limited by the large cone angle afforded by the hydrocarbon tails. This affords a higher compressibility (less rigid film) that decreases as the film is further compressed. Minimum compressibility in our films was measured at 10^{-2} m/mN (figure 3.20), much higher than that measured for the stearic acid monolayers.

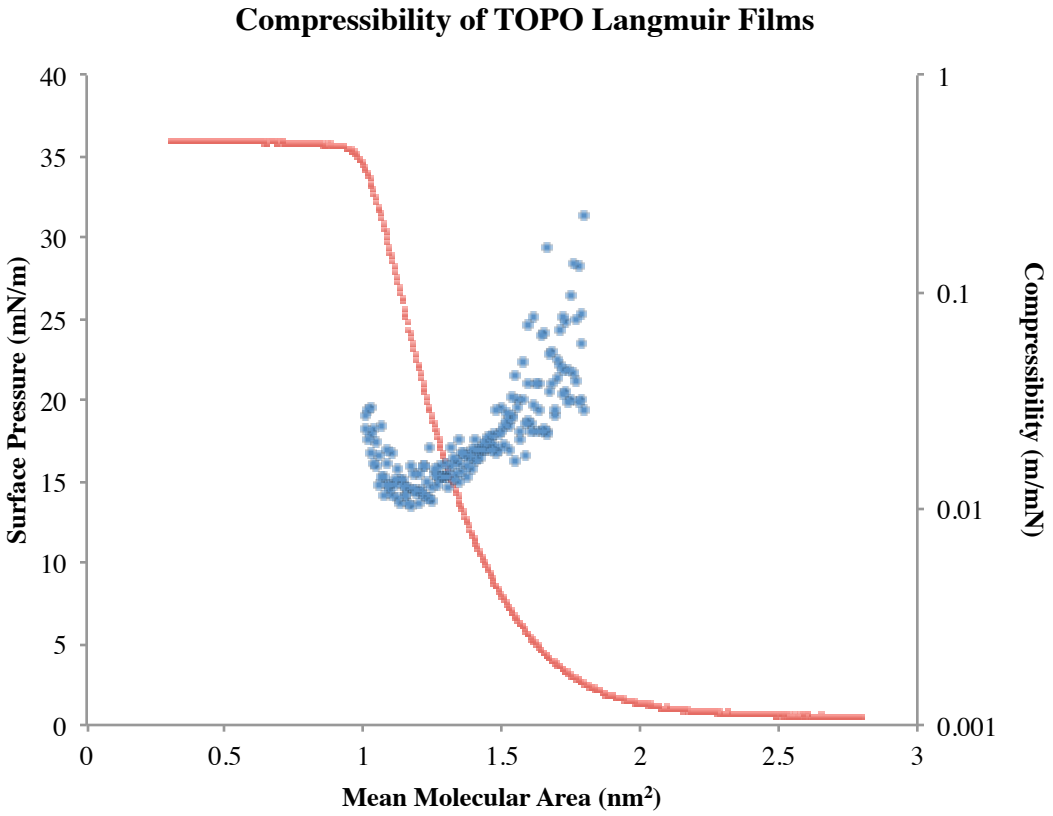

Figure 3.20: Compressibility of trioctylphosphine oxide monolayer on a pure water subphase.

CHAPTER 4: LANGMUIR FILMS OF CdSe NANOCRYSTALS

4.1 Background and Prior Art

Nanocrystal monolayers are substantially different than amphiphilic monolayers in that they exhibit an entirely non polar surface: the head groups of the passivating ligand (in this case, phosphine oxide on the TOPO ligand) are bound to the nanocrystal surface with their aliphatic tails facing outwards (figure 4.1). This results in an entirely hydrophobic surface that has no preferential orientation on a water-air interface. Such

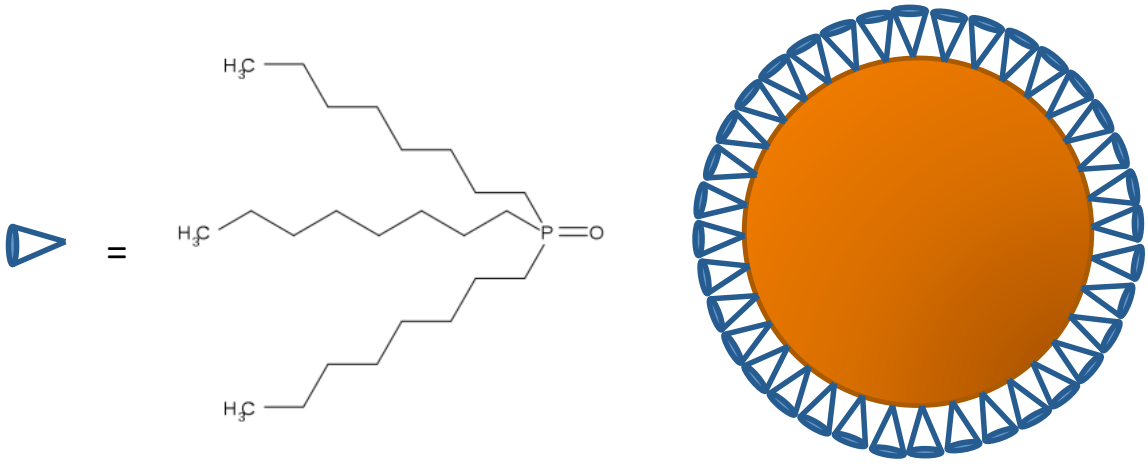

Figure 4.1: Cross section of a CdSe nanocrystal passivated with TOPO ligands. The polar phosphine oxide headgroups are bound to the nanocrystal surface, while the hydrophic tails are radially oriented outward, presenting a hydrophobic surface.

Langmuir Blodgett films of CdSe nanocrystals were first investigated by Daboussi and Bawendi at MIT in 1993.[70] They employed spreading solutions of 5-10 mg/ml of TOPO capped CdSe nanocrystals dispersed in chloroform and observed collapse pressures around 65 mN/m for nanocrystals of varying sizes (2.5, 3.0, 3.6, 4.3, 5.3 nm diameters). While film compressibility was not reported, extrapolation from the published isotherms suggests values of 10^{-2} m/mN for all nanocrystal sizes. All nanocrystal films exhibited constant pressure collapse behavior (as one would expected) due to the uncharged nature of the hydrocarbon surface. Furthermore a rinse process was described to reduce the amount of free TOPO in solution. A two solvent method is used to remove free TOPO: TOPO-capped nanocrystals are insoluble in methanol while free TOPO is readily dissolved. Nanocrystal / free TOPO solutions are thus separated by adding methanol until nanocrystal precipitation, then discarding the methanol/TOPO supernate before redissolving the precipitated nanocrystals in a suitable solvent (chloroform, toluene, hexane, etc). The next decade saw several reports of further Langmuir Blodgett manipulation of CdSe-TOPO monolayers with maximum surface pressures ranging from 20 – 60 mN/m.[71-76] This wide range of surface pressures speaks to the difficulty of preparing such monolayers: lower collapse pressures and higher compressibilities indicate significant amounts of excess TOPO in solution. As seen in figure 3.16, collapse pressures of multi component films are lower than they are for pure films. The failure to account for the excess ligand in solution is responsible for the largely inconsistent results, varying film morphologies and differing collapse pressures observed in the literature.

4.2 Initial Studies

The first efforts at producing monolayers of CdSe nanocrystals employed commercially available materials: "Evidots" purchased from Evident Technologies in Troy, NY; and "TriLite Nanocrystals" purchased from Crystalplex in Pittsburgh, PA. While the Evidots were size tunable CdSe nanocrystals, the Trilite NCs were composition tuned, employing a $CdSe_xS_{1-x}$ core to achieve a range of emission wavelengths while maintaining a consistent 5.5 nm diameter across a range of colors. Furthermore, both manufacturers reported concentration as mass per volume (mg/ml). As the manufacturers also reported molecular weights for these materials (accounting for both the core and ligand shell), the amount of spreading solution that should produce a monolayer at 400 cm^2 was calculated, roughly half the area of the trough with the following equation:

$$Volume\ [uL] = \frac{4*10^{22}}{N_A*PMA}\frac{FW}{C} \qquad [4.2]$$

Where C is the concentration in mg/ml, PMA is the predicted molecular area in nm^2, N_A is Avogadro's number, and FW is the formula weight of the nanocrystal in g/mol. The given molecular weights (~10^5 g/mol) and concentrations (5-20 mg/ml) suggested spreading solution volumes of 30-120 μl would yield close packed monolayers at 400 cm^2. The majority of this early work was done on the TriLite NCs (alloy cores), which made it difficult to verify concentrations spectroscopically. The alloy composition and exact size of the nanocrystals were proprietary, and transmission electron microscopy (TEM) studies revealed that the TriLite materials were actually large (10 nm) pyramid like structures, not the pseudo-spherical 5.5 nm crystals described by the manufacturer

(figure 4.2). Without further knowledge of the alloy composition an extinction coefficient could not reliably identified to use in absorption measurements.

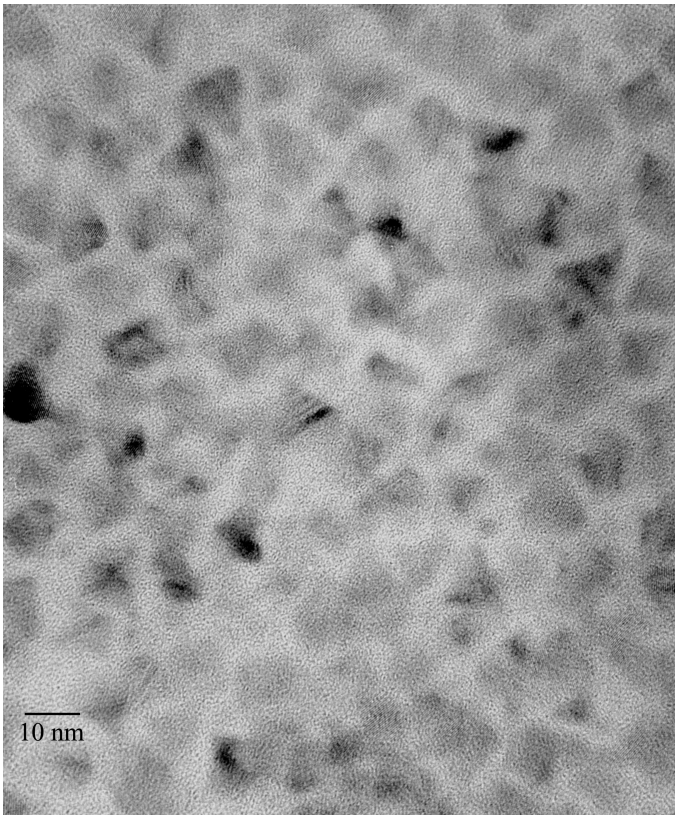

Figure 4.2: TEM of Crystalplex TriLite nanocrystals, revealing pyramid like structures with ~10 nm edge lengths.

Isotherms similar to those in the literature were observed at much higher molecular areas than expected (figure 4.3). This could be explained by a higher than actual value for formula weight or a lower than actual value for concentration or predicted molecular area. It was initially suspected the pyramidal morphology of the crystals was a major source of error, but geometric analysis shows that both the volume and cross sectional

area of a 10 nm edge length pyramid is quite close to the respective dimensions of a 5.5 nm sphere.

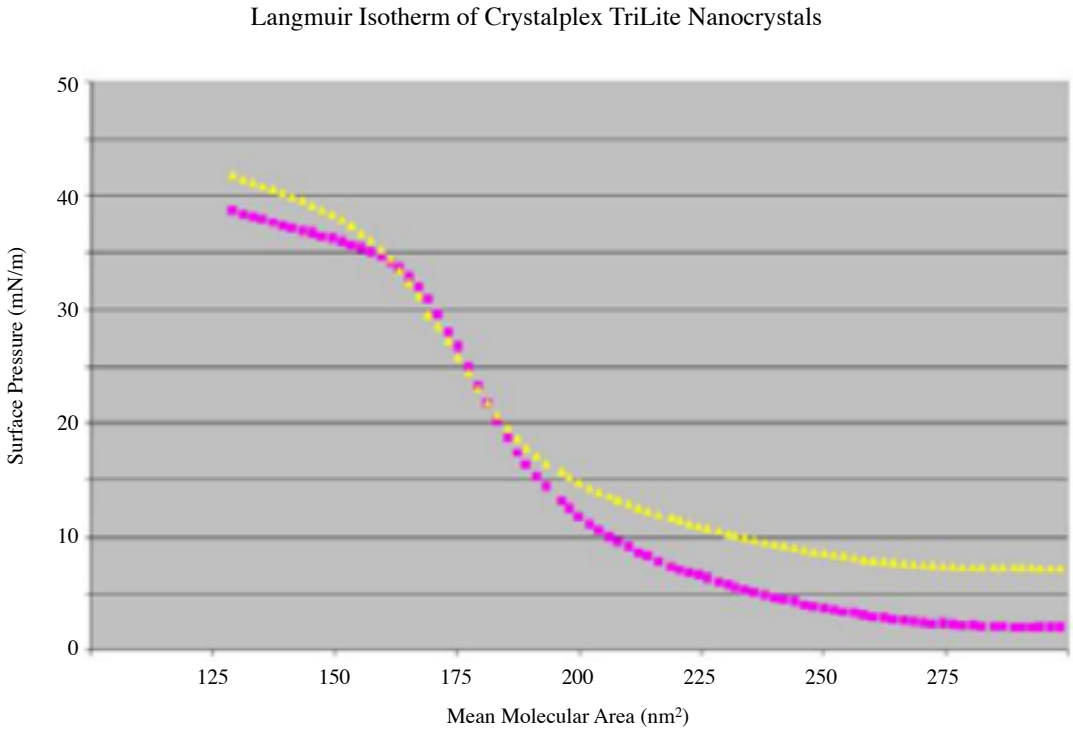

Figure 4.3: First Langmuir isotherm taken of Crystalplex TriLite Nanocrystals. 10 µl of a 20 mg/ml spreading solution was deposited on a pure water subphase and compressed at a rate of 30 mm/min.

Furthermore, the formula weight given was consistent with the density and volume of the nanocrystals. At the time, the reported concentrations of the commercial materials were not questioned beyond verifying the value with the manufacturer. The deposited films of core-shell dots (CdSeS cores with a monolayer of ZnS on the surface) produced visible luminescence (figure 4.4).

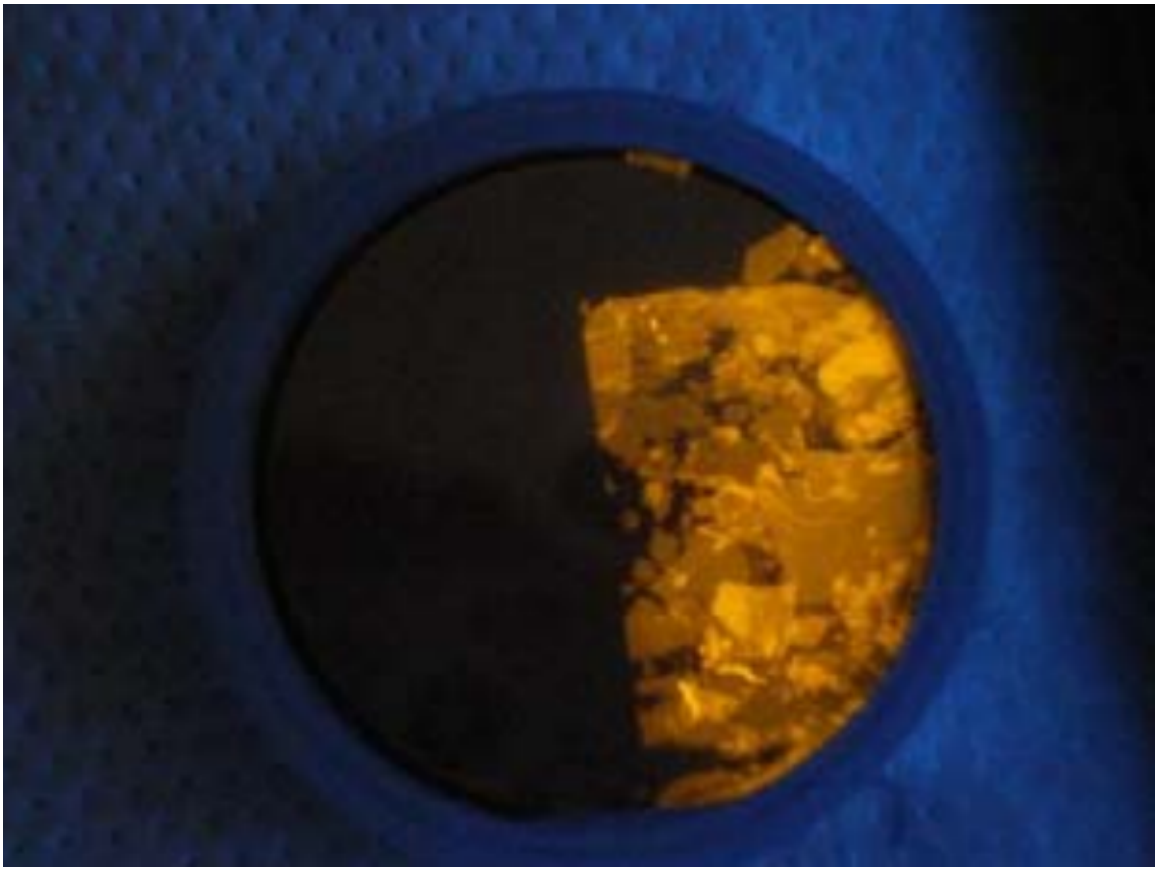

Figure 4.4: Fluorescence image of TriLite Nanocrystal Langmuir Blodgett films on GaN wafer.

These films, while having the expected photoluminescent effects, possessed no electrical conductivity and produced shorted vertical devices. Scanning electron microscopy of the films revealed sparse, network like structures with expansive voids in between them (figure 4.5). Interestingly, it was evident that the nanocrystals were forming multilayers within these network-like structures, indicated by darker areas in the image A great deal of time was spent exploring different techniques and variables: using differing concentrations of spreading solutions, differing barrier compression speeds,

varying subphase pH and ionic strength, varying anneal times, etc. but had limited success in solving this problem: every film examined had large voids rendering device engineering impossible. One area that did produce repeatable and notable results was pretreating the substrate to lower the surface energy (promoting nanocrystal adhesion) prior to deposition.

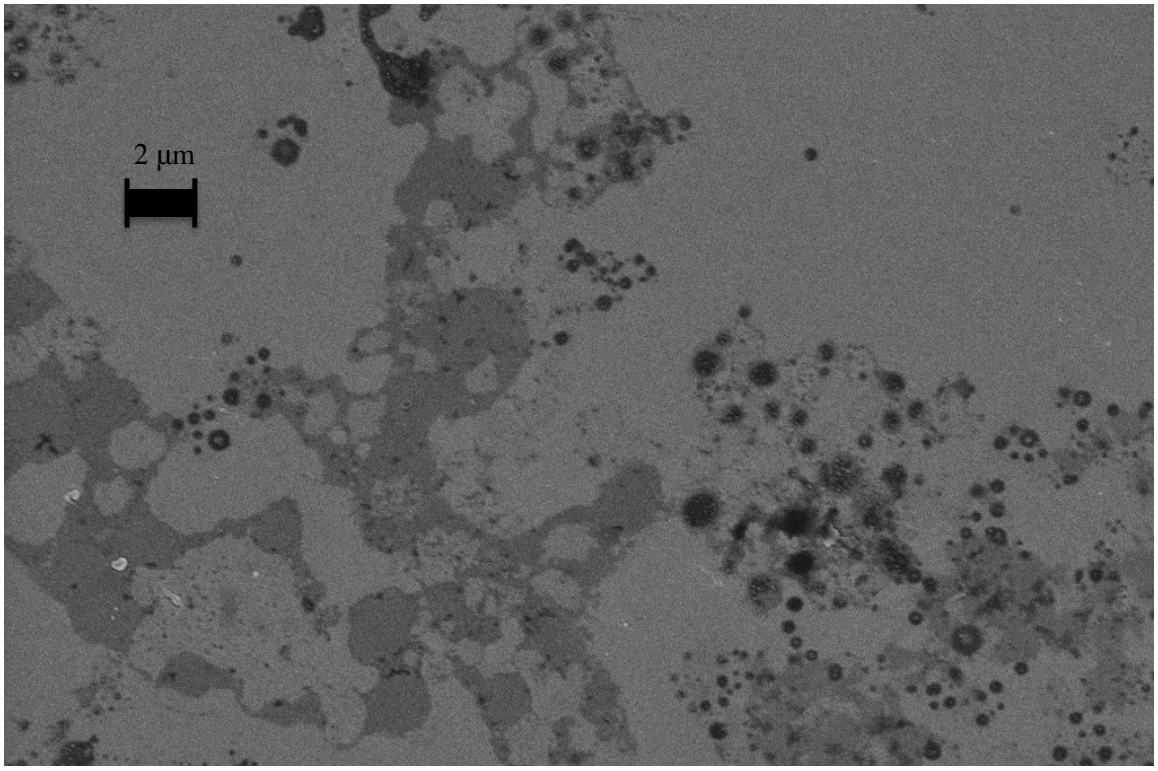

Figure 4.5: SEM image of a Langmuir Blodgett film of CdSeS nanocrystals on ITO. Dark grey areas are nanocrystal films with darker areas representing nanocrystal multilayers.

4.3 Substrate Surface Energy Modification

TOPO coated CdSe nanocrystals have very low energy surface and adhere well to low surface energy (hydrophobic) substrates. Hydrophilic substrates however, often show dewetting (figure 4.6), which can result in the formation of QD cellular networks due to favorable hydrogen bonding between the substrate and water from the Langmuir subphase. Plotting the free energy as a function of concentration (figure 4.7) two minima are observed. It was hypothesized that TOPO-capped CdSe QDs on hydrophilic substrates exist between these two minima, leading to a spinodal decomposition where QDs diffuse to high concentrations in localized areas, and are void in other areas. This spinodal decomposition is well described by the Cahn-Hilliard equation:

$$\frac{\partial c}{\partial t} = D\nabla^2(\mathrm{c}^3 - \mathrm{c} - \gamma\nabla^2\mathrm{c}) \qquad [4.3]$$

Using a linearly stabilized integration scheme in MATLAB, a uniform film undergoing spinodal decomposition (figure 4.10) was modeled. The results were in good agreement with the cellular networks have observed, and suggest that stable Langmuir films of hydrophobic particles (i.e. any nanocrystal that would form a stable Langmuir film) are in fact unstable on hydrophilic substrates. Furthermore, the more hydrophobic a substrate is, the more stable and uniform one would expect QD monolayers on it to be.

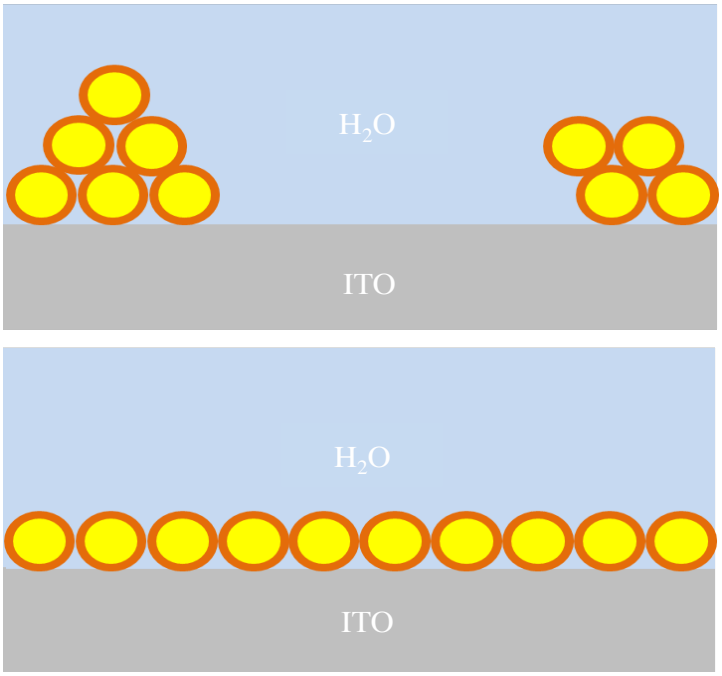

Figure 4.6: (top) ITO surface after solvent (acetone, methanol) clean. As a result the nanocrystals and water molecules phase segregate on the high energy surface forming cellular networks. (bottom) ITO surface after acid treatment, rendering the surface hydrophobic. Nanocrystals on this surface will remain stable as smooth, ordered monolayers.

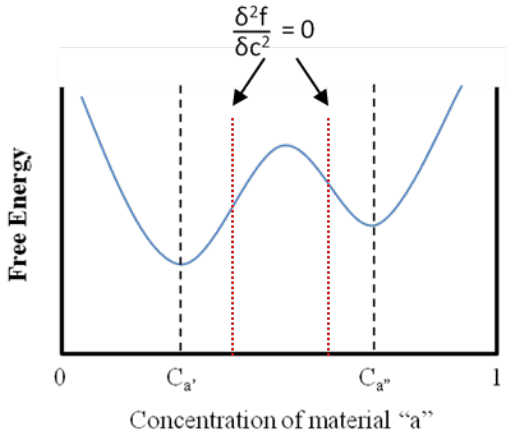

Figure 4.7: Qualitative plot of free energy as a function of composition. Regions between the red dotted lines are called the spinodes, where a homogenous composition is unstable. Systems in the spinodal region will decompose into two phases at concentrations C_a' and C_a".

ITO coated glass slides were prepared via RF magnetron sputtering. A 99.99% pure In_2O_3:Sn_2O_3 (90%:10%) was used to deposit 200 nm thick ITO films at 3 mT. In order to promote nanoparticle adhesion on the surface, the ITO films were subjected to various acids in order to lower the films' surface energy. It was found that aqua regia (HCl:HNO_3, 3:1) decreased the surface energy (increased hydrophobicity) without significantly increasing the surface roughness of the film. Efforts to investigate other acids either did not appreciably affect the surface energy (HCl, H_2SO_4) or aggressively damaged the ITO film rendering it useless for device applications (HNO_3, HF).

CdSe nanocrystals capped with trioctylphosphine oxide (TOPO) were washed in methanol. The nanoparticles were dispersed in toluene at concentrations of 20 mg/ml.

Etching studies determined that a 20:3:1 mixture of H_2O:HCl:HNO_3 for 30 minutes significantly increased the water contact angle of ITO films (figure 4.8). It was found the cleanliness of the glass substrates and quality of the sputtered ITO films greatly influenced the etching rates and final film quality. Without carefully prepared sputtered films, high surface areas susceptible to pitting and rapid etching were observed.

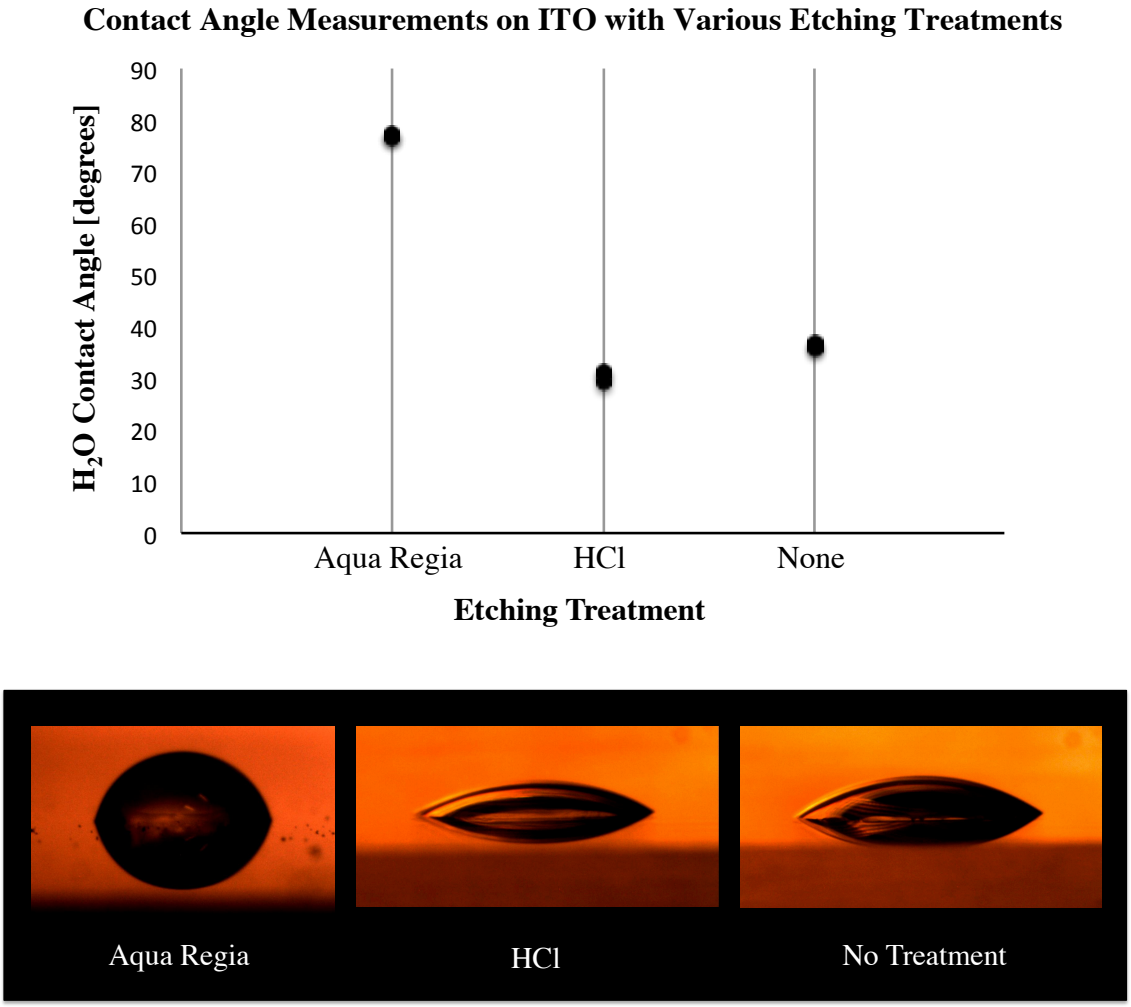

Figure 4.8: Water contact angle measurements on ITO films subjected to various acid treatments.

The water contact angle measurements were performed with a home built system using a front lit, high contrast background to achieve maximum resolution, depicted in figures 4.9 and 4.10. The photographs were converted to 8 bit black and white images and processed using imageJ, an open source, java based image processing algorithm developed by the NIH[77]. Furthermore a plugin to determine the accurate shape of the drops (and thus an accurate contact angle) was used. This plugin, also open source, was developed by Stadler and others at École Polytechnic.[78, 79]

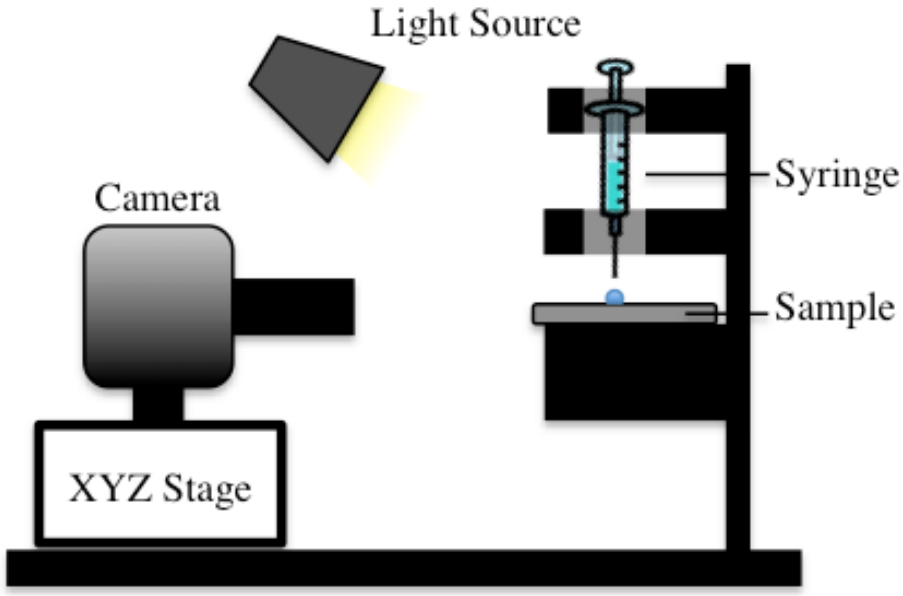

Figure 4.9: A diagram of the water contact angle measurement setup constructed for these experiments.

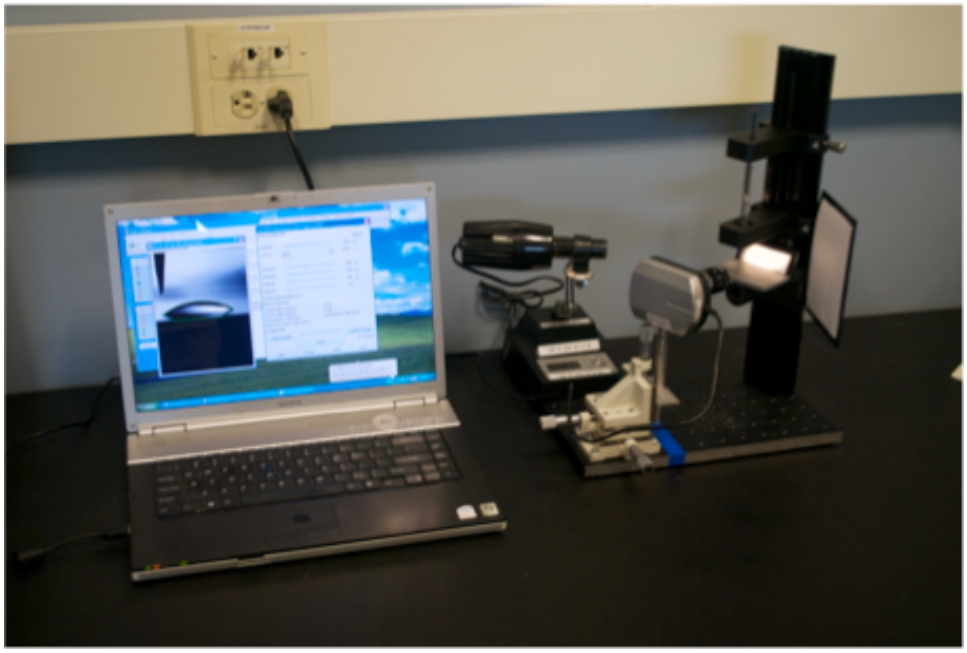

Figure 4.10: A photograph of the water contact angle measurement setup constructed for these experiments.

After optimizing the etching process, nanocrystal films were deposited using the Langmuir-Blodgett deposition method, nanocrystal films were deposited at surface pressures of 32 mN/m, just below their collapse pressures to achieve maximum film density (figure 4.11). Upon comparing the aqua regia treated substrates with the untreated substrates, it was found the untreated samples had phase segregated (as seen in prior studies) leaving a poorly covered ITO film. These patterns created by this phase segregation can be well described by the Cahn-Hilliard equation, modeled in figure 4.12.

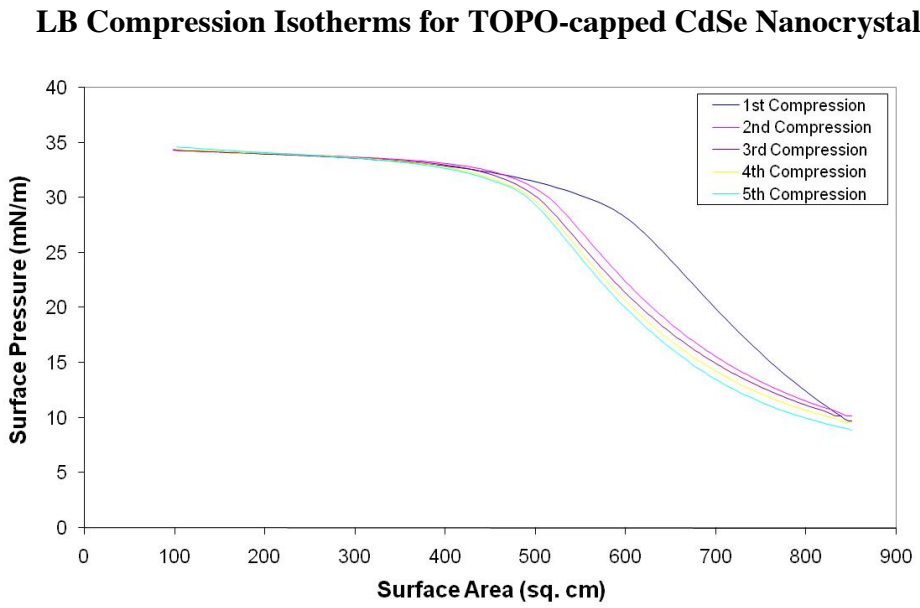

Figure 4.11: LB compression isotherms for deposited nanocrystal films. The films show stability at 32 mN/m, the pressure used for these depositions.

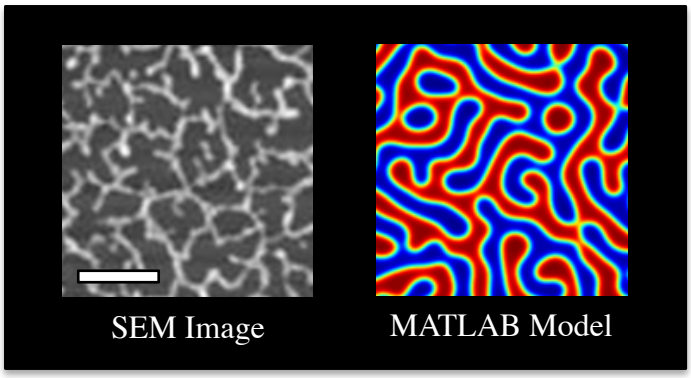

Figure 4.12: (left) Phase segregation observed in CdSe Langmuir films deposited on a hydrophilic substrate ($\theta = 36^{o}$), scale bar is 2 μm. (right) Spinodal decomposition modeled according to the Cahn-Hilliard equation in MATLAB.

Furthermore, the films deposited on the aqua regia treated samples exhibited higher transfer ratios during deposition and higher photoluminescence after. The transfer ratio is a measure of how much the surface area of the trough is decreased as the substrate is being dipped through the monolayer:

$$Transfer\ Ratio = \frac{Change\ in\ Trough\ Area\ During\ Deposition}{Total\ Surface\ Area\ of\ Substrate} \quad [4.4]$$

As the LB trough is programmed to hold the film at a constant pressure during deposition, complete substrate coverage would yield a transfer ratio of 1. Given that these substrates are only covered with ITO on one side and that the glass side is relatively hydrophilic, transfer ratios higher than 0.8 for the aqua regia treated samples were observed. Photoluminescence measurements were in agreement with the transfer ratio data, suggesting that the aqua regia treatment improved nanoparticle coverage on ITO films (figure 4.13).

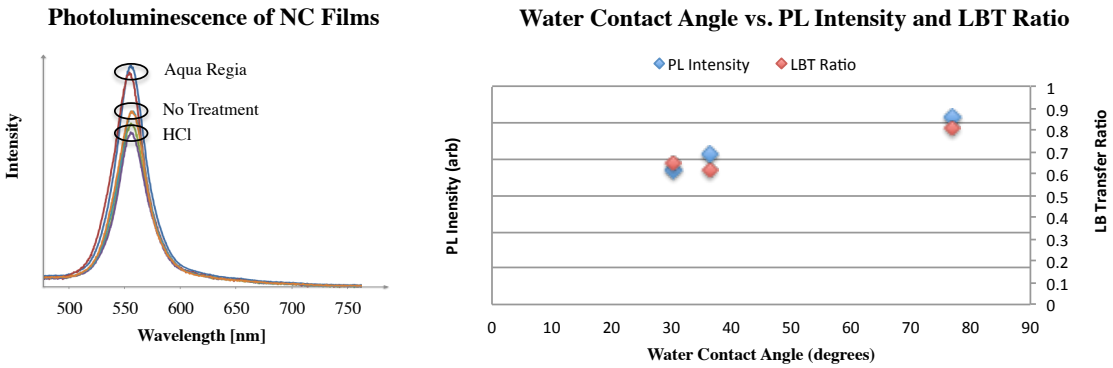

Figure 4.13: (left) Photoluminescence measurements taken of deposited nanocrystal films on treated ITO substrates. Higher PL signals indicate greater nanoparticle density on the ITO surface. (right) Measured water contact angle vs. PL intensities, illustrating the importance of low surface energy substrates when seeking high nanoparticle coverage.

While the increased coverage seen on the treated ITO films was encouraging, the nanocrystal film quality still needed to be improved in order to realize robust, vertically oriented devices. Even after dozens of monolayers were deposited on the substrates (the bottom contact in a device), it was found that deposition of a top contact shorted the device and horizontal structures were non-conductive, suggesting there were still voids in the nanocrystal films. SEM images of treated substrates verified an improvement in coverage but a persistent lack of large area film formation.

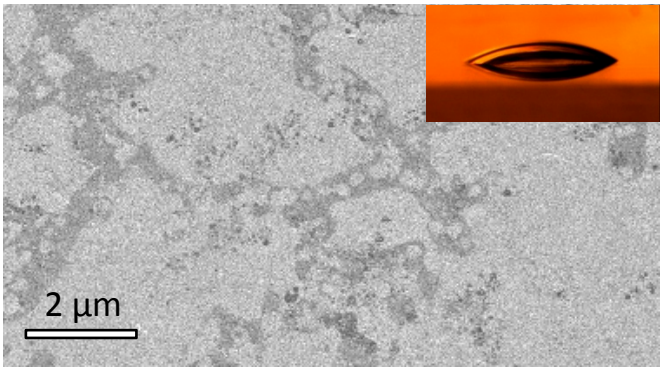

CdSe on ITO (no treatment)

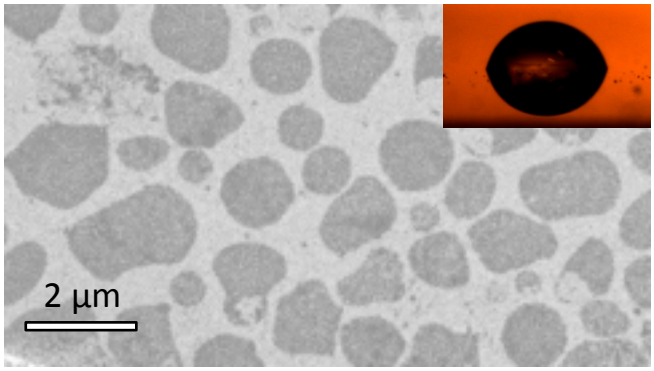

CdSe on ITO (aqua regia treatment)

Figure 4.14: SEM comparison of CdSe/ZnS-TOPO Nanocrystals deposited on treated (top) and untreated (bottom) ITO substrates.

4.4 Nanocrystal Purification: Rinsing of Spreading Solutions

Despite efforts at modifying experimental conditions and substrate surface chemistry, a larger area monolayer remained out of reach. Attention was refocused back to the initial spreading solutions.

4.4.1 Commercial Nanocrystals

While (purchased) stock solutions of TOPO-capped CdSe nanoparticles were purified from their initial reaction aliquot by the manufacturer, it was realized they contained a substantial excess of unbound TOPO ligand in solution (to enhance stability).

Drying experiments indicated that the reported concentrations of the stock solutions (in mg/ml) were actually the concentrations of total dissolved solids, not the concentration of CdSe nanocrystals as advertised. A two solvent method was followed to reduce unbound ligand in solution and characterize the solutions:

1. Add 10 ml methanol to 5 ml of stock CdSe-TOPO solution and mixed thoroughly. Solution becomes opaque, nanocrystals precipitate out after 30 min.
2. Remove 10 ml of the supernate and vacuum dry the precipitate.
4. Add 5 ml of toluene, dissolving the precipitate.
5. Filter resulting solution through a 0.22 μm syringe filter to remove aggregates or large impurities.
6. Repeat.

Table 4.1

Throughout this procedure the absorbance of the dispersed solutions was measured, Langmuir isotherms of the supernates were formed and the dried precipitates were weighed to determine the amount of TOPO removed. Only 10 ml (of the 15 ml total volume) of the solution in step 2 was removed to avoid accidental loss of precipitated nanocrystals. Later rinsing efforts employed centrifugation and a total decantation of the supernate, but these studies gave us valuable insight into the amount of excess ligand being removed. Figure 4.15 illustrates the mass of the sample after each of four consecutive rinse procedures.

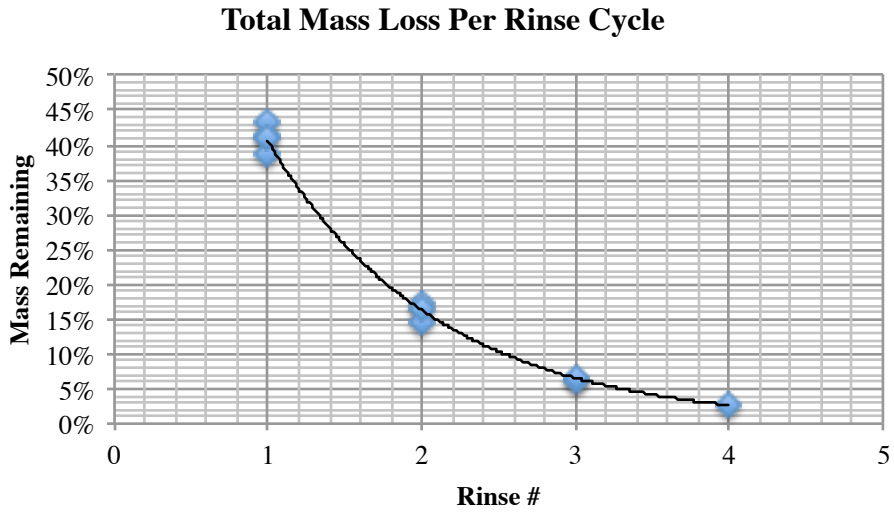

Figure 4.15: Percentage of original mass remaining after consecutive methanol rinsing cycles. Mass loss is due to removal of excess unbound TOPO ligand.

The extent of mass loss was surprising and the procedure was repeated several times. Plotting instead the relative mass loss per cycle it cab be seen that it is relatively constant for the first few rinsing cycles (figure 4.16). Furthermore, it was noted that this mass loss is consistent with the percent of solvent removed after precipitation. Efforts to remove more than 10 ml (of 15 ml total volume) resulted in significant loss of nanocrystal precipitate that was still partially suspended in the lower third of the solution. Dividing the percent mass loss by the percent volume decanted gives us the solvent utilization (figure 4.17) which represents the percentage of mass soluble in methanol. High values, such as those measured in figure 4.17 indicate that nearly the entire solution prior to rinse 1 and 2 was soluble in methanol. It was thus concluded that the commercially bought solutions were nearly completely (>99% by mass) TOPO.

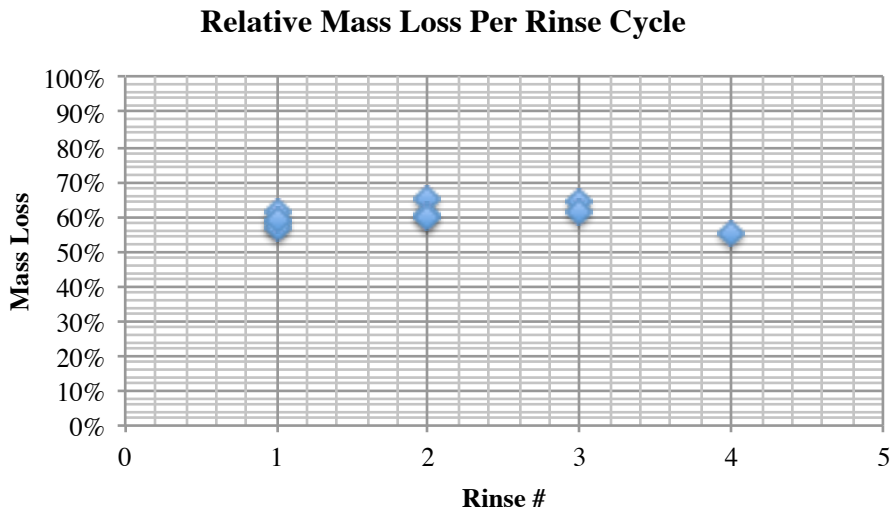

Figure 4.16: Percentage of mass loss per rinse cycle for consecutive methanol rinse. Mass loss is due to removal of excess unbound TOPO ligand.

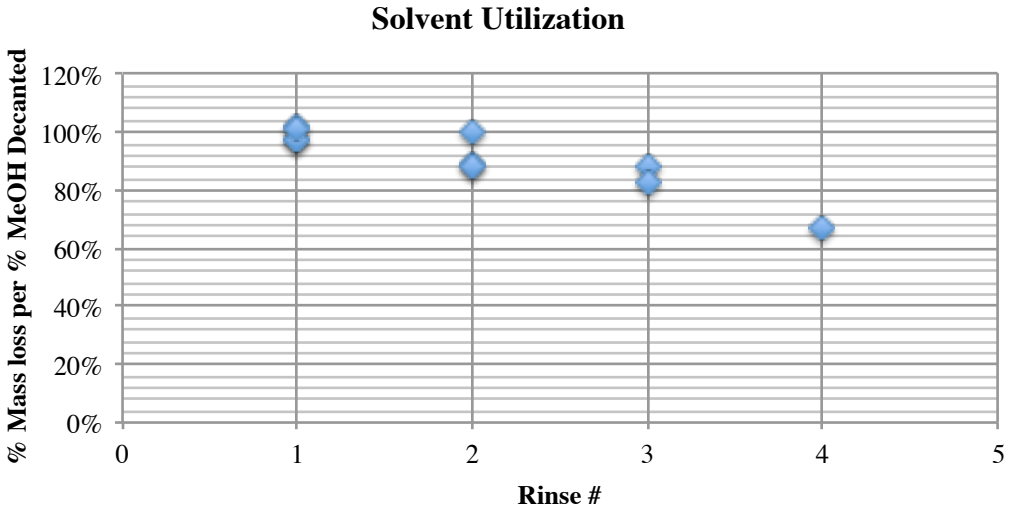

Figure 4.17: Solvent utilization for four consecutive methanol rinse cycles. These high values indicate the initial solution was comprised almost entirely of unbound TOPO.

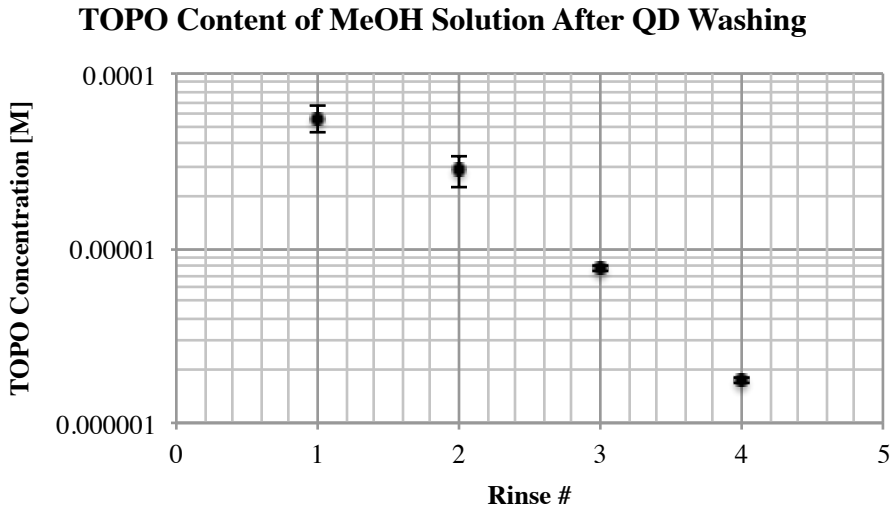

Figure 4.18: TOPO concentration of methanol supernate after consecutive rinsing steps (described in table 4.2).

This process resulted in rinsing solutions with successively decreasing TOPO concentrations (the supernate was analyzed in the Langmuir trough to determine molarity, shown in figure 4.19). Upon further rinsing (beyond 4 rinsing cycles) nanoparticle aggregation was observed (0.22 μm filtered solutions were optically clear with no measurable absorption).

4.4.2 Synthesized Nanocrystals

The difficulty in spectroscopic analysis of the proprietary nanocrystals motivated us pursue synthesis of nanocrystals to better characterize them and understand the components of the spreading solution. CdSe nanoparticles were synthesized by colleagues via a well established wet chemical method with TOPO, trioctylphosphine (TOP) and hexadecylamine (HDA) as coordinating ligands in an excess of TOPO.[80] The CdSe nanoparticles were kept in an extreme excess of unbound TOPO forming a greasy

solid stored in the dark at room temperature. TOPO has a low melting point (52° C) so gentle heating of this solid to 60° C melted it, producing a semi-transparent solution of TOPO capped CdSe nanocrytsals dispersed in liquid TOPO. The process used was slightly refined from the initial procedure (table 4.1) to include centrifugation, allowing us to completely precipitate the nanocrystals and decant all of the methanol solution during each rinse cycle. Furthermore, the vaccum-drying step for all but the final dispersion was eliminated.

1. Add 10 ml methanol to 5 ml of stock CdSe-TOPO solution and mix thoroughly. Solution becomes opaque immediately.
2. Centrifuge the suspension at 6500 rpm for 5 minutes and decant the colorless supernate.
3. Add 5 ml of toluene, dissolving the precipitate.
4. Repeat 1-3 for each desired rinse cycle.
5. Filter resulting solution through a 0.22 μm syringe filter to remove aggregates or large impurities.

Table 4.2

This rinsing procedure reduced TOPO concentrations in the nanocrystal solutions by a factor of nearly 200 (figure 4.20) but still proved insufficient to form stable monolayers of CdSe nanocrystals: too much free TOPO exists in solution to allow for NC monolayer formation. This is evident by the collapse pressures observed in rinsed films. Referring to the earlier discussion of mixed monolayers (figure 3.16, equation 3.23) it is evident that the isotherms that were observed were primarily TOPO for three reasons.

1. Absorption measurements allow us to determine the concentration and size of CdSe nanocrystals. As absorption is dependent on the size of the nanocrystal core, it is relatively insensitive to surface passivation of the nanocrystal surface by organic molecules.[81, 82] It should be noted that inorganic passivation of the CdSe core with a wider bandgap shell (ZnS, ZnSe, CdS) will show a slightly redshifted (~ 50 meV) absorption profile due to the reduced quantum confinement due to carriers tunneling into the shell,[83] but an organic passivation has no such effect. Therefore different rinsing solutions can be objectively compared with absorption spectroscopy to determine the concentrations of CdSe nanocrystals independent of the excess TOPO concentration.

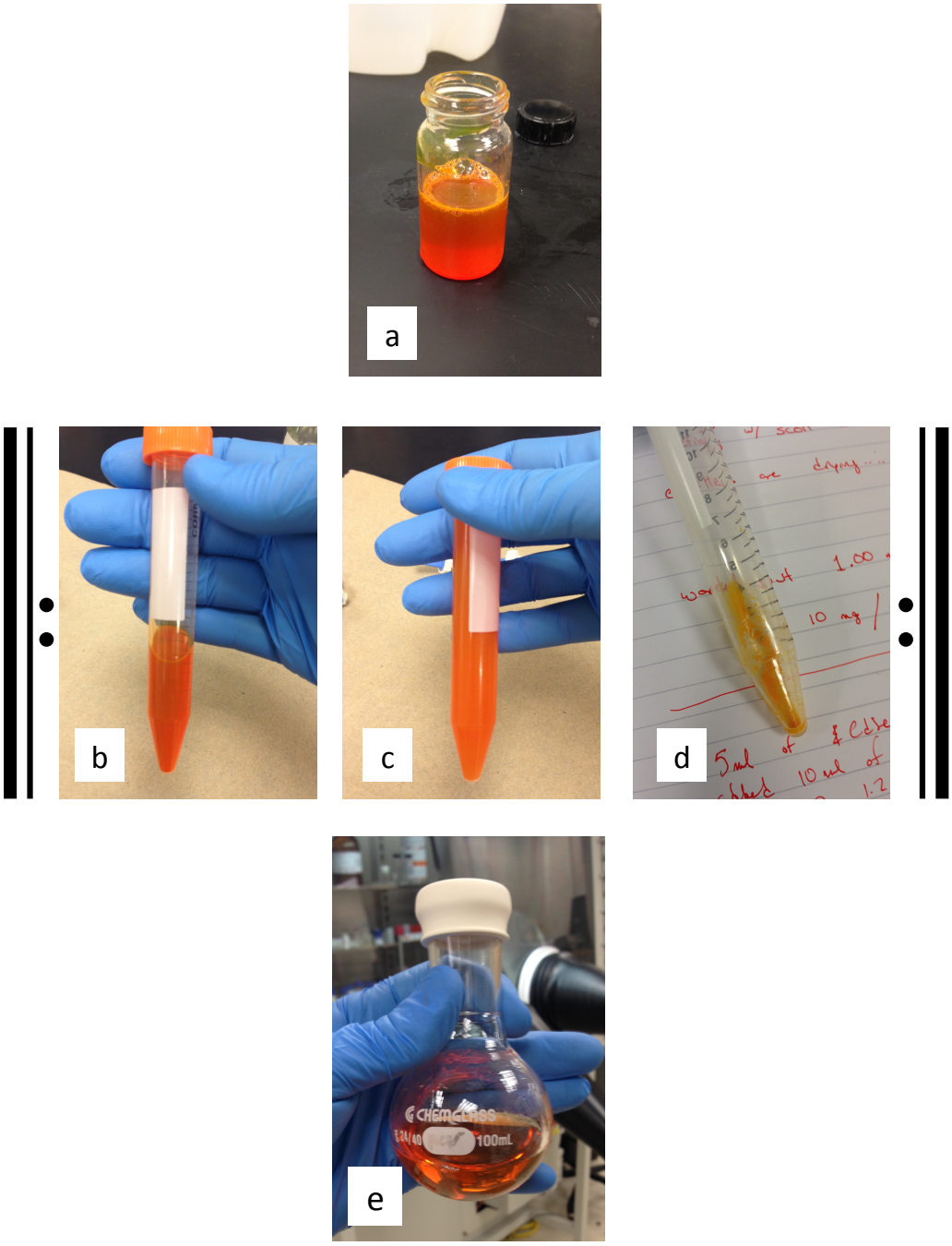

Figure 4.19: Rinsing process for UNCC grown CdSe nanocrystals. CdSe-TOPO stock solid is melted (a) and 10 ml methanol is added (c). The solution is centrifuged and the resulting (colorless supernate is discarded. For subsequent rinse cycles the precipitate is re-dispersed in toluene (b) and the methanol rinse (c,d) is repeated. After the final rinse cycle, the precipitate (d) is vacuum dried, dispersed in toluene and passed through a 0.22 μm filter before characterization (e).

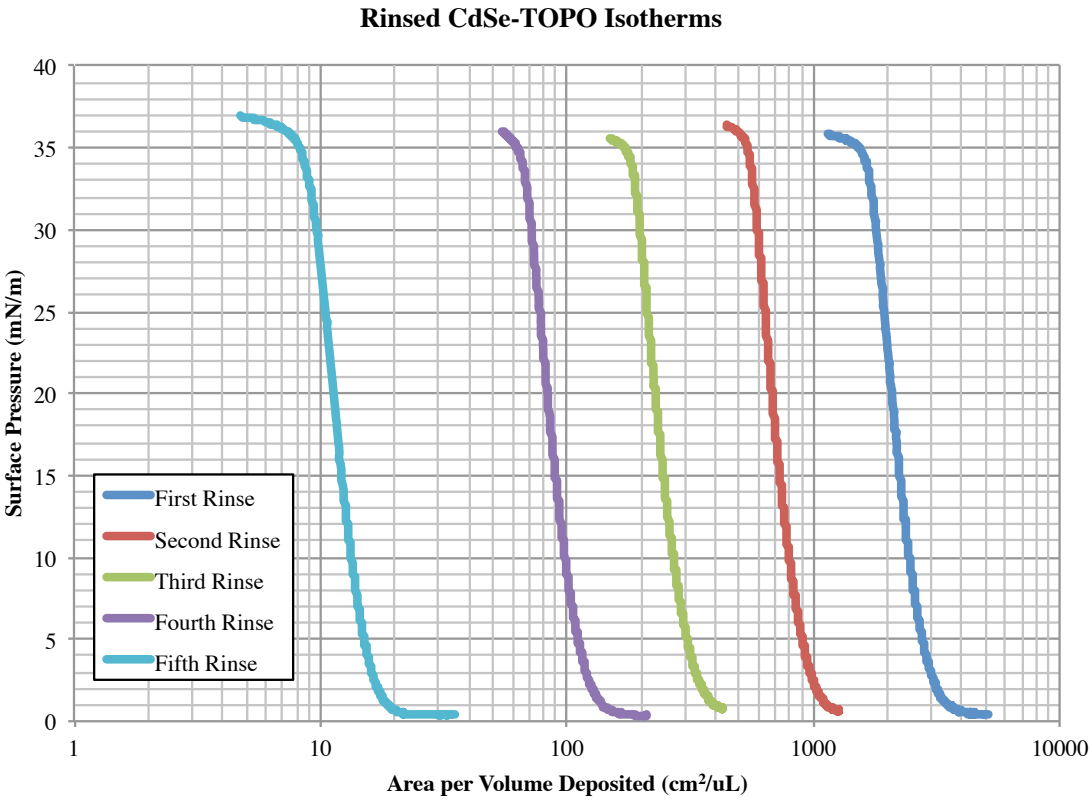

Figure 4.20: Isotherms of successively rinsed solutions of CdSe-TOPO in toluene. The x-axis represents the area occupied in the trough per µl deposited. Solutions with higher TOPO concentrations (i.e. the first and second rinses) obviously required

2. The collapse pressures of the films occur near 35 mN/m, consistent with a pure TOPO isotherm. Reports in the literature feature collapse pressures as high as 65 mN/m for CdSe films,[70] so it can be inferred that a film collapsing at 35 mN/m has little influence from the CdSe nanocrystals and thus comprised of nearly entirely TOPO.

3. The compressibility of the films (figure 4.21) is extremely similar to those of pure TOPO (figure 3.20).

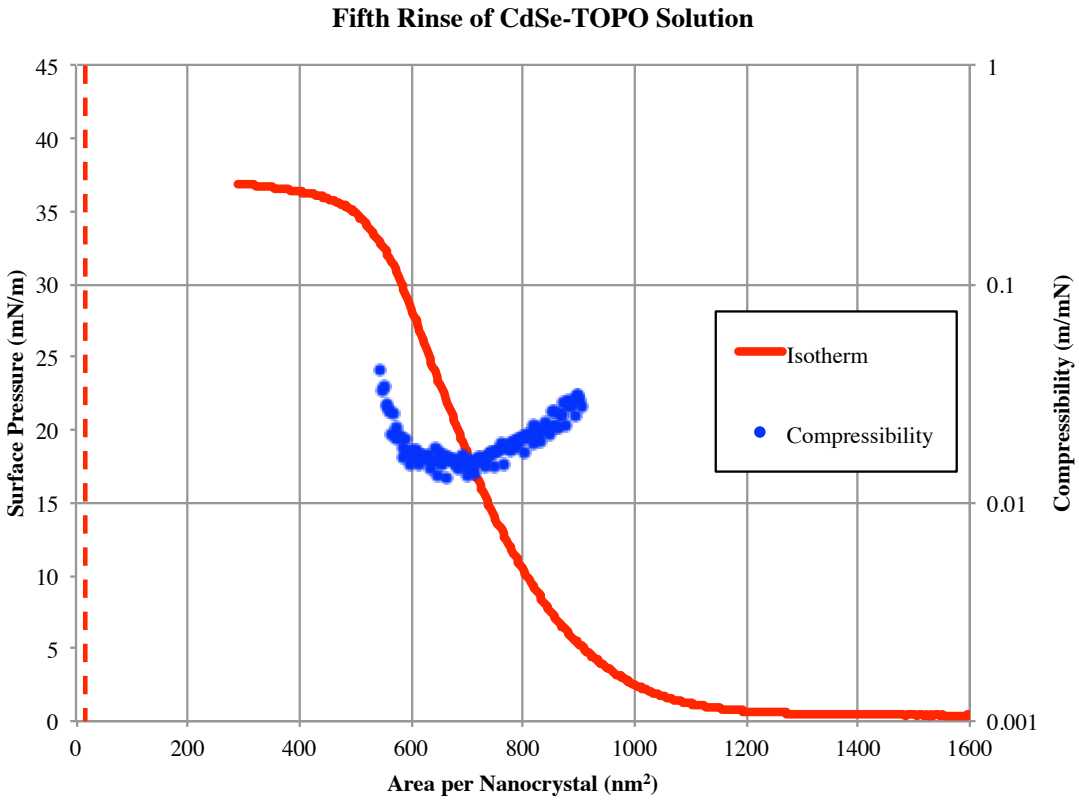

Figure 4.21: Isotherm and compressibility of the fifth rinse of the CdSe-TOPO solution. Dotted red line represents the predicted area per nanocrystal, 14.6 nm^2 per nanocrystal. Substantially higher measured nanocrystal areas suggest a significant excess of TOPO in the film.

While this data suggests that further rinsing is required to obtain a more pure nanocrystal spreading solution, it was found that further rinsing resulted in aggregation of the nanocrystals, evident from a lower optical density in the absorbance spectra (figure 4.22) and visible contamination of the 0.22 μm filter used to remove such aggregates (figure 4.23). Unused filters appear white, while filters used in rinse cycles 1-4 have a very slight

discoloration to them. Upon the fifth rinse it was immediately evident that significant amounts of nanocrystal aggregates were caught by the filter.

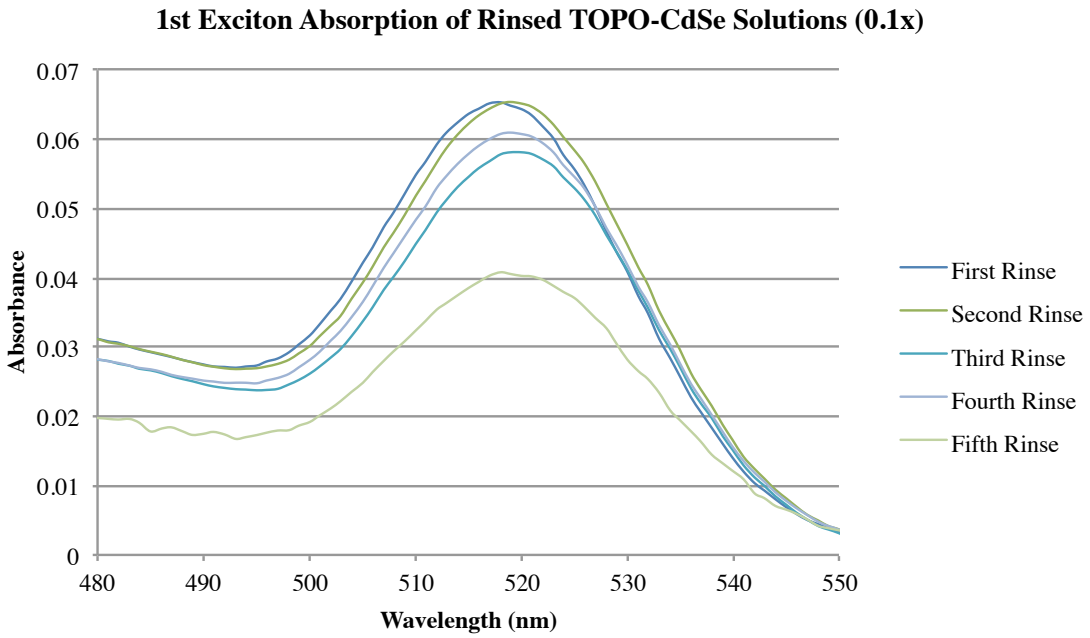

Figure 4.22: Absorption of rinsed TOPO-CdSe solutions showing a general trend of lower absorption with successive rinsing cycles, with a notable decrease after the fifth rinse. For this sample, subsequent rinses produced optically clear samples with no apparent nanocrystal absorption features.

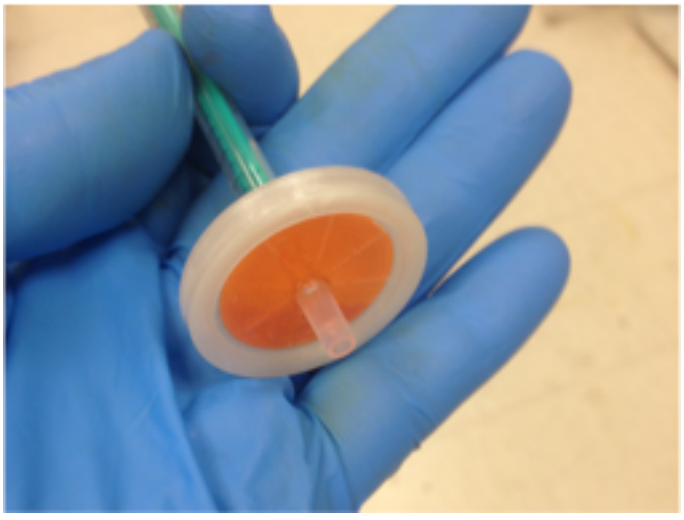

Figure 4.23: Visible evidence of nanocrystal aggregates trapped in a 0.22 μm filter after five rinse cycles.

Rinse #	TOPO molarity	NC molarity	NC molar %	NC mass %
1	266.7 mM	3.963 μM	0.001486 %	0.1725 %
2	85.51 mM	3.957 μM	0.004626 %	0.5350 %
3	28.65 mM	3.508 μM	0.01222 %	1.402 %
4	10.74 mM	3.689 μM	0.03425 %	3.831 %
5	1.455 mM	2.745 μM	0.1852 %	17.75 %

Table 4.3 shows the TOPO and CdSe nanocrystal content of each of the rinse cycles.

Further experiments all showed similar trends: after 5-6 rinse cycles significant amounts of nanocrystals were lost due to aggregation. It should be noted that in these experiments it was impossible to pursue more aggressive rinsing techniques without total loss of suspended nanocrystals.

CHAPTER 5: DEVICE FABRICATION

The original intent was to fabricate devices from monolayer and multilayer films of CdSe nanocrystals. Methods were developed and characterized for depositing indium tin oxide (sputter deposition), gold (sputter and electron beam deposition) and aluminum oxide (atomic layer deposition) in an effort to fabricate devices and test structures that would help better understand the properties of nanoparticle Langmuir films.

5.1 Sputter Deposition

Figures 5.1 illustrates a schematic of the AJA International ATC 1800F Sputter Deposition System (pictured in figure 5.2) used in these studies. Unlike many other deposition systems this is a sputter down setup: The substrate stage is oriented below the downward facing targets (the substrate stage facing up), allowing samples to be placed onto the stage without the need for clips or other retainment. The substrate stage is a 6" diameter rotating platform with a 300 ^{o}C programmable heater and water cooling. Three gas inlets are attached, two connected to (mass flow controlled) Ar and the other to a N_2 line for venting purposes. The roughing pump is connected behind the turbomolecular pump, which is connected to the deposition chamber via a gate valve. As the system does not have a load lock, the venting procedure is to shut down the turbo pump, close the gate valve and purge with N_2. After loading samples onto the substrate holder the access port is closed, the gate valve is opened and the turbo pump restarted. The pump is typically run for 90 – 120 minutes, which reduces the pressure in the chamber to 1.0 x 10^{-6} T.

Once this sufficiently low "base pressure" is achieved, one of the Ar valves is opened and Ar flows into the chamber at 15 sccm, increasing the pressure to 4.0 x 10^{-5} T. To further increase the Ar pressure the gate valve between the deposition chamber and turbo pump (the red component in figure 5.1) is partially closed until a pressure of 3.0 mT is achieved.

Upon achieving a background pressure of 3.0 mT an additional 15 sccm of Ar is introduced before turning on the RF (13.56 MHz) power supply at an initial power of 20 W, ramping up to 200 W over 60 s. The applied electric field produces an argon plasma with a characteristic light blue / lavender glow that brightly illuminates the inside of the chamber. As neutral Ar atoms are ionized, the Ar^+ ions are accelerated towards the target (figure 5.3) where one of several things may occur:

Table 5.1

1	The ion collides elastically and reflects off the target.
2	The ion collides inelastically and becomes buried in the target.
3	The ion collides with the target, incurring structural rearrangement.
4	The ion collides with the target leading to the ejection of target atom(s).

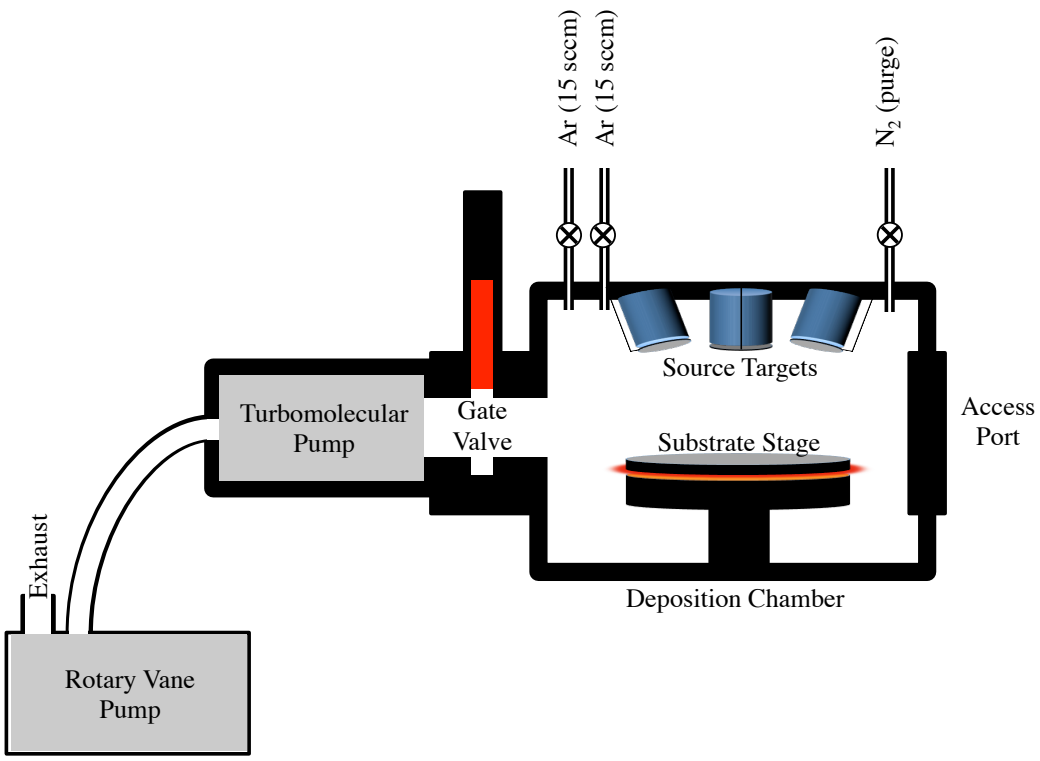

Figure 5.1: Diagram of the AJA International ATC 1800F Sputter Deposition System used to deposit thin films.

Sputtering occurs when a target atom is ejected from the target surface (table 5.1, #4), and travels through the chamber, either ballistically or colliding with other atoms before adsorbing onto the substrate or chamber wall. For sensitive samples ballistic transport is not desirable, introducing higher Ar background pressures increase the likelihood and number of collisions with gas molecules, decreasing the kinetic energy of the target atoms before they impact the substrate surface. Typically, the RF power, background (Ar) pressure and substrate temperature are varied to produce the desired conditions.

Figure 5.2: Picture of the AJA International ATC 1800F Sputter Deposition System.

5.1.1 Indium Tin Oxide Sputter Deposition

The first reported transparent, conductive material was cadmium oxide, published by Bedeker in the early twentieth century.[84] Since then, many other transparent conductive oxides have been explored,[85] namely tin doped indium oxide, more commonly referred to as indium tin oxide (ITO) due to the extremely high dopant concentrations. Indium tin oxide (ITO) is a degenerately doped n-type semiconductor commonly used in a wide range of applications, including displays, LEDs, sensors and shielding.

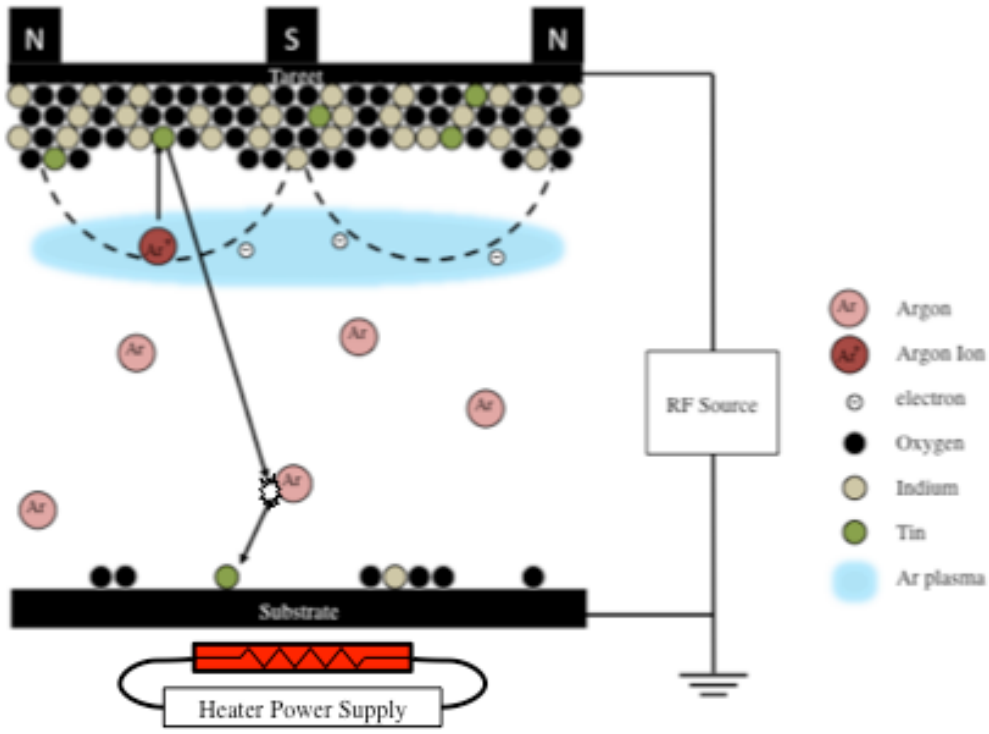

Figure 5.3: Illustration of an RF ITO sputtering process. Neutral argon atoms are ionized in a magnetically confined plasma, which then accelerate towards the target in the presence of the electric field. Collision with the target may eject target atoms, which then deposit on the substrate either ballistically or after several collisions within the low pressure Ar gas (one such collision is depicted in figure 5.3).

Many methods of ITO deposition exist, but hot pressed oxide sputtering targets have been shown to produce high quality films that are quite resilient to minor variations in process conditions,[86] and have such seen wide use in the optoelectronic industry. For these studies such targets were used, specifically In_2O_3/SnO_2 (90/10 wt%) 2.00" x 0.250" disks purchased from the Kurt J. Lesker Company.[87] Sputtered ITO films can have resistivity as low as 10^{-4} Ω cm and optical transmittivity as high as 85% in the visible region,[88] making them suitable for these studies. A notable feature of this sputtering

configuration is that the targets are composed of indium and tin oxides (as supposed to In/Sn alloys) and do not require an additional oxygen source (typically O_2 gas).

The deposition rate of the sputtering system was studied operating at a pressure of 3-4 mTorr and 200 W RF power. These values were chosed as the system was well characterized for operation in this regime, and ITO deposition had been shown successfully under similar conditions.[88] An average deposition rate of 5.9 nm/min was found under those conditions, producing uniform films that were conductive and optically transparent.

Film thicknesses were measured with Tencor Alphastep 200 profilometer. The step was created by masking off a section of the sample before sputtering. The substrates were single side polished sapphire. The Alphastep is a contact profilometer that measures step height by scanning a diamond tip across the sample with a uniform contact force. For hard films such as these (ITO on sapphire), this technique works extremely well. The tip has a radius of 12.5 μm, offering somewhat limited lateral resolution, but has a vertical resolution of in the nanometer range (when new, the manufacturer claimed a 5 Å vertical resolution, +/- 10 nm of noise was observed) that is sufficient for characterizing films 100-1000 nm in thickness. Select films were also measured with an AFM and it was found the Alphastep measurements to be in good agreement.

Sheet resistances were measured with a Lucas Labs Pro-4 Resistivity System. The setup is equipped with a four point probe head, a Keithley 2400 power source and Pro4 measurement software. The four point probe consists of four collinear tungsten wires spaced equally (figure 5.5). Current is passed through the outer probes (#1 and #4 in

figure 5.5) and measured by the inner probes (#2 and #3 in figure 5.5). Ideally the inner probes do not draw any current.

The resistivity of a semi-infinite volume is:

$$\rho_{SI} = 2\pi L \frac{V}{I} \qquad \text{[eq 5.1]}$$

Where ρ_o is the resistivity, L is the spacing in between the probes, and V and I are the current and voltage, respectively. Smits et al established that equation 5.1 was

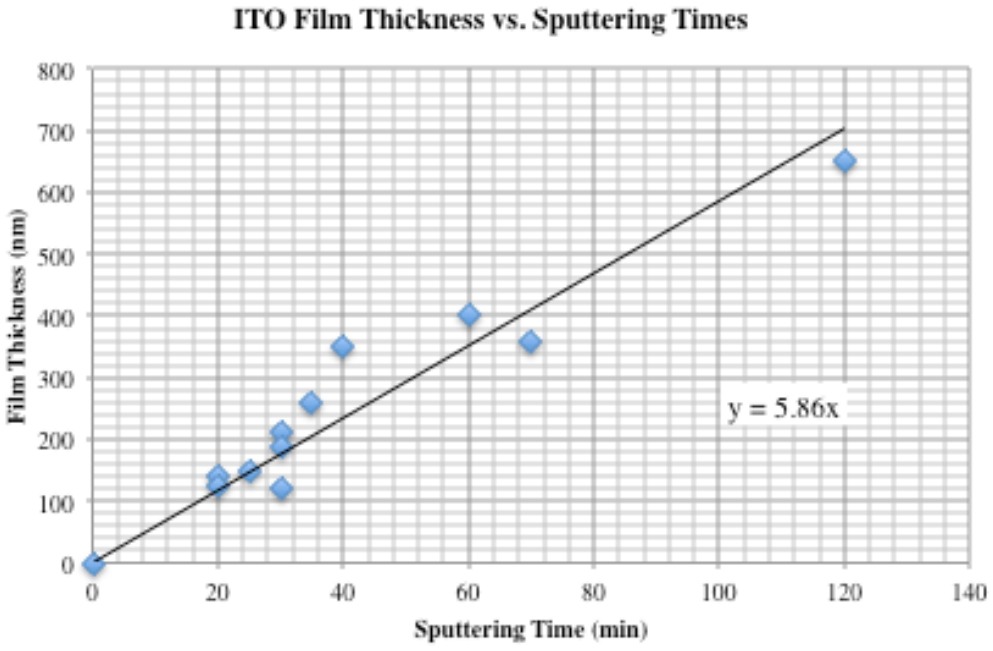

Figure 5.4: Sputtered film thickness vs. deposition time for ITO films deposited at 200 ºC, 2.5 W/cm^2 RF. The average deposition rate was 5.9 ± 1.3 nm/min.

valid for samples where the nearest boundary was at 5L from the nearest probe.[89] In this case L = 0.04", meaning samples thinner than 0.2" (5 mm) required a correction. This correction was found to be linear with respect to thickness provided the thickness of the sample was less than half the probe spacing (2t < L, in this case t < 2.5 mm), which was the case for all films measured. Furthermore the slope of this line was determined to be $2\ln(2)^{-1}$, allowing us to express a corrected, thickness dependent form of equation 5.1:

`

$$\rho_C = 2\pi L \frac{V}{I}\left(\frac{t}{L}\frac{1}{2\ln(2)}\right)$$

$$\rho_C = 4.53\, t\, \frac{V}{I} \qquad \text{[eq 5.2]}$$

Equation 5.2 is the corrected bulk resistance of the sample and has units of [Ω cm]. Dividing both sides of equation 5.2 by the sample thickness gives sheet resistance:

$$R_s = \frac{\rho}{t} = 4.53\frac{V}{I} \qquad \text{[eq 5.3]}$$

While the units of equation 5.3 are Ω, there is a geometrical significance to the measurement. Recalling the resistance formula:

$$R = \frac{l}{wt}\rho \qquad \text{[eq 5.4]}$$

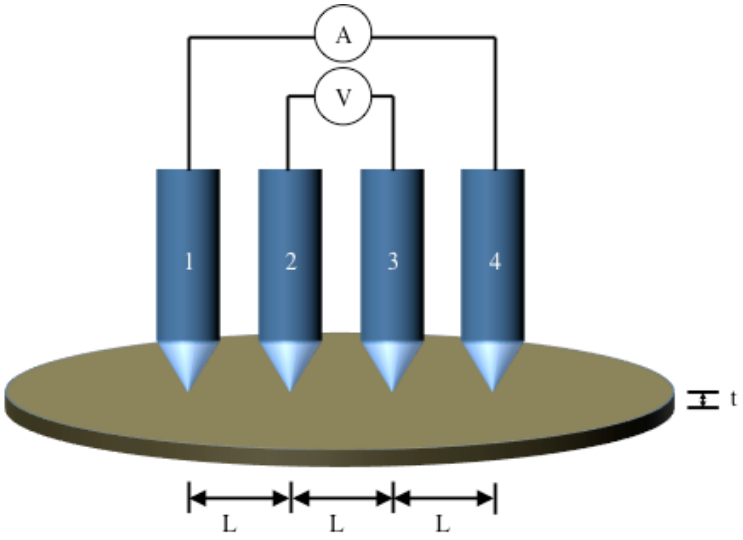

Figure 5.5: Diagram of a four point probe head used to measure sheet resistances.

Figure 5.6: Photograph of the four point probe measurement apparatus (Lucas Labs).

Where l, t, and w are the length, thickness and width of a sample, it can be seen that for a square (w = l) equation 5.4 becomes equation 5.3. From this equation 5.3 can be interpreted as the resistance of a square sample, which is why units for sheet resistance are commonly expressed as Ω/□. This is dimensionally identical to Ω but serves as helpful reminder of the geometric importance to sheet resistance measurements.

There is a further correction regarding the planar dimensions of thin films expressed as:

$$C = \frac{1}{1+\frac{9}{(D/L)^2}} \qquad \text{[eq 5.5]}$$

Where D is the diameter of the wafer. This probe station (and most others) are designed with closely spaced probes such that this correction approaches unity and can be disregarded in calculations. The samples measured were 50 mm in diameter, yielding a correction factor of 0.9964. Figure 5.6 is a photograph of the Pro4 apparatus used in these studies. Figures 5.7 and 5.8 show the measured sheet resistivity and calculated bulk resistivity, respectively, from the sputtered ITO films.

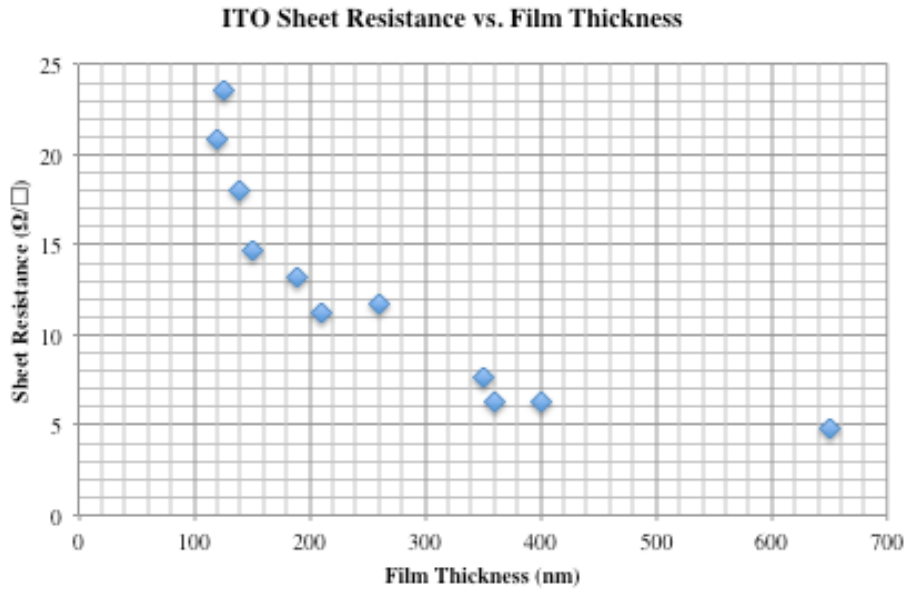

Figure 5.7: Measured sheet resistances for ITO films deposited at 200 ºC, 2.5 W/cm^2 RF. Sheet resistances were measured with a four point probe, film thicknesses were measured with a profilometer.

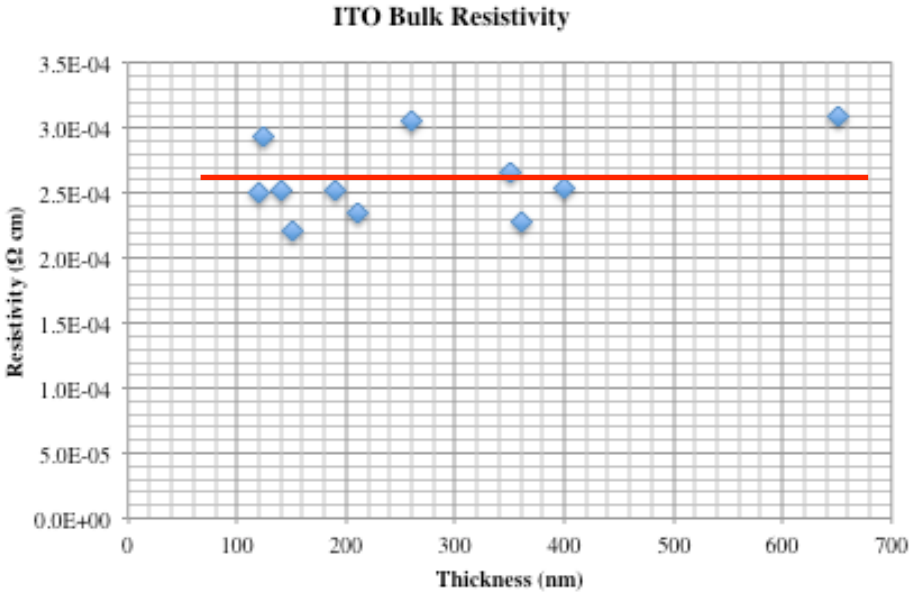

Figure 5.8: Calculated bulk resistivity for ITO films deposited at 200 ºC, 200 W RF. The average bulk resistivity was 26.1 ± 3.0 mΩ cm.

5.1.2 Gold Sputter Deposition

The procedure for sputtering gold is similar to that for sputtering ITO with one important difference. Instead of an alternating RF power source, the sputtering is carried out with a DC bias (sometimes known as diode sputtering). The target is held at a negative voltage while the substrate is either biased positively or earthed (as in this case). The procedure for striking an Ar plasma is identical to that for the RF ITO process, with an excess of Ar being introduced (30 sccm) before the pressure is adjusted to 3 mTorr and deposition proceeds. A schematic of the gold deposition process is shown in figure 5.9.

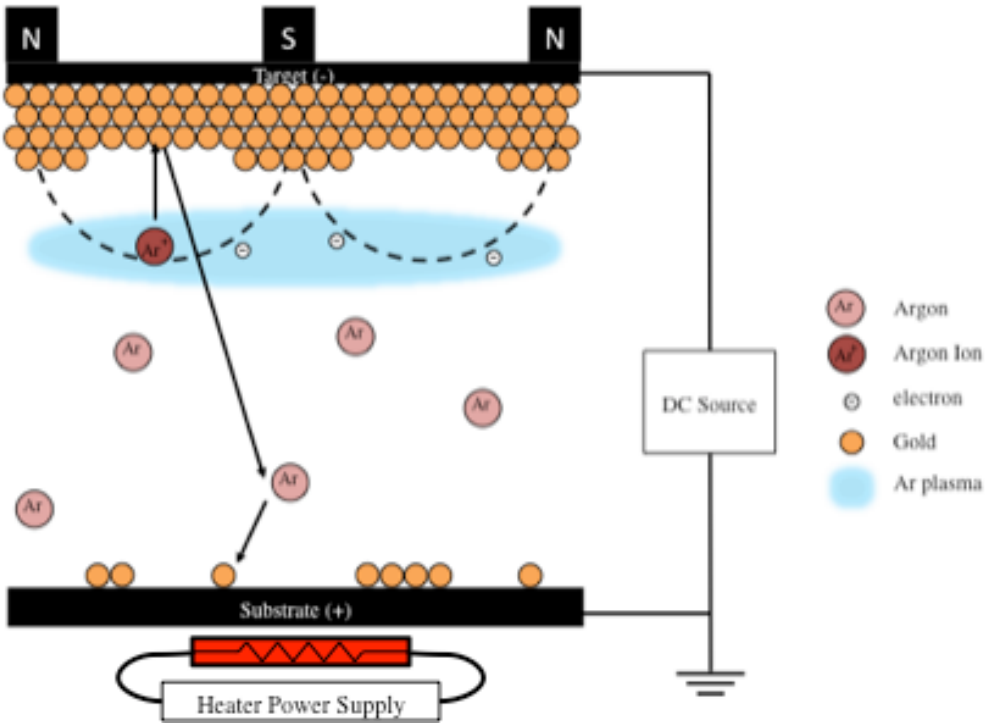

Figure 5.9: Illustration of an DC sputtering process. Neutral argon atoms are ionized in a magnetically confined plasma, then accelerated towards the target, ejecting target atoms which impact the substrate.

The gold films were characterized with both the Alphastep profilometer and a Veeco Dimension 3100 scanning probe microscope with a Nanoscope IV controller. Films thinner than 100 nm were measured with the AFM in tapping mode while films with thicknesses greater than 100 nm were measured with the Alphastep. The substrates were not heated during deposition and a deposition rate of 5.3 nm/min was observed at a 20 W DC power.

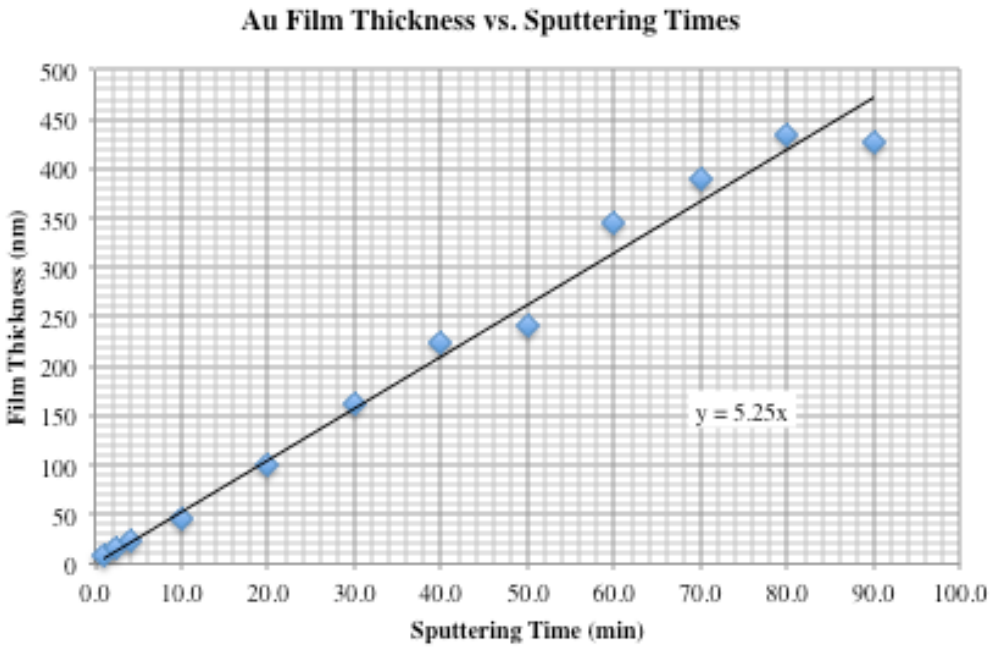

Figure 5.10: Sputtered film thickness vs. deposition time for Au films deposited at room temperature, 20 W DC. The average deposition rate was 5.25 ± 0.9 nm/min.

The gold films demonstrated sheet and bulk resistivity consistent with prior reports in the literature[90] and had a smaller deviation that their ITO counterparts (figures 5.11, 5.12).

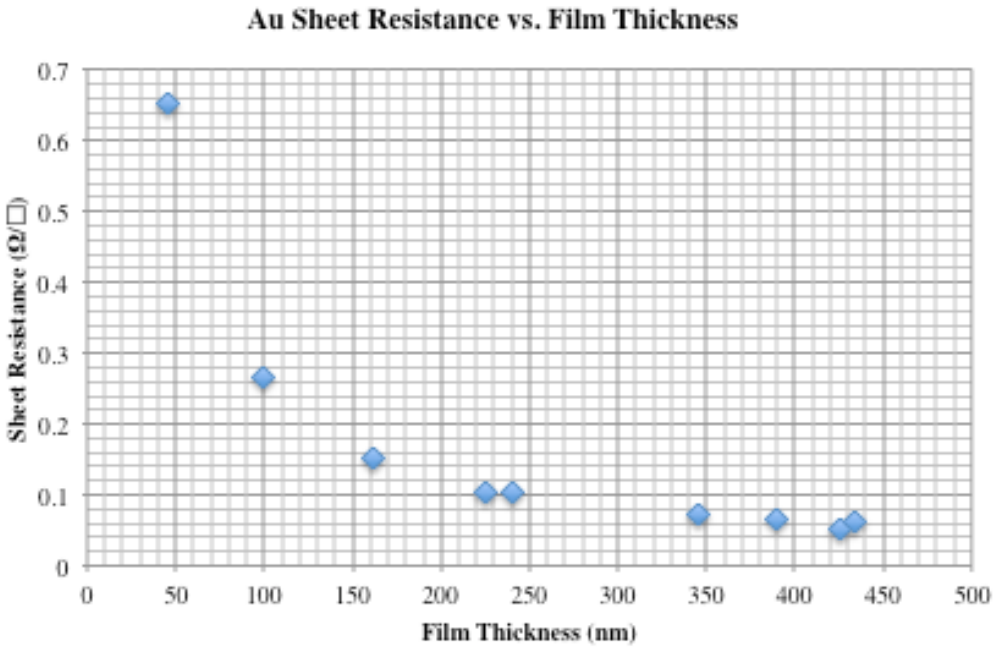

Figure 5.11: Measured sheet resistances for Au films deposited at 20 W DC. Sheet resistances were measured with a four-point probe, film thicknesses were measured with a profilometer and atomic force microscope.

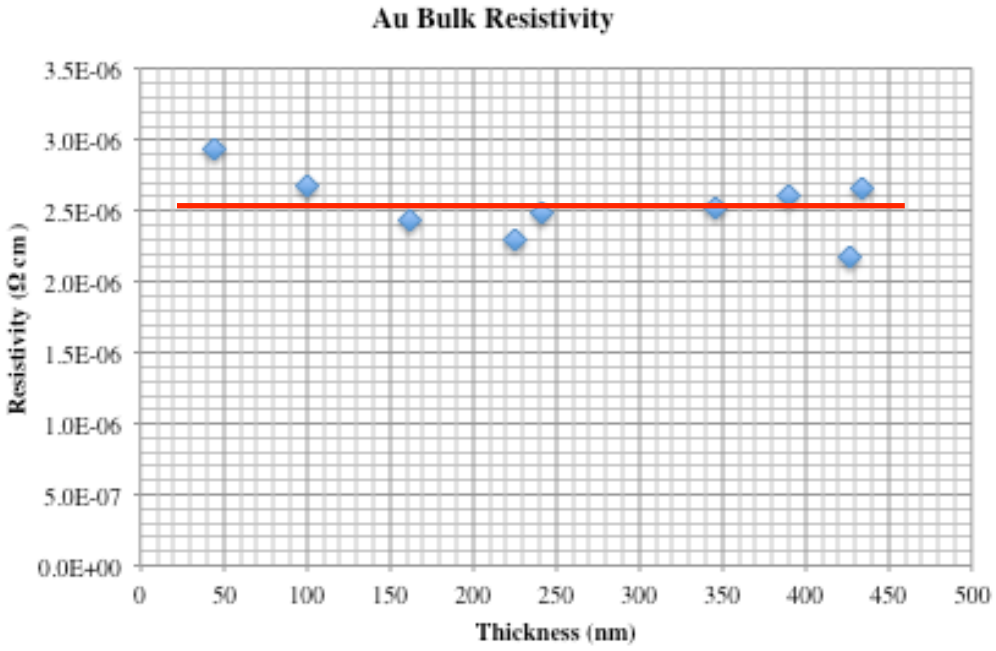

Figure 5.12: Calculated bulk resistivity for Au films deposited at 20 W DC. The average bulk resistivity was 2.53 ± 0.2 μΩ cm.

5.2 Electron Beam Deposition

A Kurt J Lesker PVD 75 Thin Film Deposition System was employed to deposit thin films of gold and chromium. It was found that patterning (and even handling) the gold films deposited via sputtering was difficult due to the poor adhesion between the gold film and underlying substrate. Using a thin layer of chromium (5 nm) followed by a thicker layer of gold (20-50 nm) fabrication and patterning gold films was possible with features as small as 1 μm.[91]

Electron beam deposition is a physical vapor deposition process that uses an energized tungsten filament to emit a beam of electrons to heat (and evaporate) a material (figure 5.13).

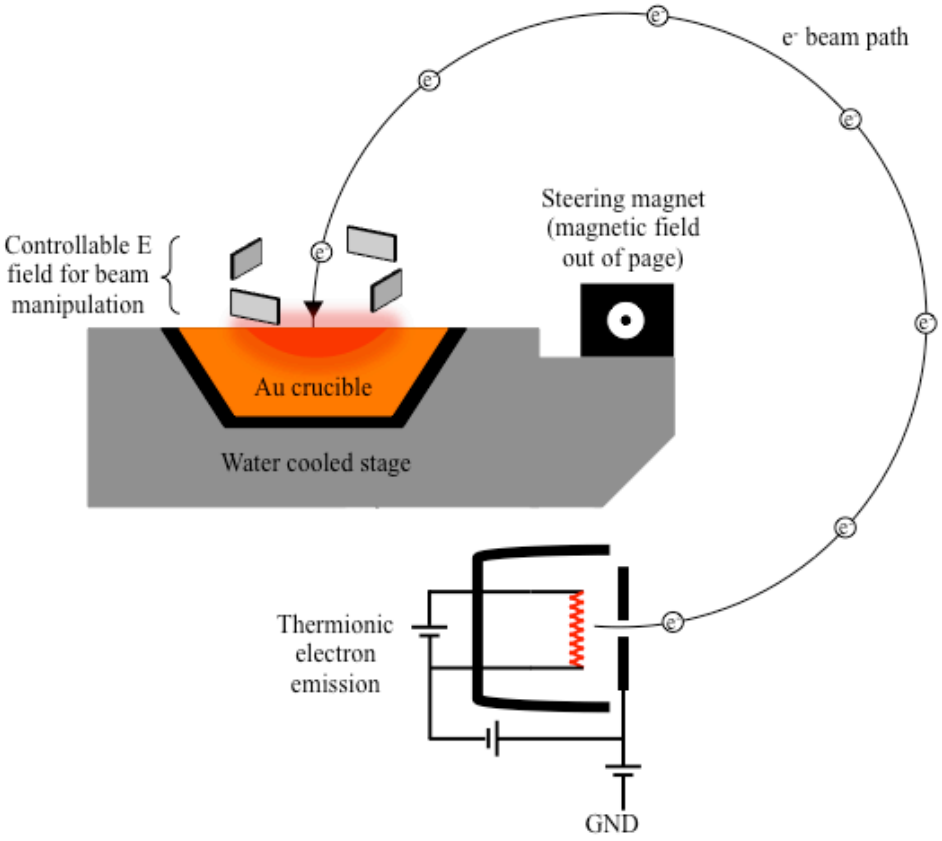

Figure 5.13: Diagram of an electron beam evaporation process.

When the tungsten wire is resistively heated to the point where the thermal energy of the electrons exceeds the work function, thermionic emission of electrons of occurs. An orthogonal magnetic field directs the emitted electrons in a circular path towards a molybdenum crucible on a water cooled stage. The crucible can be filled with a variety of metals, Au was primarily used for these device studies. Furthermore, a controllable electric field is used to direct the beam location within the crucible (the beam itself is much smaller than the crucible) to prevent non-uniform heating.

Figure 5.14: The Kurt J. Lesker PVD 75 Thin Film Deposition System.

5.3 Photolithography

Both ITO and gold structures were patterned for the purpose of measuring lateral conductance in these CdSe films. Two photolithographic techniques were employed to accomplish this, the first using the "lift off" method, where the photoresist is deposited and patterned prior to conductive film deposition and the second using the "etch back" method, where the photoresist is deposited and patterned after the conductive film has been deposited. The resist used is Shipley 1813, a novolac / diazonaphthoquinone (DNQ) based resist developed and sold by Microposit. The resist is positive, with DNQ in the exposed regions undergoing a photo-induced Wolff rearrangement, yielding a carboxyl group which renders such regions highly soluble in aqueous bases (figure 5.15).[92]

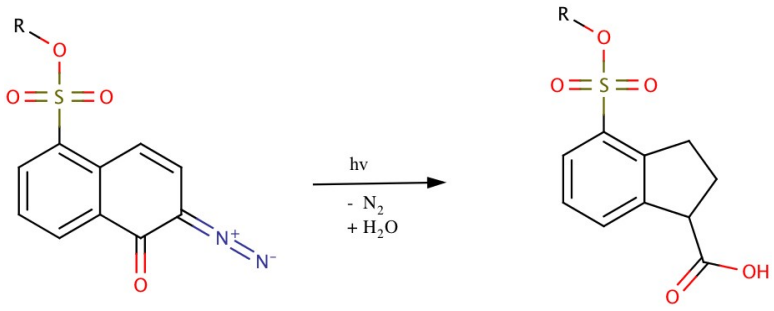

Figure 5.15: Wolff rearrangement of DNQ, producing a carboxylic acid that is soluble in an aqueous base.

5.3.1 Lift-off Photolithography

Lift off photolithography involves a patterned photoresist layer, which a film is deposited (sputtered or evaporated) on. Stripping of the photoresist layer removes both the photoresist and the portion of the film on top of that resist, while leaving behind the portion of the film directly on the substrate (figure 5.16). While this is commonly accomplished using a positive mask and a negative resist, this was approached this using a negative mask and positive photoresist, as a high quality Cr negative mask had already fabricated from previous work.

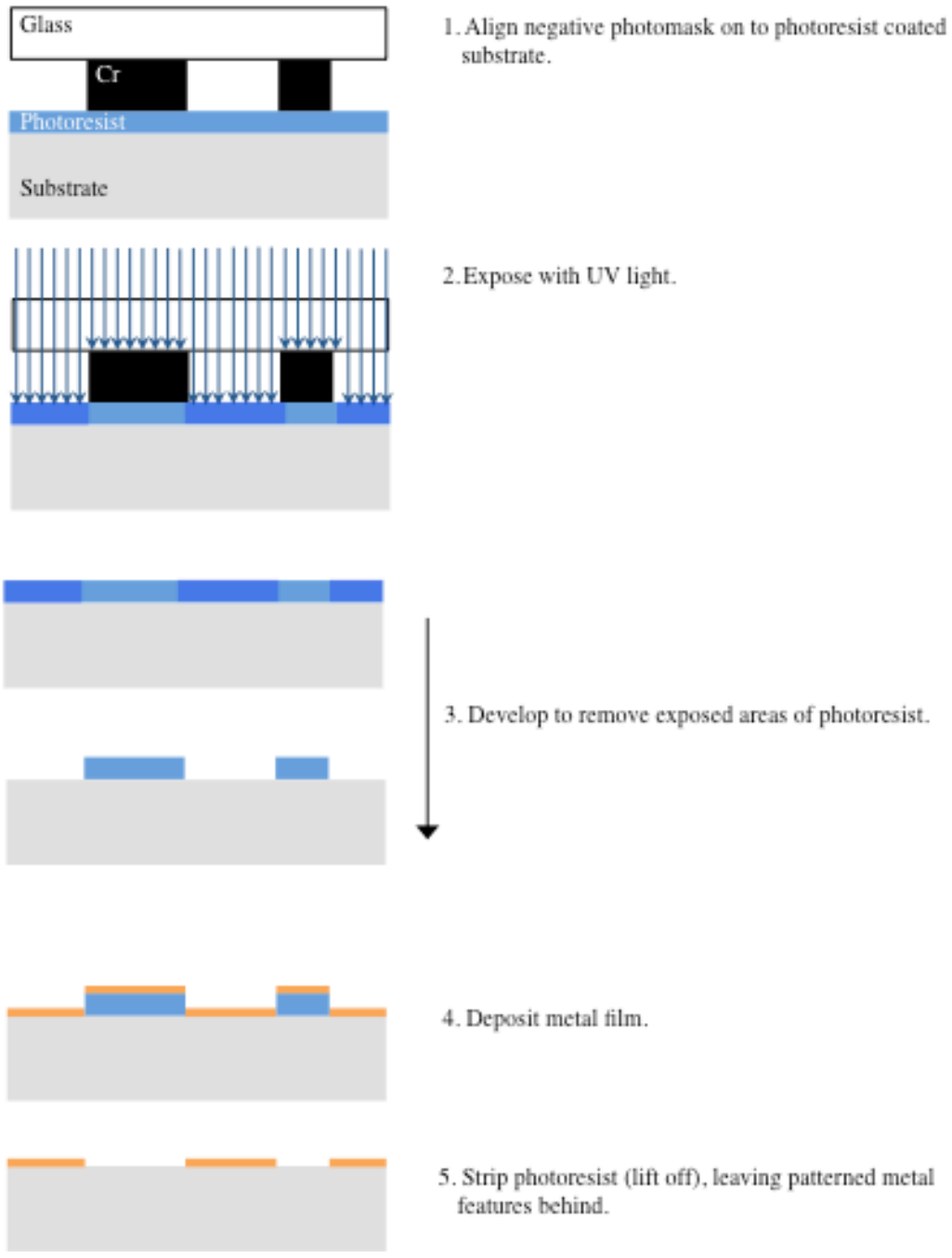

Figure 5.16: Photolithography process for lift off patterning of gold using Shipley 1813 positive photoresist and positive contact mask.

Furthermore, the fabrication of high quality patterns and structures using Shipley 1813, a positive Novolac based photoresist, had been successfully demonstrated before by this research group. Figure 5.16 illustrates this process. Prior to coating with photoresist the substrate is cleaned in a sonicated bath of acetone for 5 minutes, followed by 5 minute baths in methanol and then isopropanol before being blown dry with N_2. The sample is then baked at 110 ^oC to remove any water or other volatile components before being spin coated with hexamethyldisilazane (HMDS), an organosilicon compound used to promote adhesion between the oxide (or nitride) substrates and novolac based photoresists. HMDS is spun on at 4000 rpm for 40s, which functionalizes the surface with trimethylsilyl groups.[93] The wafer is now ready to be spin-coated with photoresist, which is done at 4000 rpm for 40 s. It is important to immediately soft-bake the spun on resist at 100 ^oC for 60 s to cure the film, and then to allow cured film to rehydrate for 60 s before UV exposure. This process yields a film approximately 1.3 μm thick, with minimal edge beading. Experiments with removing the edge bead (this is accomplished by exposing and developing the outer 5 mm of the circular wafer) in order to decrease the distance between the photomask surface and the wafer to be patterned, were not performed as it was found to be unnecessary. The sample is then placed in a Quintel Ultraline Q 4000-6 mask, aligner where a negative photomask is used to expose the sample in contact mode (figure 5.16). The mask has circular transmission line measurement structures patterned (see figure 5.17, note the lift off technique uses the negative mask, the positive mask is depicted in 5.17) a well-established method that allows for sheet resistance measurements of thin films.[94] Shipley 1813 is optimized for a 436 nm exposure, coinciding with the G-line emission (435.8 nm) of a mercury vapor lamp. Such a lamp (300 W) is fixed on the

Quintel mask aligner and samples are exposed to 150 mJ/cm^2 as recommended by the manufacturer.[95] Exposure doses are verified by measuring the lamps output prior to loading the sample and adjusting the exposure time accordingly. After exposure the samples are removed and developed in Microposit MF-351, a sodium hydroxide based (aqueous, 2.2 % wt) solution, to remove the irradiated portions of the film. The photoresist is rinsed thoroughly with water and dried with N_2 before chromium/gold deposition. This results in a metal film deposited directly on the substrate in areas where the sample was exposed and a metal film on top of a photoresist layer in unexposed areas (figure 5.16, step 4). By submerging the sample in an ultrasonicated bath of N-methyl-2-pyrrolidone (NMP), the remaining resist (and metal deposited on those areas) was completely removed, leaving behind a patterned metal film that is an inverse image of the initial (negative) mask used.

This technique worked very well for gold and other metallic films but was ineffective with films of ITO. The ITO films tended to flake off in larger pieces (10-100 μm in size) as the lacked the ductility to tear along adhesion lines as the gold films did. Furthermore, the ITO films also required longer times in the ultrasonicated NMP bath, suggesting that solvent penetration of the ITO films was poorer than it was with the gold. For this reason all further ITO patterning was done with etching.

5.3.2 Etch back photolithography

Etch back photolithography involves the deposition of a film (in this case, ITO), then overcoating with a film of photoresist. This is then patterned before the etching step, which removes the areas of ITO unprotected by photoresist. This was accomplished this using a positive mask and positive photoresist (Shipley 1813). Figure 5.17 outlines this

process, with the coating, exposure, and development conditions remaining the same as they were for the lift off procedure. The wafer was then immersed in a 1:1 $HCl:H_2O$ solution at room temperature for approximately 5 minutes depending on the thickness of the film. The measured etch rates were between 75-100 nm/min, the conductivity of etched areas was measured intermittently to determine etch progress, etching was considered complete when the substrates (sapphire or glass) measured zero conductivity. It is important to note that this wet etching method is isotropic, undercutting the film, thus effectively widening the gap from the original mask dimensions (illustrated in figure 5.18). The etching process carefully monitored so as not to over etch and furthermore the patterns were characterized after resist removal to verify the dimensions of these test structures.

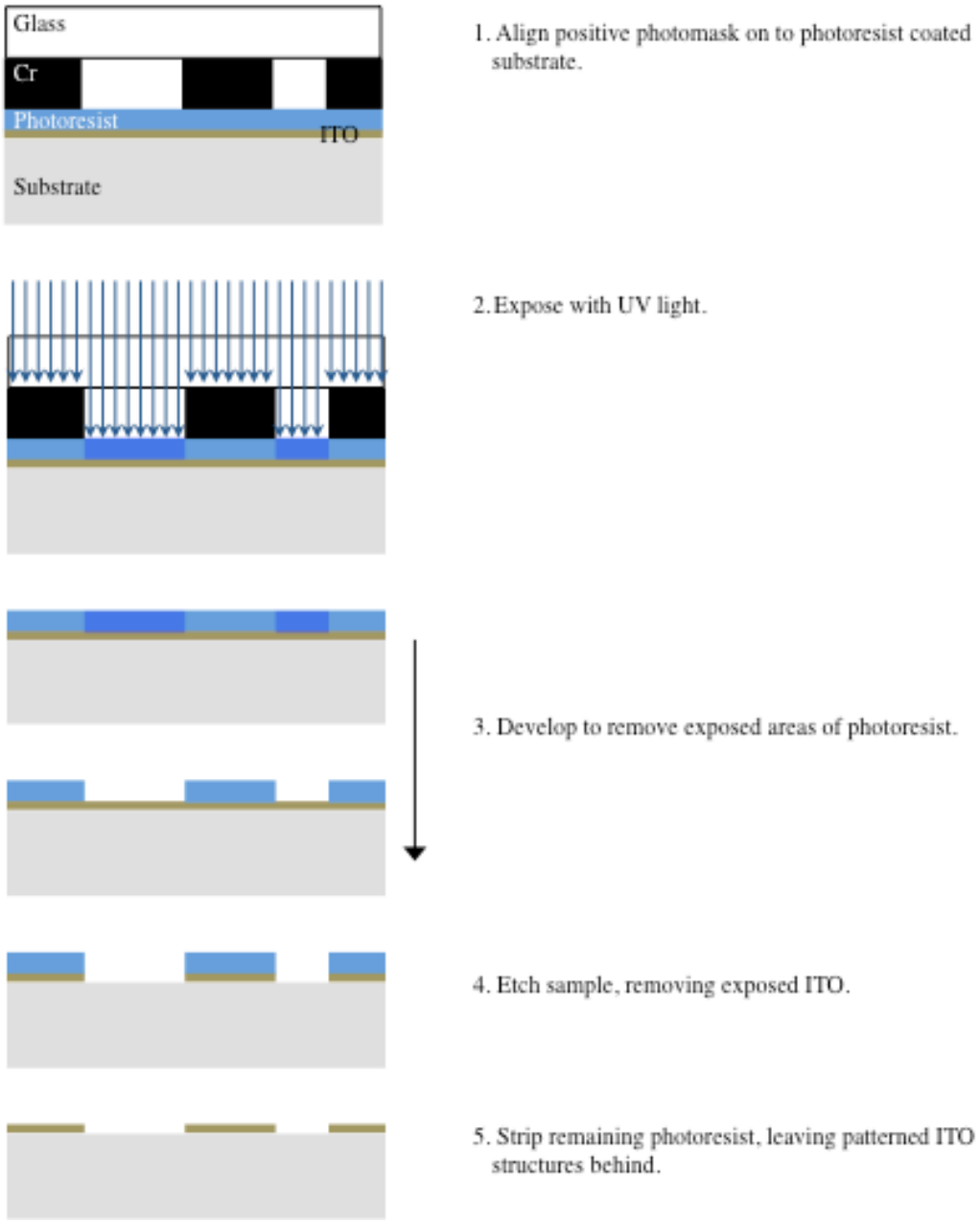

Figure 5.17: Photolithography process for etch patterning of ITO using Shipley 1813 positive photoresist and positive contact mask.

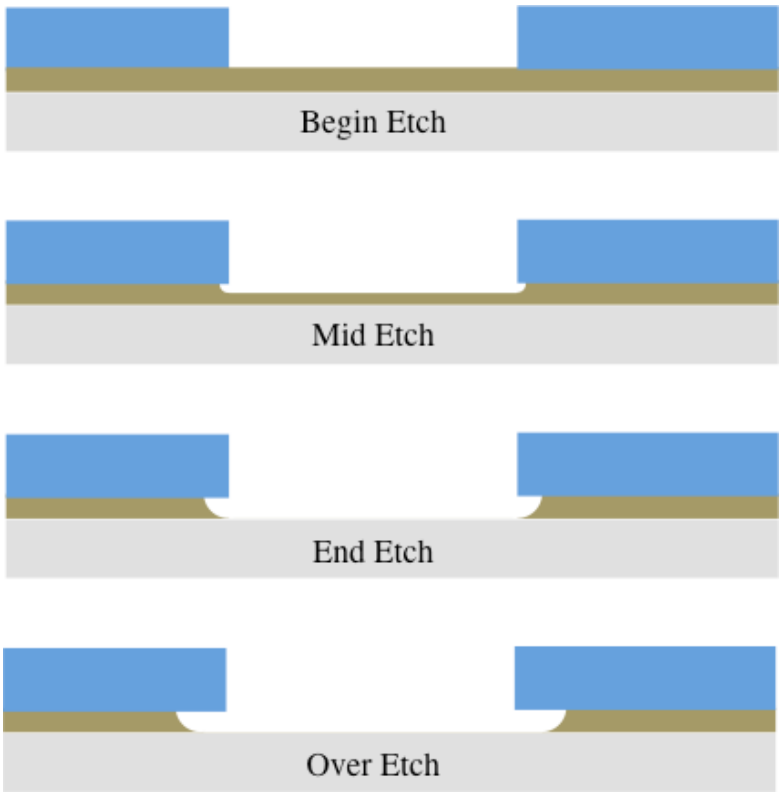

Figure 5.18: Illustration of isotropic wet etching and undercutting of the resist. Blue areas represent photoresist, brown areas represent ITO film and gray area is the substrate.

5.4 Circular Transmission Line Method Structures

The structures fabricated were circular transmission line method structures (CTLMs), whose dimensions are shown in figure 5.19. The respective gap spacings are 5, 10 15, 25, 35, and 45 μm. A two point probe method was used, applying a current across the inner and outer sections of the structure, and calculated a voltage using equation 5.6:[96]

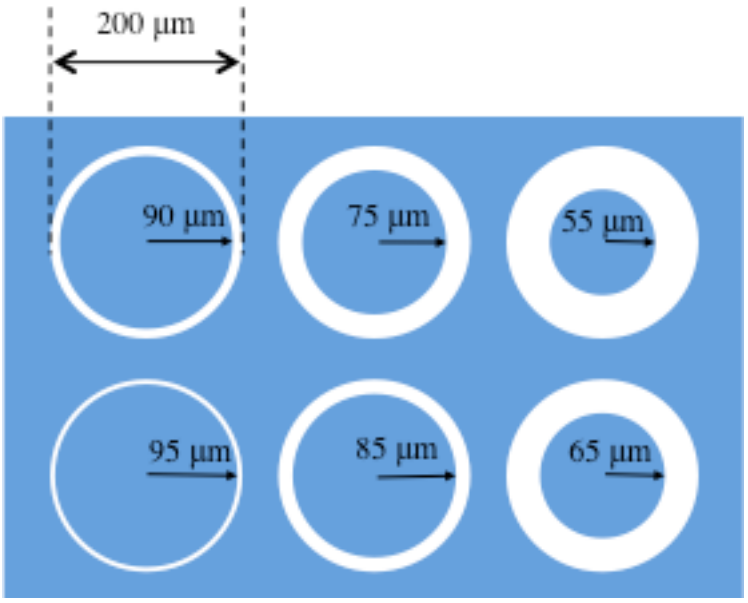

Figure 5.19: Positive contact mask pattern for circular transmission line method structures. The blue areas represent the opaque portion of the mask while the white areas will be exposed and eventually etched.

$$\Delta V = \frac{iR_s}{2\pi}\left[ln\left(\frac{r_o}{r_i}\right) + \frac{L_T}{r_i}\frac{I_o(r_i/L_T)}{I_1(r_i/L_T)} + \frac{L_T}{r_o}\frac{K_o(r_i/L_T)}{K_1(r_i/L_T)}\right]$$

[eq 5.6]

Where

i	=	Current across separation d
R_s	=	Semiconductor sheet resistance
L_T	=	Transfer length
I_0, I_1, K_0, K_1	=	Modified Bessel functions, and
r_i, r_o	=	Inner and outer radii of circular contact

When using low resistance (i.e. metal) contacts the Bessel function ratios (I_0/I_1 and K_0/K_1) approach unity, yielding equation 5.7:

$$\Delta V = \frac{IR_S}{2\pi}\left[ln\left(\frac{r_o}{r_i}\right) + \frac{L_T}{r_i} + \frac{L_T}{r_o}\right] \qquad \text{[eq 5.7]}$$

Provided the gap is sufficiently small ($r_o/r_i > 0.5$), the following can approximated:

$$ln\left(\frac{r_o}{r_i}\right) \approx \frac{r_o - r_i}{r_o} \qquad \text{[eq 5.8]}$$

This allows us to reduce equation 5.7 further to:

$$\Delta V = \frac{IR_S}{2\pi r_o}(r_o - r_i + 2L_T) \qquad \text{[eq 5.9]}$$

The total resistance between the contacts is defined as $R_T = \Delta V / I$, and defining the gap distance $d = r_o - r_i$, equation 5.9 can be expressed as a resistance:

$$R_T = \frac{R_S}{2\pi r_o}(d + 2L_T) \qquad \text{[eq 5.10]}$$

Equation 5.10 illustrates a linear relationship between gap distance (d) and total resistance, whose plot should have a slope of $R_a/2\pi r_o$ and a y intercept of $R_aL_T/\pi r_o$ (figure 5.20).

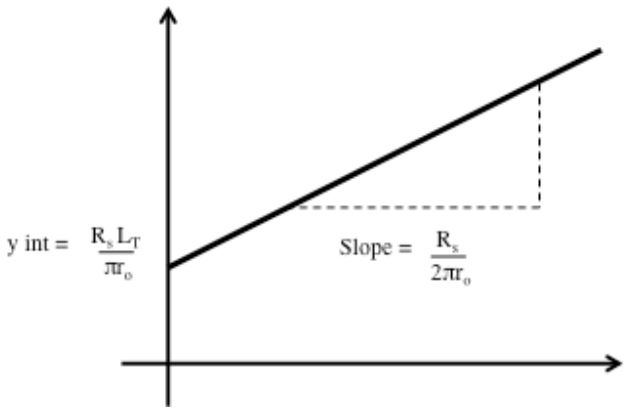

Figure 5.20: Graph of total resistance vs. CTLM gap distance. This relationship should be linear.

The transfer length is expressed as:

$$L_T = \sqrt{\frac{\rho_c}{R_s}} \qquad \text{[eq 5.11]}$$

This allows for a straightforward calculation of both contact and sheet resistance from the slope and y intercept:

$$R_s = 2\pi r_o\ (\mathbf{slope}) \qquad \text{[eq 5.12]}$$

$$\rho_c = (L_T)^2\ R_s = [\pi r_o(\mathbf{y\ int})]^2/R_s \qquad \text{[eq 5.13]}$$

5.5 Atomic Layer Deposition

Recent success was shown by encapsulating quantum dot monolayers with Al_2O_3 via an atomic layer deposition (ALD) process.[97] An ALD reactor was assembled for such a purpose. The technique used in this work employed trimethylaluminum (TMA) and water precursors as the aluminum and oxygen sources, respectively, a method shown to produce high quality Al_2O_3 films across a range of operating conditions.[98]

Atomic layer deposition is a conformal chemical vapor deposition method that relies on sequential, self terminating solid-gas reactions to form films with sub nanometer precision. A diagram of the apparatus is shown in figure 5.21. The reaction chamber has two lines leading to a shower head type inlet which provides both purge gasses and precursors to the chamber. This shower head is located directly (< 10 mm) above a heated substrate stage where the sample is placed. Nitrogen gas is continuously pumped at a rate of 20 sccm from two mass flow controllers (10 sccm each) at the rear of the two lines leading to the shower head. These two lines are also responsible for carrying precursor materials, one for inorganic sources (i.e oxygen) and another for metal-organic sources (i.e. TMA). The apparatus built for this study featured three inlet sources on the metalorganic line (right side of figure 5.21) for future use with other precursors. As TMA and many other metal-organics are pyrophoric it is advisable to “permanently” install these sources on the reactor, only replacing them when depleted. The three inlets on the metal-organic line allow users to experiment with several such sources without the need to remove any. The reactor has an outlet attached to a rotary vane pump with a globe valve in between.

The ALD reaction is straightforward: $Al(CH_3)_3$ reacts via ligand exchange with surface hydroxyl groups upon introduction to the substrate, a reaction which self terminates due to the steric hindrance of the methyl groups. After unreacted species are removed via nitrogen purge, H_2O is then introduced to the reactor where it reacts, also via ligand exchange, with the surface methyl groups. The system is again purged with nitrogen. Note that after this treatment, the surface is now predominately hydroxyl groups, and will support further $Al(CH_3)_3$ / H_2O cycles to build up an Al_2O_3 film.

After testing the system for integrity and performing an overnight vacuum bake, the following procedure was used to deposit ALD films:

Table 5.2

1. Set the MFCs to 0 sccm, fully open the globe valve and pump the system down. This brings the system pressure down to below 1 mT.

2. Set the MFCs to 10 sccm each and set the substrate heater PID to 150 ^oC. The system pressure is now approximately 26 mT.

3. Once the substrate heater has reached 150 ^oC, begin to close the globe valve to increase the pressure to 1.0 T. At this point there is now N_2 flowing through the system with a background pressure of 1.0 T and the substrate is at 150 ^oC.

4. A (user) pre-configured program is run which opens the H_2O ALD valve for 1.0 s, allows for 10.0 s of nitrogen purging, then opens the $Al(CH_3)_3$ valve, followed by a another 10.0 s of nitrogen purging. This process is repeated for each monolayer desired.

5. After deposition, the substrate heater is switched off and three pump-purge cycles are completed to remove any trace precursor material before exposing the system to atmosphere.

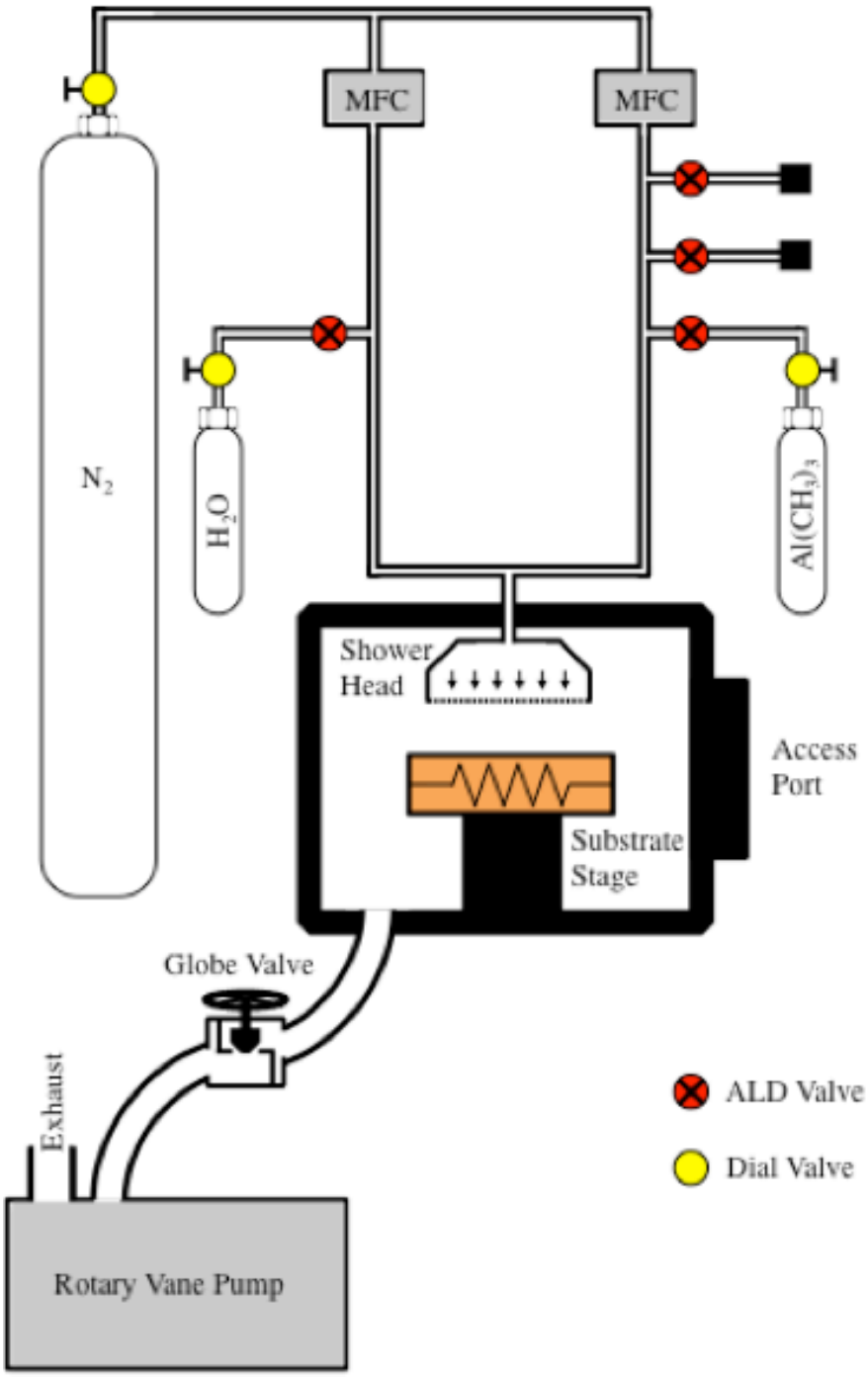

Figure 5.21: Diagram of assembled ALD reactor with H_2O and $Al(CH_3)_3$ sources.

CHAPTER 6: RESULTS AND CONCLUSIONS

The original intent was to fabricate devices from monolayers and multilayers of CdSe nanocrystal Langmuir films. Several reports of vertical devices have been published in the literature using various deposition techniques, including layer by layer (LbL) deposition,[99] traditional spin coating,[100] phase segregation assisted spin coating,[101] contact printing[102] and others. While reports of Langmuir films of CdSe exist, no devices have been reported using such a method. Devices were fabricated to probe the properties of such films in several configurations. Structures employing both vertical and horizontal charge transport were designed to elucidate the properties and structures of these films. It was found that reliable reproduction of these devices was difficult however, largely due to non-uniformities in the Langmuir monolayers.

3.1 Vertical Device Fabrication

The first device fabricated was a vertically oriented ITO-CdSe-ITO structure designed to probe excitonic effects at the CdSe-ITO interface (figure 6.1). This device is a nanoparticle analog of the Kallman and Pope experiment discussed in Chapter 2.[13] Glass slides were cut into 25 x 25 mm squares, rinsed in acetone, methanol and DI water and then heated to 120 ^{o}C for 120 seconds to remove any volatile compounds before being loaded into the sputtering system. 300 nm thick ITO films were sputtered as described in Chapter 5. The ITO coated glass slides were then coated with 1-20 Langmuir monolayers using both Blodgett and Schaffer techniques. A further 200-500 nm thick

film of ITO was sputtered onto the QD layer after masking the edges to prevent the ITO contacts from contacting each other. The dimensions of the top contact were 20 x 20 mm.

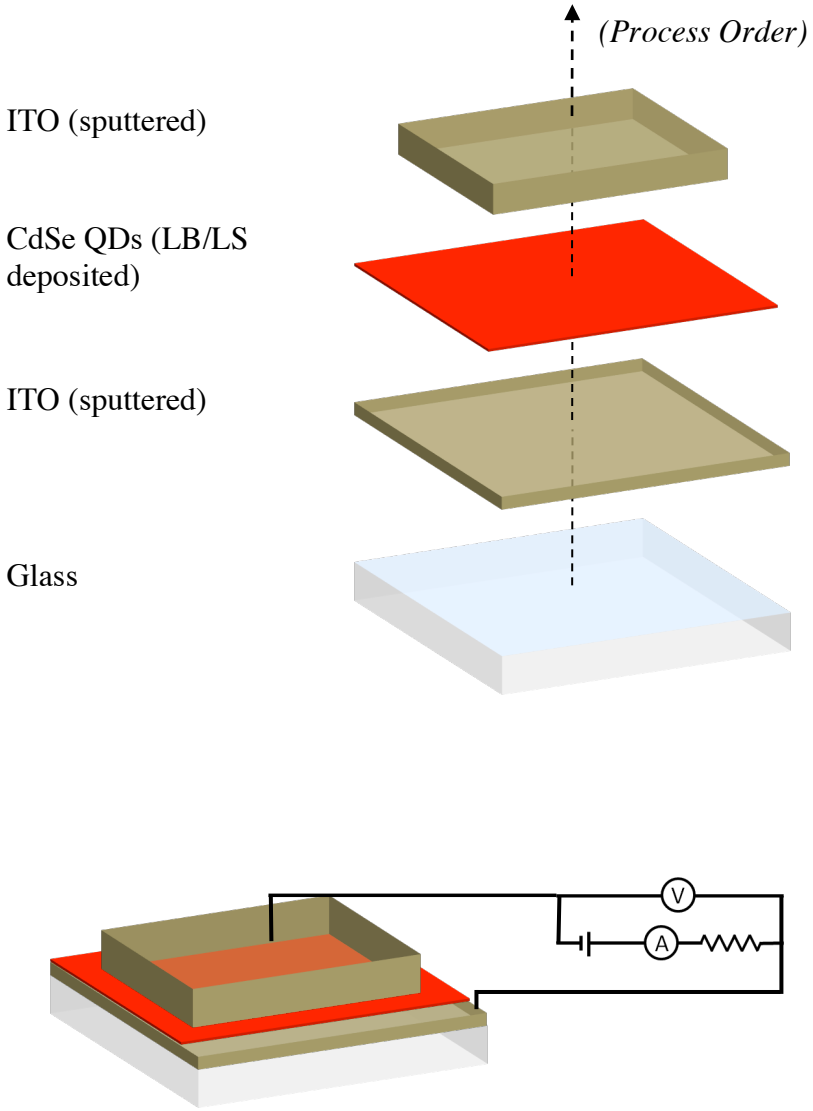

Figure 6.1: Deposition process for ITO-CdSe-ITO structure (top, exploded view) and electrical testing configuration (bottom, assembled view).

The initial batches of these devices were all shorted, showing a linear relationship between current and voltage consistent with a short due to the two contacts touching each

other. A device with zero CdSe monolayers (i.e. a deliberately shorted device) showed a resistance of 183 Ω. While this is somewhat higher than measured in Chapter 5 (10 Ω for a 200 nm thick film), it is important to note that this device consists of two ITO films, deposited on top of one another at different times and exposed to moisture and the atmosphere in between those depositions, just like a device with a Langmuir film deposited on it would be. Several devices that had Langmuir films deposited on them showed similar behavior (i.e. were shorted) and it was thought that the active area was (considerably) larger than it needed to be, thus by shrinking it the risk of a short could be reduced. We initially masked the 20 x 20 mm into four 7.5 x 7.5 mm squares (figure 6.2), but saw the same behavior observed with the larger 20 x 20 mm contact. In order to further reduce the top contact area, a physical mask was fabricated by drilling an array of 1.59 mm (1/16") holes into a 0.5 mm thick aluminum plate. By placing this mask on top of the glass-ITO-CdSe sample in the sputtering chamber, it was possible to fabricate dozens of devices on a single sample, both reducing the sample area (and the likelihood of "defects" in the QD film) and increasing the number of testable structures.

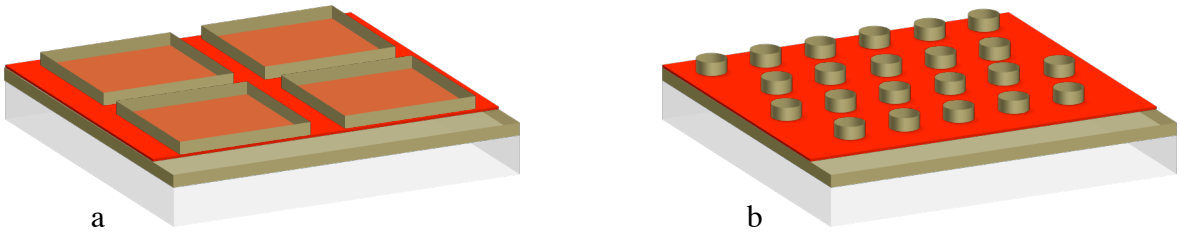

Figure 6.2: Second and third generation contact geometries, employing 56 mm^2 square contacts (a) and 1.98 mm^2 circular contacts (b).

Many devices tested demonstrated behavior indicating incomplete coverage of the bottom layer during the CdSe nanocrystal deposition process. It was considered that the ITO sputtering process could be damaging the underlying films and itself be responsible for the shorting of the devices, so experiments were conducted to vary the sputtering conditions in an attempt to improve device performance.

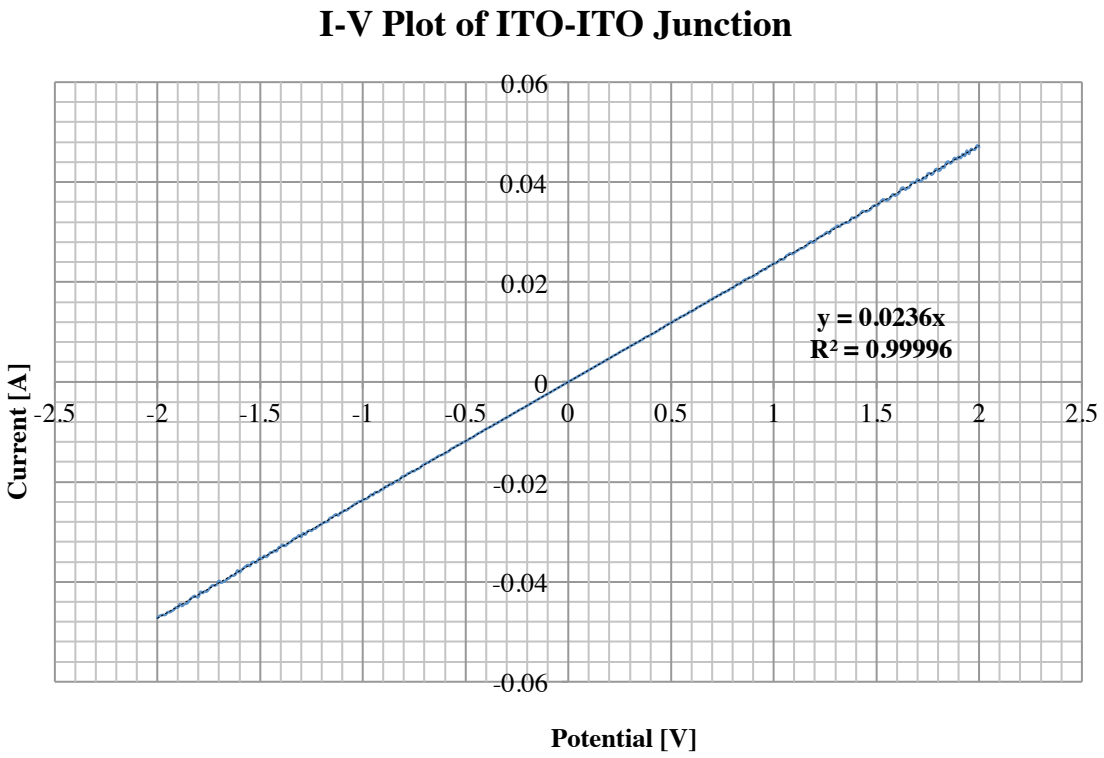

Figure 6.3: Current-voltage behavior of a deliberately shorted vertical device, illustrating direct contact between the top and bottom ITO films. This structure had a measured resistance of 42.19 Ω.

Two main possibilities exist for substrate damage during the sputtering process: Damage due to the impact of the target atoms (In, Sn, O) and damage due to the high energy neutral gas atoms (argon). Raising the background pressure will minimize the former, thermalizing the target atoms as they experience collisions more frequently.[103] Raising the pressure will increase the ratio of the high-energy neutral species however, increasing the rate of substrate bombardment.[104] Conversely one can lower the background pressure and achieve the opposite effect: a lower neutral species bombardment rate at the expense of more energetic target species impacting the substrate. Both approaches were tried but again yielded shorted devices, suggesting that either a) neither the target species (In, Sn, O) or neutral species (Ar) are responsible for device-compromising damage to the substrate or b) the sputtering process is inherently damaging to CdSe nanocrystal thin films to an extent that cannot be mitigated by modifying operating conditions. To rule out sputtering damage as the cause of the device shorts, another batch of devices was made using e-beam evaporated gold contacts instead of sputtered ITO.

Furthermore we deposited up to 25 monolayers of Al_2O_3 via an atomic layer deposition process outlined in Chapter 5. As ALD divides the deposition process into two half reactions, control over which surfaces are deposited on is afforded. In our CdSe-TOPO on ITO surface, for example, the covered areas are low energy, aliphatic hydrocarbons while the uncovered areas are higher energy oxides. By depositing the Al precursors (intended to react and form a monolayer on an oxygen terminated substrate) first, we could expect to coat the exposed oxide surface (the ITO substrate) without depositing on the CdSe QDs. Similarly, the subsequent oxygen precursor would form a monolayer only on the newly form Al-terminated surface, not the QDs themselves. This

allows for the aluminium oxide to "fill in" the gaps in the CdSe films, illustrated in figure 6.4. This technique has been used with moderate success by Lambert et al.[105]

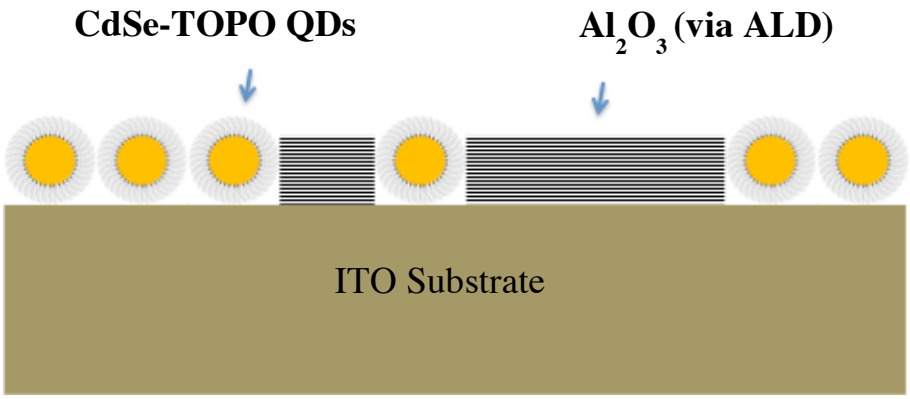

Figure 6.4: Illustration of Al_2O_3 films designed to form on the ITO substrate, without coating the CdSe covered portions of the sample.

6.2 Vertical Device Characterization

Many vertical devices exhibited behavior consistent with shorted top and bottom contacts, strongly suggesting that CdSe nanocrystal films were incomplete. This problem persisted with as many as 50 monolayers of CdSe nanocrystals deposited on the bottom contact, suggesting significant coverage problems with both Langmuir Blodgett and Langmuir Schaffer deposition methods. Langmuir Blodgett film devices in particular all showed low resistance, ohmic type behavior consistent with shorted devices. Devices fabricated with 5 Langmuir Schaffer monolayers were moderately more successful however, with several exhibiting highly resistive Schottky type conduction behavior consistent with transport through a colloidal quantum dot layer. Despite this, the majority

of the LS devices were still shorted. For the devices that exhibited such behavior, a linear fitting function passing through the origin was applied to the data:

As the x axis respresented potential and the y axis current, the fit equation takes the form:

$$y = mx + b \qquad \text{[eq 6.1]}$$

Plugging in the physical values of x and y, and setting the y intercept to zero yields:

$$I = mV \qquad \text{[eq 6.2]}$$

Which can be written in a more familiar form:

$$V = I\left(\frac{1}{m}\right) \qquad \text{[eq 6.3]}$$

This allows us to define resistance in terms of slope using Ohm's law:

$$V = IR \qquad \text{[eq 6.4]}$$

$$R = \left(\frac{1}{m}\right) \qquad \text{[eq 6.5]}$$

Devices were shorted across the range of conditions used in fabrication, including varying deposition pressures and varying numbers of ALD monolayers. For these ohmic devices, no apparent relation was found between these parameters and resistance. Furthermore, the resistances measured deviated significantly from the mean, indicating non-uniform characteristics from one device to another, despite the identical fabrication conditions for many of them. There did appear to be variations in device behavior

between 1.5 and 3.0 V, but these effects were not reproducible, even in scans occurring immediately following the previous measurement with no change in conditions or even probe position. It is conceivable that such effects are the result of degrading nanocrystal or ligand conduction pathways, but it is difficult to make any useful judgements from such varying measurements. The results from the shorted Langmuir Schaffer devices are shown in tables 6.1, 6.2 and 6.3.

Table 6.1: Current-voltage measurments for Langmuir Schaffer monolayers deposited at 26 mN/m with 0, 5, and 25 monolayers of ALD deposited before top contact ITO deposition. Ohmic results were fit to a linear function intersecting the origin, with the resistance found from the inverse of the slope. Coefficient of determination (R^2) is also reported for each fit as are average values and standard deviation.

26 mN/m Deposition Pressure					
0 ALD Monolayers		**5 ALD Monolayers**		**25 ALD Monolayers**	
Resistance (Ω)	**CoD**	**Resistance (Ω)**	**CoD**	**Resistance (Ω)**	**CoD**
127.286	0.98819	132.197	0.98030	147.059	0.99870
157.794	0.97172	100.016	0.99453	151.515	0.99783
135.500	0.99587	167.290	0.98727	208.333	0.98829
75.737	0.97720	118.611	0.99353	188.679	0.99540
89.474	0.99338	111.700	0.98430	185.185	0.99548
57.582	0.99368	90.554	0.99679	125.000	0.99885
118.448	0.99071	135.651	0.98216	136.986	0.99882
147.740	0.97833	120.968	0.98125	181.818	0.99547
117.213	0.97636	179.767	0.98622	151.515	0.99772
161.561	0.97389	155.456	0.98880	126.582	0.99989
85.927	0.97483	136.128	0.99862	75.758	0.99275
154.400	0.98079	77.594	0.98028	94.340	0.99581
		148.788	0.98942	96.154	0.99232
				86.957	0.99900
				76.923	0.99418
				86.957	0.99663
				77.519	0.97734
				76.923	0.99418
				75.758	0.99275
				86.957	0.99663
				86.957	0.99990
				95.238	0.99433
				84.034	0.99491
				96.154	0.99486
				98.039	0.98470
				83.333	0.99589
				77.519	0.97734
				95.238	0.99251
Avg Res (Ω)	**St Dev**	**Avg Res (Ω)**	**St Dev**	**Avg Res (Ω)**	**St Dev**
115.842	34.622	131.667	27.496	112.622	40.317

Table 6.2: Current-voltage measurments for Langmuir Schaffer monolayers deposited at 29 mN/m with 0, 5, and 25 monolayers of ALD deposited before top contact ITO deposition. Ohmic results were fit to a linear function intersecting the origin, with the resistance found from the inverse of the slope. Coefficient of determination (R^2) is also reported for each fit as are average values and standard deviation.

29 mN/m Deposition Pressure					
0 ALD Monolayers		**5 ALD Monolayers**		**25 ALD Monolayers**	
Resistance (Ω)	**CoD**	**Resistance (Ω)**	**CoD**	**Resistance (Ω)**	**CoD**
121.951	0.92069	121.951	0.98749	87.719	0.99652
160.804	0.96771	169.492	0.90842	113.636	0.98792
138.695	0.99983	125.000	0.97777	113.636	0.99220
128.200	0.97236	161.290	0.98393	131.579	0.99672
174.626	0.98228	175.439	0.99049	111.111	0.99625
129.193	0.97752	263.158	0.91167	169.492	0.96908
108.995	0.95751	169.492	0.90842		
88.960	0.95625	156.250	0.96652		
94.106	0.98096	47.170	0.99464		
116.437	0.96858	43.290	0.99943		
78.467	0.97285	48.077	0.97379		
54.601	0.95652	53.763	0.98659		
40.156	0.99484	46.512	0.99879		
29.294	0.95818	67.568	0.98898		
25.061	0.99818	44.248	0.98922		
16.118	0.95949	46.512	0.99879		
14.457	0.97209	67.568	0.98898		
		37.879	0.99999		
		51.546	0.99632		
		54.054	0.99807		
		53.476	0.99494		
Avg Res (Ω)	**St Dev**	**Avg Res (Ω)**	**St Dev**	**Avg Res (Ω)**	**St Dev**
89.419	51.583	95.416	63.958	121.196	27.484

Table 6.3: Current-voltage measurments for Langmuir Schaffer monolayers deposited at 32 mN/m with 0, 5, and 25 monolayers of ALD deposited before top contact ITO deposition. Ohmic results were fit to a linear function intersecting the origin, with the resistance found from the inverse of the slope. Coefficient of determination (R^2) is also reported for each fit as are average values and standard deviation.

32 mN/m Deposition Pressure					
0 ALD Monolayers		**5 ALD Monolayers**		**25 ALD Monolayers**	
Resistance (Ω)	**CoD**	**Resistance (Ω)**	**CoD**	**Resistance (Ω)**	**CoD**
64.516	0.99888	80.645	0.99891	94.340	0.98465
65.359	0.99825	80.645	0.99587	96.154	0.98111
91.743	0.99495	86.957	0.99967	149.254	0.98019
103.093	0.99094	86.207	0.99901	188.679	0.96739
108.696	0.98059	102.041	0.98543	111.111	0.98505
109.890	0.98631			147.059	0.96366
112.360	0.99329			178.571	0.9626
112.360	0.98719			200.000	0.97577
123.457	0.98101			158.730	0.96355
133.333	0.97867			86.207	0.99708
144.928	0.94249			104.167	0.99371
				117.647	0.99203
				98.039	0.97751
Avg Res (Ω)	**St Dev**	**Avg Res (Ω)**	**St Dev**	**Avg Res (Ω)**	**St Dev**
106.339	25.007	87.299	8.763	133.074	39.370

Despite a large majority of shorted devices, some of the devices did exhibit highly resistive, Schottky-type behavior. The I-V characterization of these devices is shown in figures 6.4-6.16 on the following pages. It is important to note that there is tremendous variation in resistance from one device to another, ranging from 10^3 to 10^9 Ω. There was no clear relation between deposition pressure or ALD treatments. No devices that received the 25 ALD monolayer treatment showed any diode-like characteristics (i.e. all

were shorted), indicating that perhaps such an ALD treatment was damaging to the nanocrystal films. It is not immediately clear why this would be, as the thermal (< 150 ºC) and atmospheric (> 10 mTorr) conditions during the ALD process are less extreme than the sputtering process (used to deposit top ITO contacts on all devices). Never the less, the highly resistive diode-like behavior was only observed in devices with either no ALD treatment or a 5 monolayer treatment. Perhaps most discouragingly, none of the devices showed any photoconductivity or photoenhancement, which would be expected of a core-conductive quantum dot film.

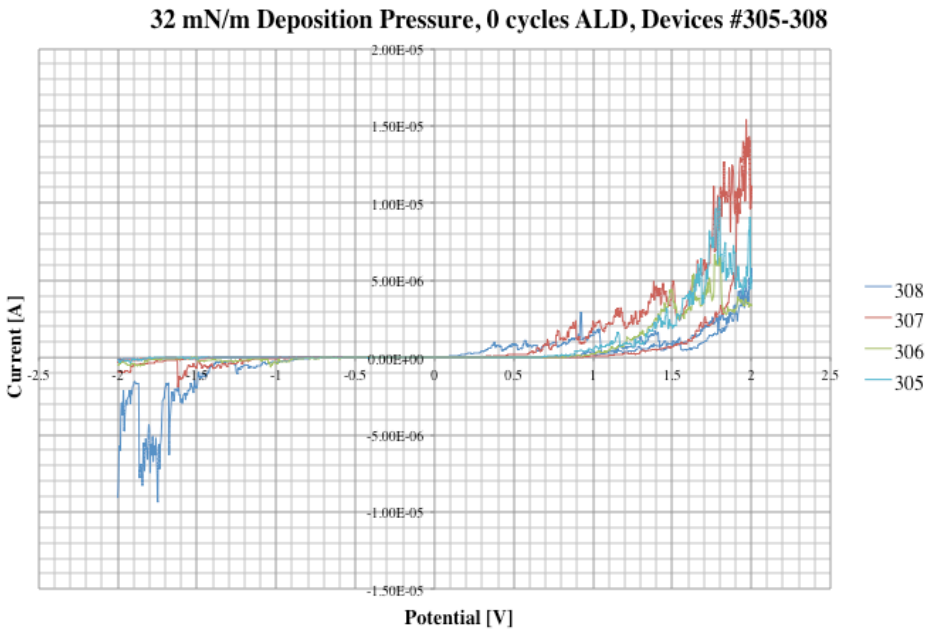

Figure 6.5: Current-voltage measurments for Langmuir Schaffer monolayers deposited at 32 mN/m with 0 cycles of ALD (0 monolayers of Al_2O_3) deposited before top contact ITO deposition.

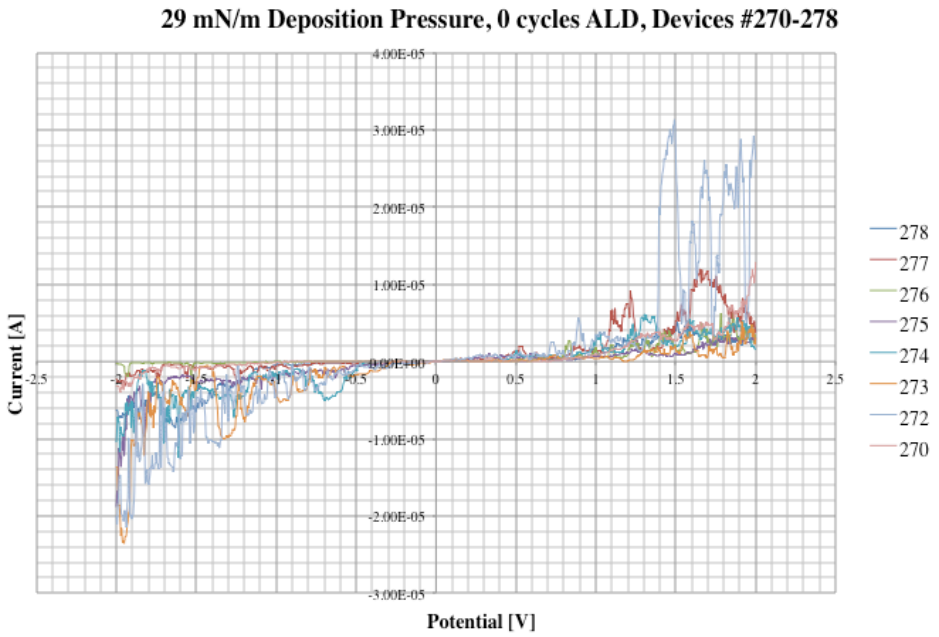

Figure 6.6: Current-voltage measurments for Langmuir Schaffer monolayers deposited at 29 mN/m with 0 cycles of ALD (0 monolayers of Al_2O_3) deposited before top contact ITO deposition.

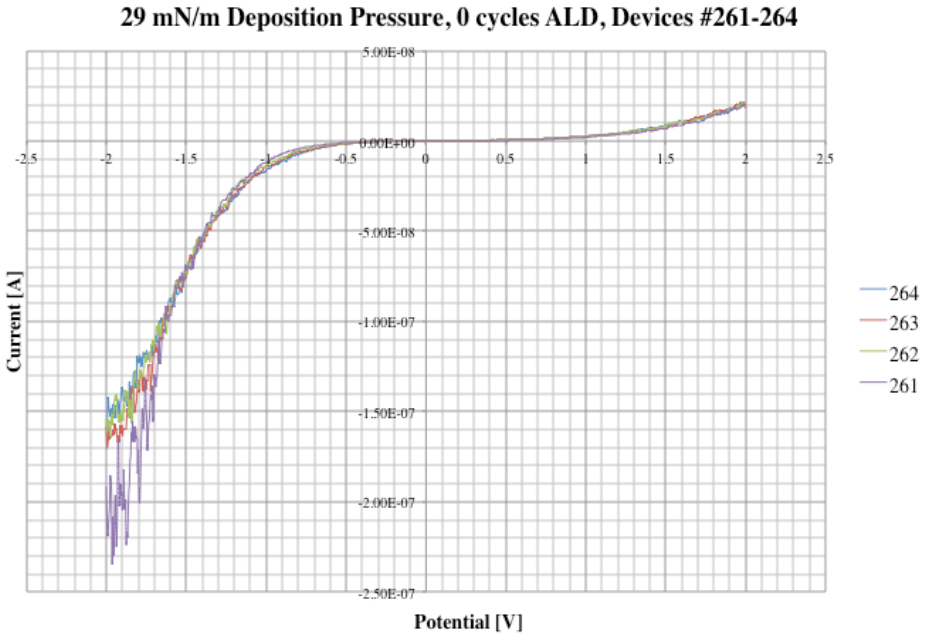

Figure 6.7: Current-voltage measurments for Langmuir Schaffer monolayers deposited at 29 mN/m with 0 cycles of ALD (0 monolayers of Al_2O_3) deposited before top contact ITO deposition.

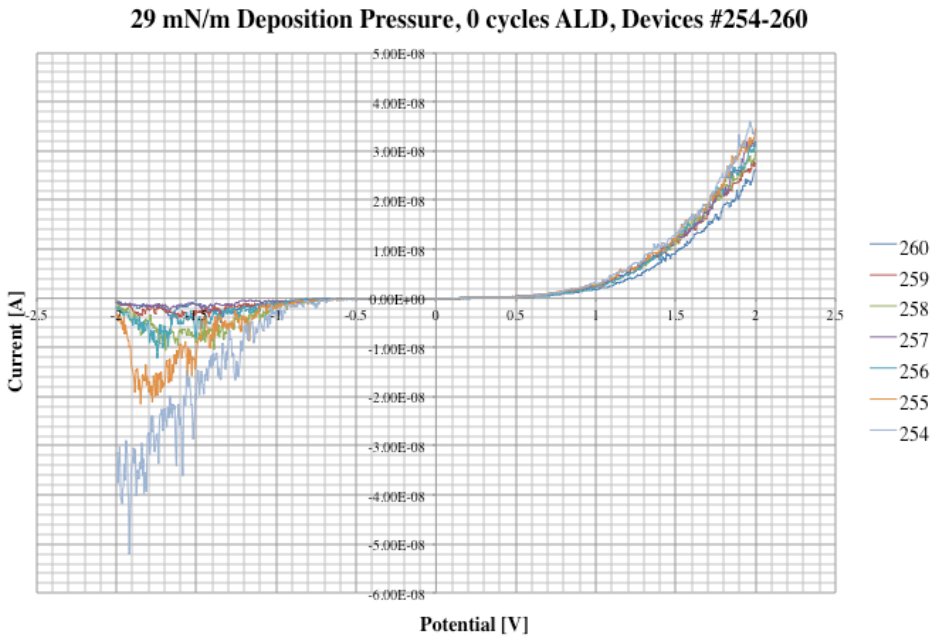

Figure 6.8: Current-voltage measurments for Langmuir Schaffer monolayers deposited at 29 mN/m with 0 cycles of ALD (0 monolayers of Al_2O_3) deposited before top contact ITO deposition.

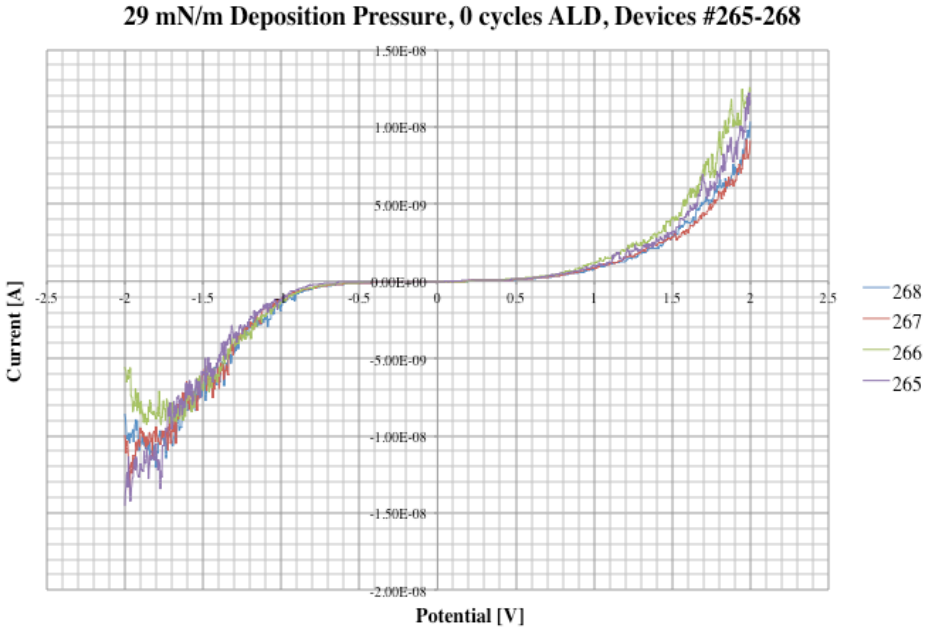

Figure 6.9: Current-voltage measurments for Langmuir Schaffer monolayers deposited at 29 mN/m with 0 cycles of ALD (0 monolayers of Al_2O_3) deposited before top contact ITO deposition.

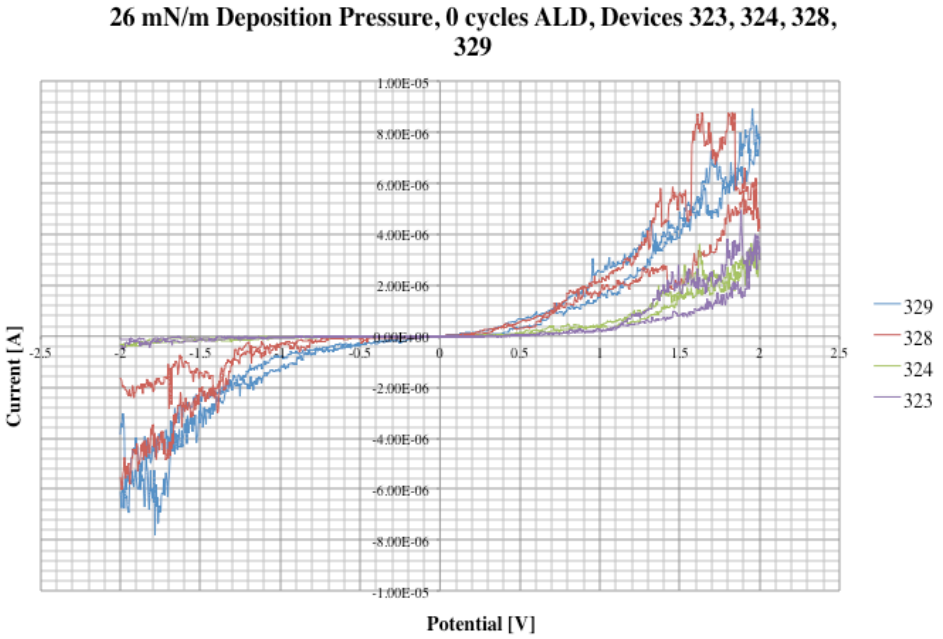

Figure 6.10: Current-voltage measurments for Langmuir Schaffer monolayers deposited at 26 mN/m with 0 cycles of ALD (0 monolayers of Al_2O_3) deposited before top contact ITO deposition.

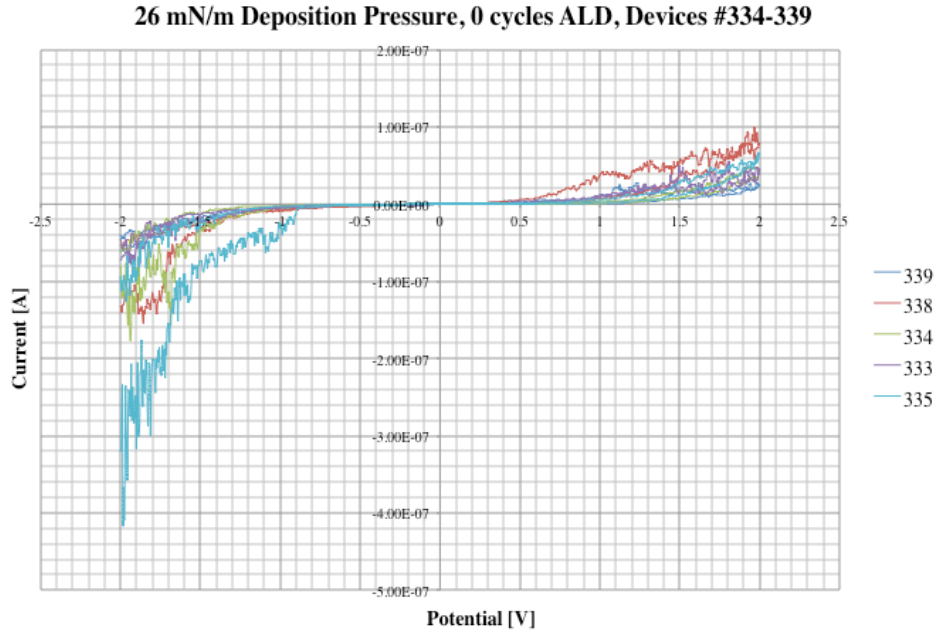

Figure 6.11: Current-voltage measurments for Langmuir Schaffer monolayers deposited at 26 mN/m with 0 cycles of ALD (0 monolayers of Al_2O_3) deposited before top contact ITO deposition.

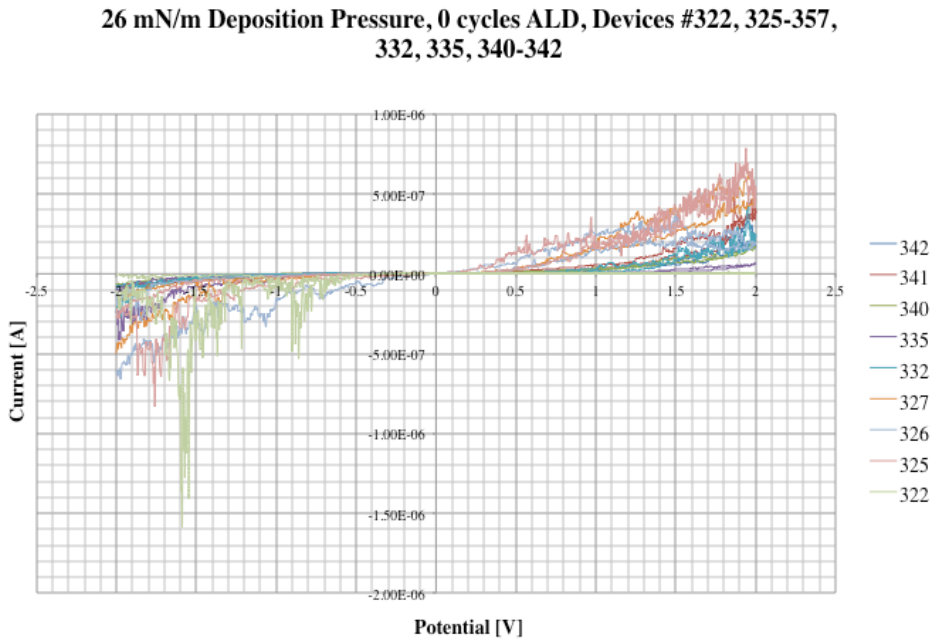

Figure 6.12: Current-voltage measurments for Langmuir Schaffer monolayers deposited at 26 mN/m with 0 cycles of ALD (0 monolayers of Al_2O_3) deposited before top contact ITO deposition.

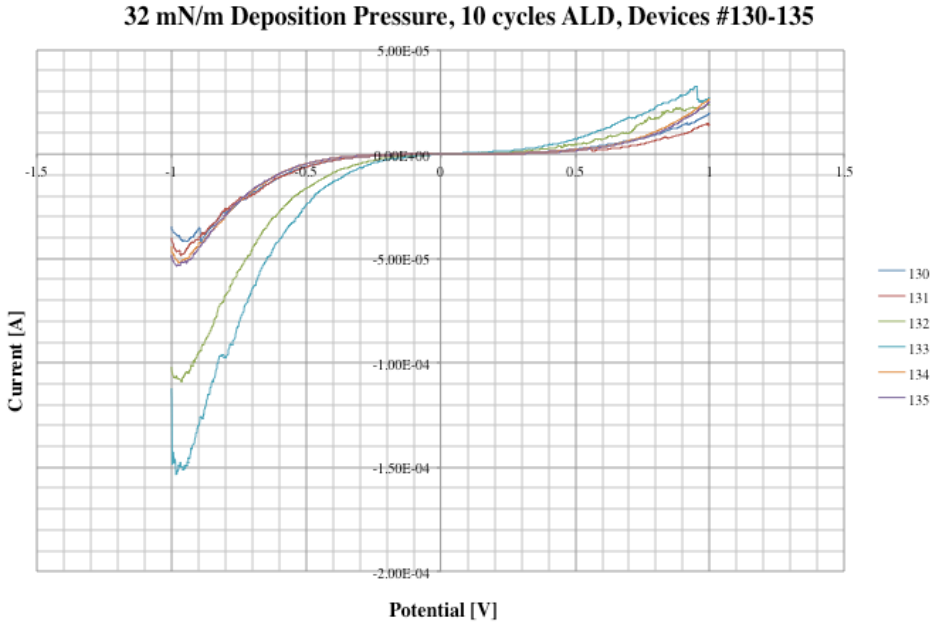

Figure 6.13: Current-voltage measurments for Langmuir Schaffer monolayers deposited at 32 mN/m with 10 cycles of ALD (0 monolayers of Al_2O_3) deposited before top contact ITO deposition.

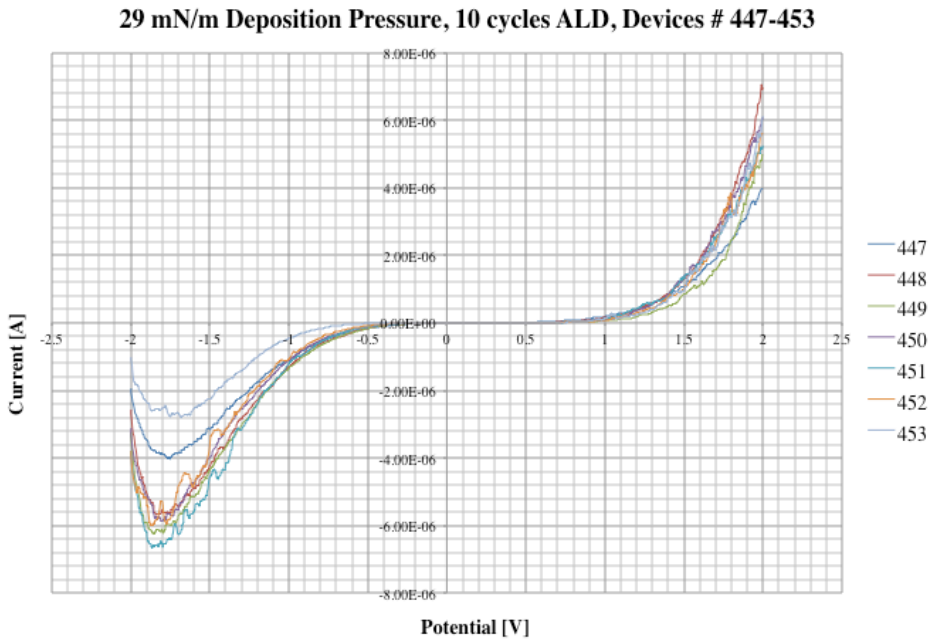

Figure 6.14: Current-voltage measurments for Langmuir Schaffer monolayers deposited at 29 mN/m with 10 cycles of ALD (5 monolayers of Al_2O_3) deposited before top contact ITO deposition.

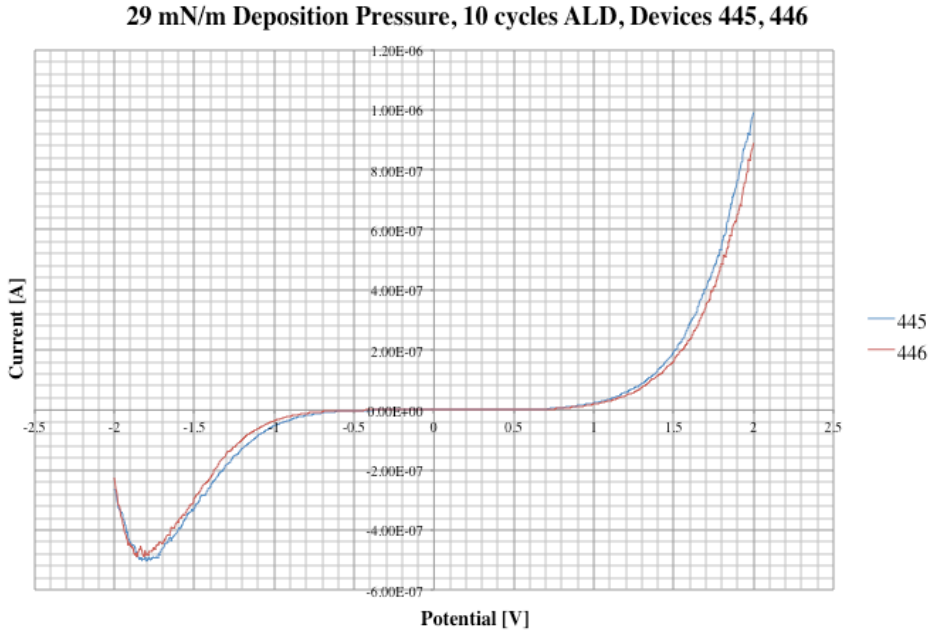

Figure 6.15: Current-voltage measurments for Langmuir Schaffer monolayers deposited at 29 mN/m with 10 cycles of ALD (5 monolayers of Al_2O_3) deposited before top contact ITO deposition.

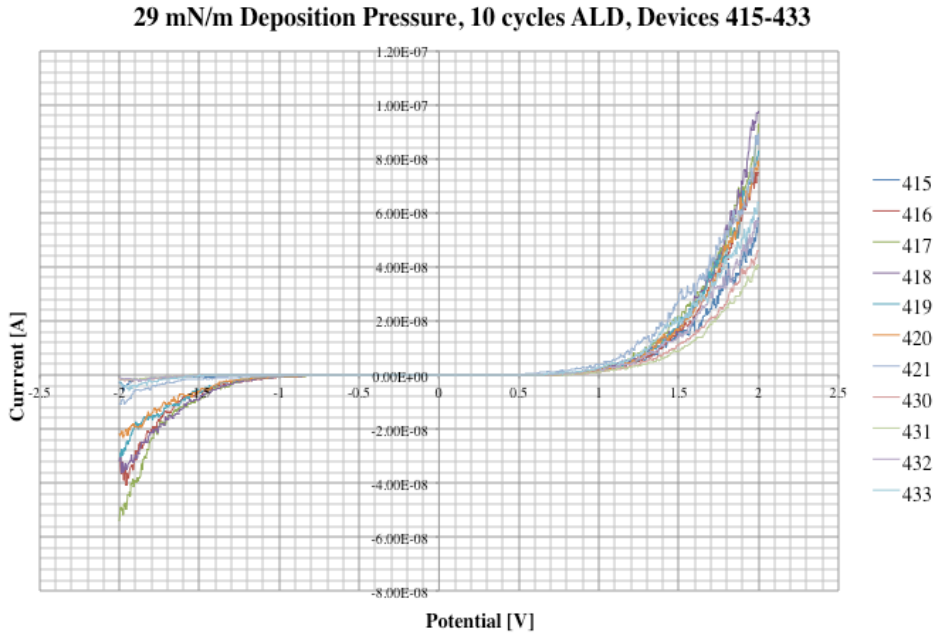

Figure 6.16: Current-voltage measurments for Langmuir Schaffer monolayers deposited at 29 mN/m with 10 cycles of ALD (5 monolayers of Al_2O_3) deposited before top contact ITO deposition.

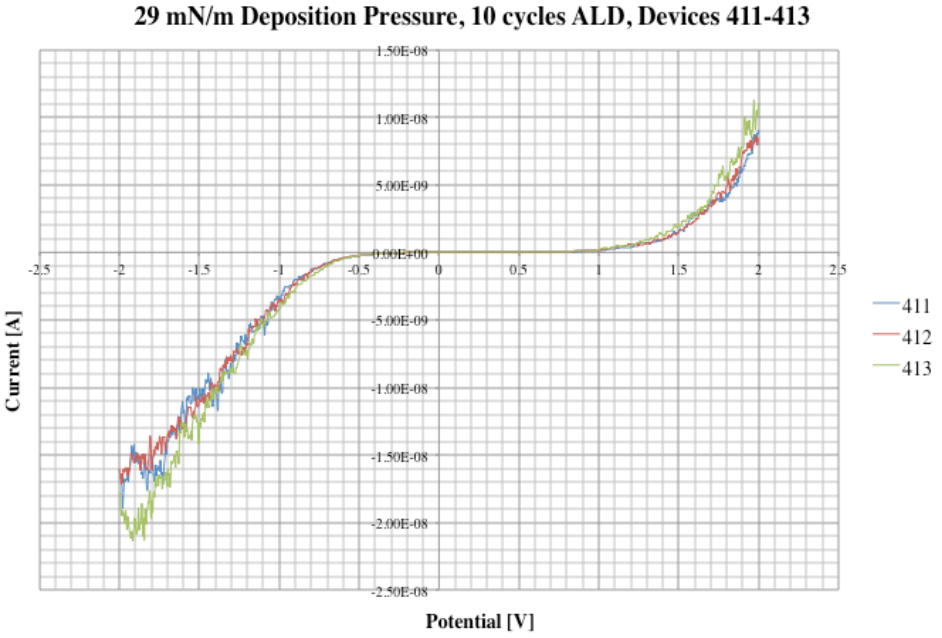

Figure 6.17: Current-voltage measurments for Langmuir Schaffer monolayers deposited at 29 mN/m with 10 cycles of ALD (5 monolayers of Al_2O_3) deposited before top contact ITO deposition.

6.3 Horizontal Device Characterization

As the nanocrystal films were of insufficient coverage to support vertical architecture, devices employing lateral current were fabricated. The idea was that a holey, or even lacey nanocrystal film morphology may support lateral conduction by merely "closing the circuit" between two contacts, instead of the complete coverage necessary for vertical device architecture. Circular transmission line method (CTLM) structures were fabricated as described in section 5.4 in order to probe such lateral conduction. These structures, like their vertical counterparts, were problematic. The fabrication process allowed for dozens of CTLM arrays on a single sample, affording many arrays to be tested across a variety of deposition conditions. The overwhelming majority of these devices showed no conduction. Over 100 of these structures were tested investiagting 2 main parameters: deposition type (LS and LB) and deposition pressure (26, 29 and 32 mN/m). While it was an initial goal to vary the number of films deposited and observe thickness dependent transport characteristics, it became quickly apparent that efforts to deposit one "monolayer" resulted in a significantly sub-monolayer film. Early structures employing 1, 5 and 15 monolayers were abandoned (after none showed any conduction) in favor of a 50 monolayer deposition process. Of these 100+ "50 monolayer" devices, only three showed conduction. All three were deposited at high pressure (32 mN/m) using the Langmuir Schaffer deposition technique. The rest of the devices, including those deposited at any pressure via the LB method as well as the 29 mN/m and 26 mN/m LS films, showed no meaningful current transport at potentials as high as +/- 20 V. An I-V plot of such an "open circuit" CTLM device is shown in figure 6.18.

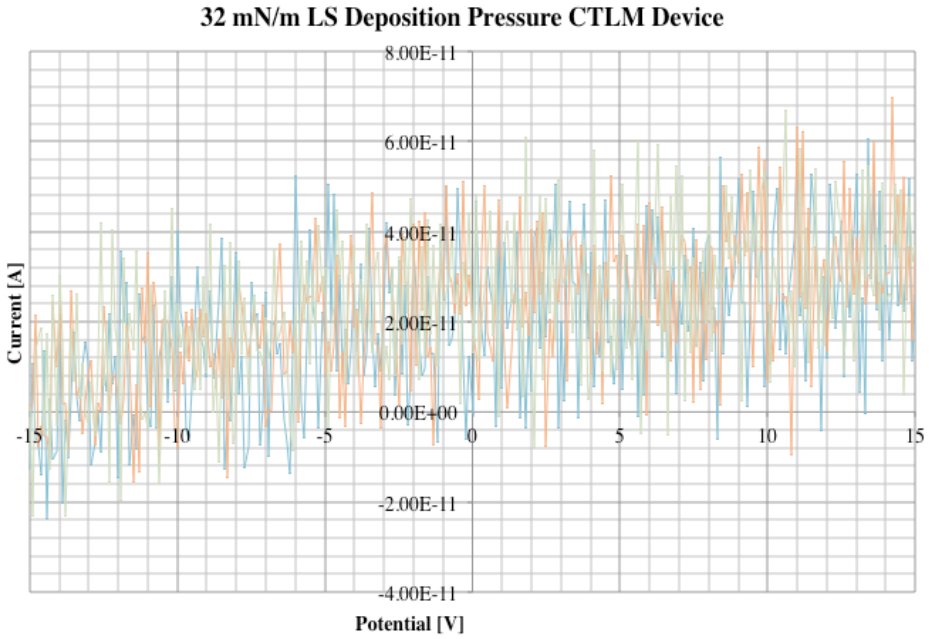

Figure 6.18: Current-voltage behavior of an open circuit horizontal CTLM device, suggesting a lack of a conduction pathway between the two contacts.

Of the devices that did exhibit conduction, the current magnitude varied considerably. Device 11 exhibited nanoamp currents (figure 6.19), device 29 exhibited currents between 100 pA and 1 nA (figure 6.20), and device 34 exhibited currents less than 50 pA (figure 6.21). The measured resistances can be plotted as a function of gap distance, which was done in figures 6.22, 6.23 and 6.24 for nine voltages (0.5, 1.0, 2.0, 3.0, 4.0, 5.0, 10.0 15.0, 20.0 V). This relationship should be linear, as derived theoretically in section 5.4. For the more conductive structure (device 11), the linear fits for the gap distance vs. resistance (figure 6.22) showed a positive correlation between with a moderate coefficient of determination (R^2_{avg} = .7721). Device 29, which exhibited less conductance also showed a correlation between gap distance vs. resistance (figure 6.23), but with a lower coefficient of determination (R^2_{avg} = .5219). Device 34 did not

show any positive correlation between gap distance and resistance as was not used in any further analysis.

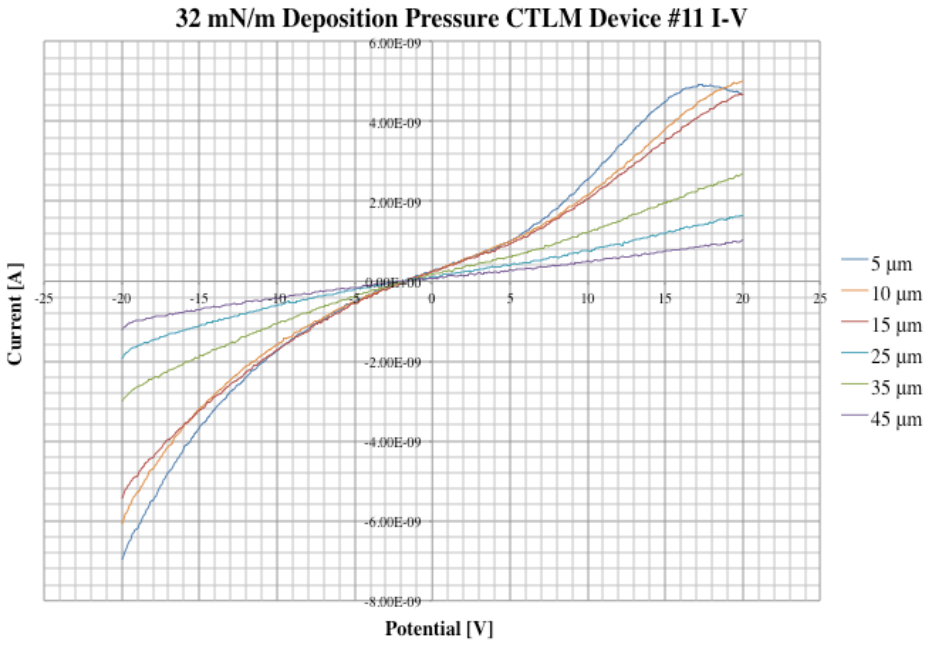

Figure 6.19: Current-voltage behavior of a CTLM device #11 with 50 Langmuir Schaffer monolayers deposited at 32 mN/m.

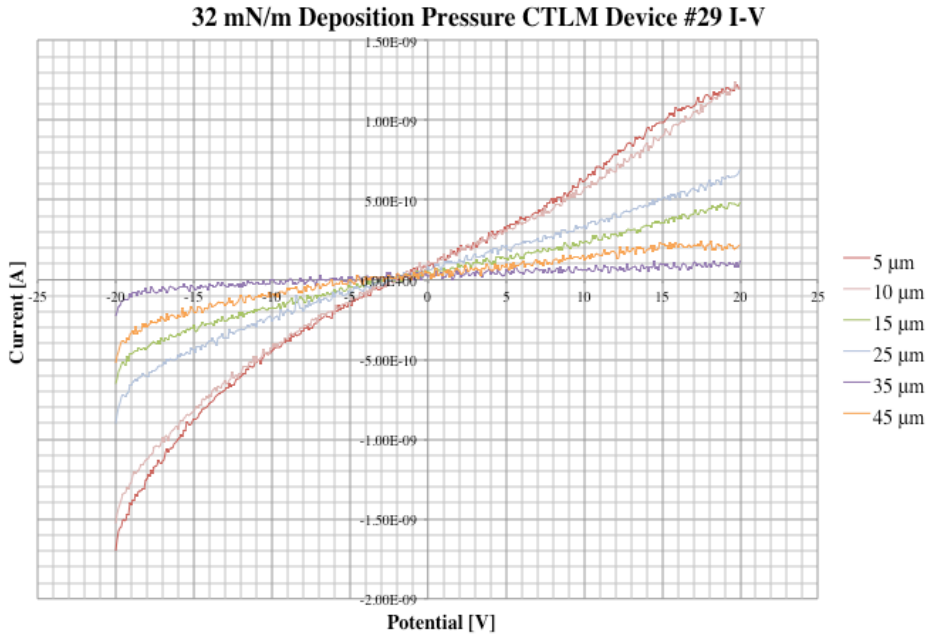

Figure 6.20: Current-voltage behavior of CTLM device #29 with 50 Langmuir Schaffer monolayers deposited at 32 mN/m.

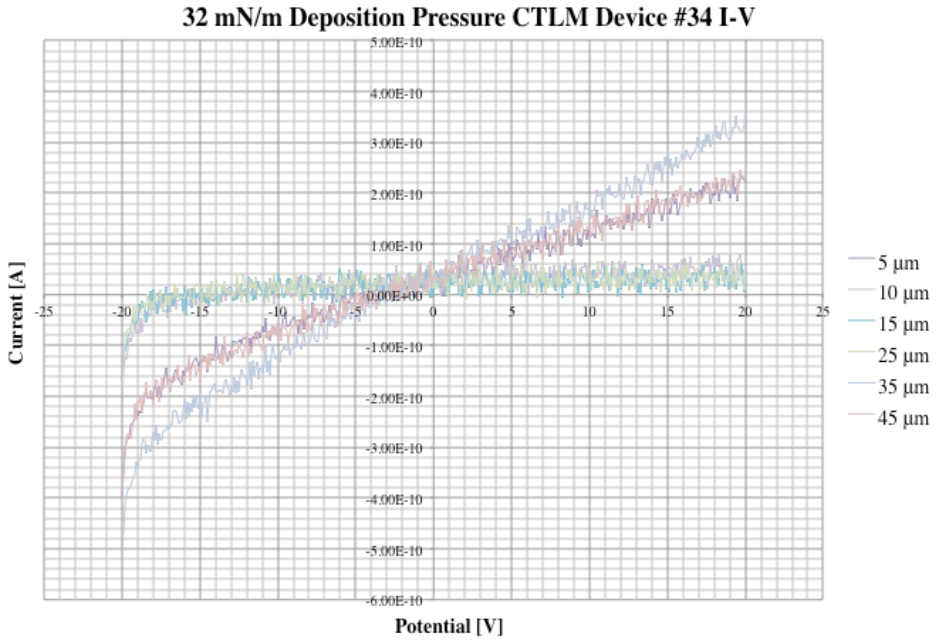

Figure 6.21: Current-voltage behavior of CTLM device #34 with 50 Langmuir Schaffer monolayers deposited at 32 mN/m.

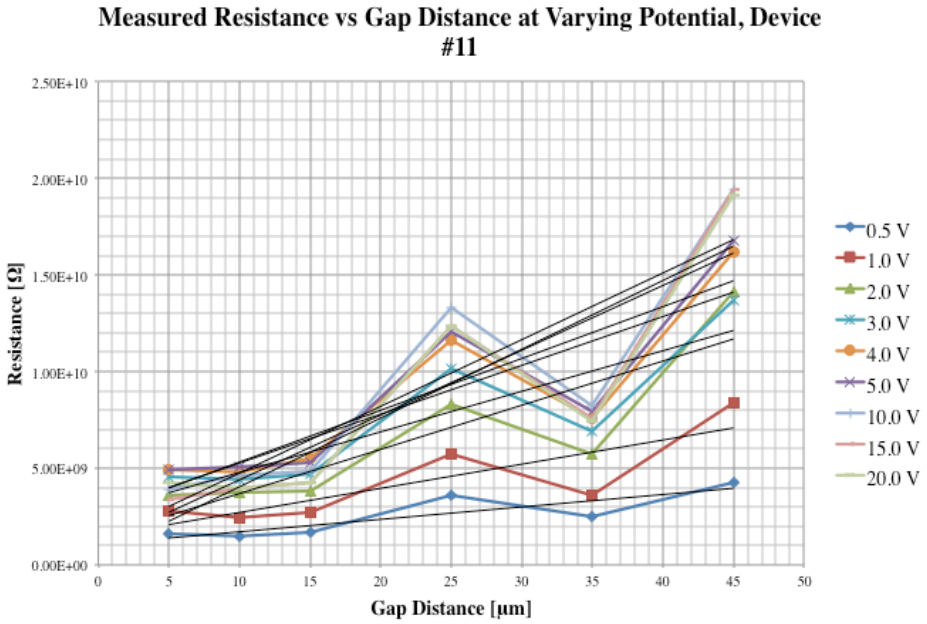

Figure 6.22: Resistance vs. Gap Distance Measurements for 50 ML LS CTLM structure # 11 at various biases.

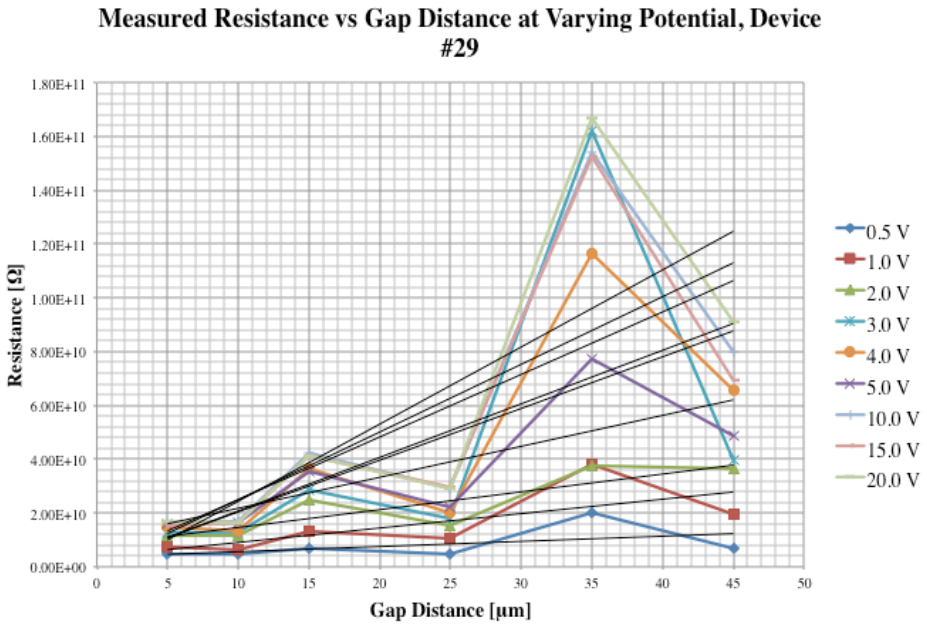

Figure 6.23: Resistance vs. Gap Distance Measurements for 50 ML LS CTLM structure #29 at various biases.

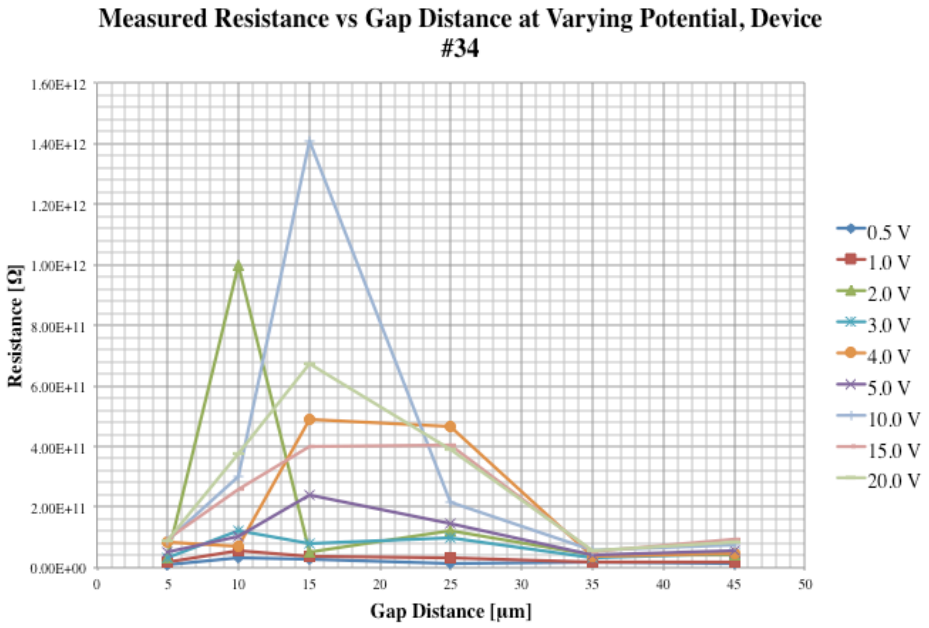

Figure 6.24: Resistance vs. Gap Distance Measurements for 50 ML LS CTLM structure #34 at various biases.

From these linear fits, we can extrapolate sheet and contact resistances for our films (figures 6.25 and 6.26). These results point to the tremendous difficulty in fabricating devices using Langmuir films of nanocrystals. Both contact and sheet resistances are not expected to vary with applied bias, the variations seen are due to differences in film morphology from one structure to the other.

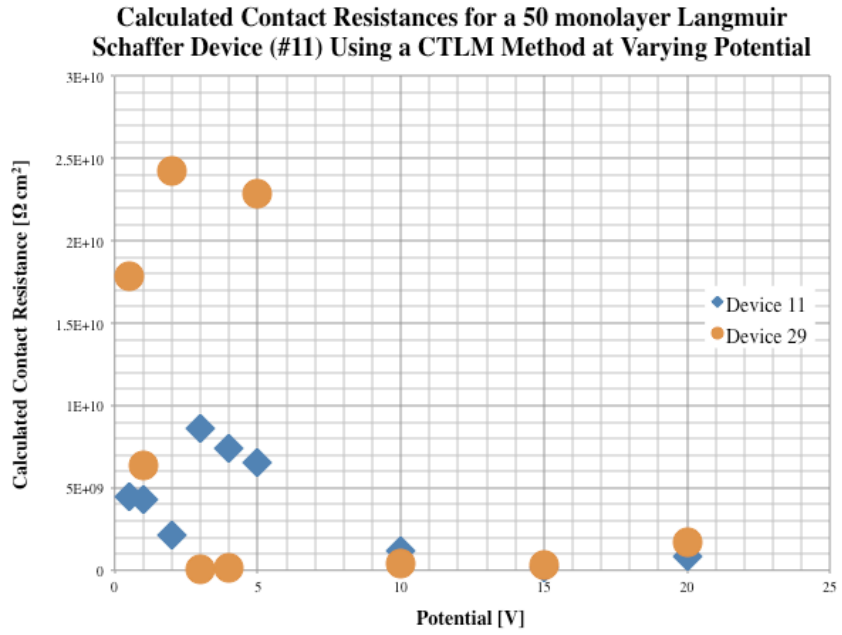

Figure 6.25: Measured contact resistance for 50 ML LS CTLM structure at various biases.

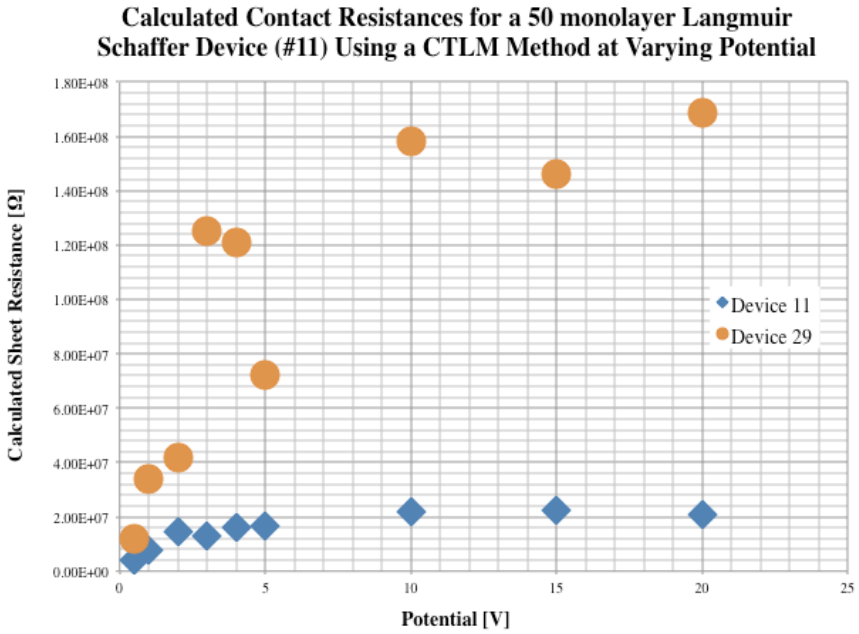

Figure 6.26: Measured sheet resistance for 50 ML LS CTLM structure at various biases.

CHAPTER 7: DISCUSSION AND FUTURE WORK

The monolayers produced by the Langmuir technique were largely insufficient to support device architectures, both vertical and horizontal. Despite using a range of deposition techniques and process variables, it was difficult to maintain consistency within given film conditions or even identify correlations between such conditions and general film properties. The lack of Langmuir films employed in electronic devices in the literature supports the idea that these films are inherently problematic. With the sterically large ligands used to maintain stability, the quantum dots remain far enough apart that no attractive force is felt to promote close packed films. These films exhibit hard-disk behavior upon compression, with no net attractive force driving their assembly. This is starkly different than the strong substrate-particle interactions that occur in Langmuir Blodgett and Langmuir Schaffer deposition techniques. This results in a nanoparticle film morphology that is dictated by the surface far more than by the Langmuir film itself. It is likely that well established techniques, namely the layer by layer technique is a better avenue for fabricating devices like those described in this work. The nature of stability at the air-water interface seems to be at odds with the need for a smaller interparticle distance to allow for controlled self-assembly. In a sense, Langmuir films of TOPO functionalized CdSe nanoparticles are not truly self-assembled, as there is no driving force of attraction between particles. The particles are only loosely held in a metastable

state: any introduction of a substrate will destroy any order previous obtained at the air-water interface.

It is perhaps worth exploring ligands that are sterically small enough to allow for stronger particle-particle interactions while maintaining sufficient separation to prevent irreversible aggregation. Energetically, this is an extremely fine line. The layer-by-layer techniques have become extremely well developed since the start of this work and now present a compelling case for their use in fabricating such device architectures and achieving such research goals. Langmuir films present a powerful platform to study nanoparticle behavior, but their applications in the deposition of films onto solid substrates is extremely limited in this author's opinion. Furthermore, they pose significant constraints of ligand selection, an important engineering consideration in the design of nanoparticle films.

Further work exploring novel Langmuir techniques should focus on the interaction of the nanoparticles, ligands, substrate and Langmuir subphase (which does not necessarily have to be water), as carefully balancing such interactions in such a system is critical to success.

REFERENCES

1. Murray C. B., K. C. R. B. M. G., Synthesis and characterization of monodisperse nanocrystals and close-packed nanocrystal assemblies. *Annual Review of Materials Science 30*, 545-610.

2. Murray, C. B.; Kagan, C. R.; Bawendi, M. G., Self-Organization of CdSe Nanocrystallites into Three-Dimensional Quantum Dot Superlattices. *Science* 1995, *270* (5240), 1335-1338.

3. Stiff-Roberts, A. D.; Zhang, W.; Jian, X.; Peng, H.; Everitt, H. O., Spin-Cast Deposition of CdSe-CdS Core-Shell Colloidal Quantum Dots on Doped GaAs Substrates: Structural and Optical Characterization. *Nanotechnology, IEEE Transactions on* 2007, *6* (4), 413-420.

4. Cassagneau, T.; Mallouk, T. E.; Fendler, J. H., Layer-by-layer assembly of thin film zener diodes from conducting polymers and CdSe nanoparticles. *Journal of the American Chemical Society* 1998, *120* (31), 7848-7859.

5. Kagan, C. R.; Murray, C. B.; Nirmal, M.; Bawendi, M. G., Electronic Energy Transfer in CdSe Quantum Dot Solids. *Physical Review Letters* 1996, *76* (9), 1517.

6. Dabbousi, B. O.; Murray, C. B.; Rubner, M. F.; Bawendi, M. G., Langmuir-Blodgett Manipulation of Size-Selected CdSe Nanocrystallites. *Chemistry of Materials* 1994, *6* (2), 216-219.

7. Ji, X. J.; Wang, C. S.; Xu, J. M.; Zheng, J. Y.; Gattas-Asfura, K. M.; Leblanc, R. M., Surface chemistry studies of (CdSe)ZnS quantum dots at the air-water interface. *Langmuir* 2005, *21* (12), 5377-5382.

8. Xu, J.; Ji, X.; Gattás-Asfura, K. M.; Wang, C.; Leblanc, R. M., Langmuir and Langmuir–Blodgett films of quantum dots. *Colloids and Surfaces A: Physicochemical and Engineering Aspects* 2006, *284–285* (0), 35-42.

9. Lambert, K.; Čapek, R. K.; Bodnarchuk, M. I.; Kovalenko, M. V.; Van Thourhout, D.; Heiss, W.; Hens, Z., Langmuir−Schaefer Deposition of Quantum Dot Multilayers. *Langmuir* 2010, *26* (11), 7732-7736.

10. Chen, J.; Song, J. L.; Sun, X. W.; Deng, W. Q.; Jiang, C. Y.; Lei, W.; Huang, J. H.; Liu, R. S., An oleic acid-capped CdSe quantum-dot sensitized solar cell. *Applied Physics Letters* 2009, *94* (15), 153115-3.

11. Brus, L. E., A simple model for the ionization potential, electron affinity, and aqueous redox potentials of small semiconductor crystallites. *The Journal of Chemical Physics* 1983, *79* (11), 5566-5571.

12. Liang, W. Y., Excitons. *Physics Education* 1970, (5), 226-228.

13. Kang, M. S.; Sahu, A.; Norris, D. J.; Frisbie, C. D., Size-Dependent Electrical Transport in CdSe Nanocrystal Thin Films. *Nano Letters* 2010, *10* (9), 3727-3732.

14. Lyde, D. R., CRC Handbook of Chemistry and Physics. 1998, (78).

15. Nozik, A. J., Quantum dot solar cells. *Physica E* 2002, *14*, 115-120.

16. Gregg, B. A., Excitonic Solar Cells. *Journal of Physical Chemistry B* 2003, *107* (20), 4688-4698.

17. Hines, M. A.; Guyot-Sionnest, P., Synthesis and Characterization of Strongly Luminescing ZnS-Capped CdSe Nanocrystals. *The Journal of Physical Chemistry* 1996, *100* (2), 468-471.

18. Murray, C. B.; Norris, D. J.; Bawendi, M. G., Synthesis and characterization of nearly monodisperse CdE (E = sulfur, selenium, tellurium) semiconductor nanocrystallites. *Journal of the American Chemical Society* 1993, *115* (19), 8706-8715.

19. Markus, T. Z.; Wu, M.; Wang, L.; Waldeck, D. H.; Oron, D.; Naaman, R., Electronic Structure of CdSe Nanoparticles Adsorbed on Au Electrodes by an Organic Linker: Fermi Level Pinning of the HOMO. *Journal of Physical Chemistry C* 2009, *113* (32), 14200-14206.

20. Yu, W. W.; Qu, L.; Guo, W.; Peng, X., Experimental Determination of the Extinction Coefficient of CdTe, CdSe, and CdS Nanocrystals. *Chemistry of Materials* 2003, *15* (14), 2854-2860.

21. Weiss, E. A.; Chiechi, R. C.; Geyer, S. M.; Porter, V. J.; Bell, D. C.; Bawendi, M. G.; Whitesides, G. M., Size-Dependant Charge Collection in Junctions Containing Single-Size and Multi-Size Arrays of Colloidal CdSe Quantum Dots. *Journal of the American Chemical Soceity* 2007, *130* (1), 74-82.

22. Kallmann, H.; Pope, M., Photovoltaic Effect in Organic Crystals. *Journal of Chemical Physics* 1959, *30* (2), 585-586.

23. Kallmann, H.; Pope, M., Bulk Conductivity in Organic Crystals. *Nature* 1960, *186* (4718), 31-33.

24. Geacintov, N.; Pope, M.; Kallmann, H., Photogeneration of Charge Carriers in Tetracene. *Journal of Chemical Physics* 1966, *45* (7), 2639-2649.

25. Gregg, B. A.; Fox, M. A.; Bard, A. J., Photovoltaic effect in symmetrical cells of a liquid crystal porphyrin. *The Journal of Physical Chemistry* 1990, *94* (4), 1586-1598.

26. Gregg, B. A., Photovoltaic properties of a molecular semiconductor modulated by an exciton-dissociating film. *Applied Physics Letters* 1995, *67* (9), 1271-1273.

27. Gubin, S. P.; Kataeva, N. A.; Khomutov, G. B., Promising Avenues of Research in Nanoscience: Chemistry of Semiconductor Nanoparticles. *Russian Chemical Bulletin, International Edition* 2005, *54* (4), 827-852.

28. Kamat, P. V., Meeting the Clean Energy Demand: Nanostructure Architectures for Solar Energy Conversion. *Journal of Physical Chemistry C* 2007, *111* (7), 2834-2860.

29. Hillhouse, H. W.; Beard, M. C., Solar cells from colloidal nanocrystals: Fundamentals, materials, devices, and economics. *Current Opinion in Colloid & Interface Science* 2009, *14* (4), 245-259.

30. Talapin, D. V.; Rogach, A. L.; Kornowski, A.; Haase, M.; Weller, H., Highly Luminescent Monodisperse CdSe and CdSe/ZnS Nanocrystals Synthesized in a Hexadecylamine−Trioctylphosphine Oxide−Trioctylphospine Mixture. *Nano Letters* 2001, *1* (4), 207-211.

31. Beard, M. C.; Turner, G. M.; Murphy, J. E.; Micic, O. I.; Hanna, M. C.; Nozik, A. J.; Schmuttenmaer, C. A., Electronic Coupling in InP Nanoparticle Arrays. *Nano Letters* 2003, *3* (12), 1695-1699.

32. Jarosz, M. V.; Porter, V. J.; Fisher, B. R.; Kastner, M. A.; Bawendi, M. G., Photoconductivity studies of treated CdSe quantum dot films exhibiting increased exciton ionization efficiency. *Physical Review B* 2004, *70* (19), 195327.

33. Vanmaekelbergh, D. A. M.; Liljeroth, P., Electron-conducting quantum dot solids: novel materials based on colloidal semiconductor nanocrystals. Royal Society of Chemistry: 2005.

34. Huang, J.; Stockwell, D.; Huang, Z.; Mohler, D. L.; Lian, T., Photoinduced Ultrafast Electron Transfer from CdSe Quantum Dots to Re-bipyridyl Complexes. *Journal of the American Chemical Society* 2008, *130* (17), 5632-5633.

35. Sykora, M.; Petruska, M. A.; Alstrum-Acevedo, J.; Bezel, I.; Meyer, T. J.; Klimov, V. I., Photoinduced Charge Transfer between CdSe Nanocrystal Quantum Dots and Ru−Polypyridine Complexes. *Journal of the American Chemical Society* 2006, *128* (31), 9984-9985.

36. Adams, D. M.; Brus, L.; Chidsey, C. E. D.; Creager, S.; Creutz, C.; Kagan, C. R.; Kamat, P. V.; Lieberman, M.; Lindsay, S.; Marcus, R. A.; Metzger, R. M.; Michel-Beyerle, M. E.; Miller, J. R.; Newton, M. D.; Rolison, D. R.; Sankey, O.; Schanze, K. S.; Yardley, J.; Zhu, X., Charge Transfer on the Nanoscale: Current Status. *The Journal of Physical Chemistry B* 2003, *107* (28), 6668-6697.

37. Robel, I.; Subramanian, V.; Kuno, M.; Kamat, P. V., Quantum Dot Solar Cells. Harvesting Light Energy with CdSe Nanocrystals Molecularly Linked to Mesoscopic TiO2 Films. *Journal of the American Chemical Society* 2006, *128* (7), 2385-2393.

38. Pearson, R. G., Hard and soft acids and bases, HSAB, part 1: Fundamental principles. *Journal of Chemical Education* 1968, *45* (9), 581-null.

39. Arango, A. C.; Oertel, D. C.; Xu, Y.; Bawendi, M. G.; Bulović, V., Heterojunction Photovoltaics Using Printed Colloidal Quantum Dots as a Photosensitive Layer. *Nano Letters* 2009, *9* (2), 860-863.

40. Bullen, C.; Mulvaney, P., The Effects of Chemisorption on the Luminescence of CdSe Quantum Dots. *Langmuir* 2006, *22* (7), 3007-3013.

41. Chen, Z.; Berciaud, S. p.; Nuckolls, C.; Heinz, T. F.; Brus, L. E., Energy Transfer from Individual Semiconductor Nanocrystals to Graphene. *ACS Nano* 2010, *4* (5), 2964-2968.

42. Jin, S.; Lian, T., Electron Transfer Dynamics from Single CdSe/ZnS Quantum Dots to TiO2 Nanoparticles. *Nano Letters* 2009, *9* (6), 2448-2454.

43. Kinge, S.; Crego-Calama, M.; Reinhoudt, D. N., Self-Assembling Nanoparticles at Surfaces and Interfaces. *ChemPhysChem* 2008, *9* (1), 20-42.

44. Kovalenko, M. V.; Scheele, M.; Talapin, D. V., Colloidal Nanocrystals with Molecular Metal Chalcogenide Surface Ligands. *Science* 2009, *324* (5933), 1417-1420.

45. Osedach, T. P.; Geyer, S. M.; Ho, J. C.; Arango, A. C.; Bawendi, M. G.; Bulovic, V., Lateral heterojunction photodetector consisting of molecular organic and colloidal quantum dot thin films. *Applied Physics Letters* 2009, *94* (4), 043307-3.

46. Schapotschnikow, P.; Hommersom, B.; Vlugt, T. J. H., Adsorption and Binding of Ligands to CdSe Nanocrystals. *The Journal of Physical Chemistry C* 2009, *113* (29), 12690-12698.

47. Talapin, D. V.; Murray, C. B., PbSe Nanocrystal Solids for n- and p-Channel Thin Film Field Effect Transistors. *Science* 2005, *310*, 86-89.

48. Talgorn, E.; Moysidou, E.; Abellon, R. D.; Savenije, T. J.; Goossens, A.; Houtepen, A. J.; Siebbeles, L. D. A., Highly Photoconductive CdSe Quantum-Dot Films: Influence of Capping Molecules and Film Preparation Procedure. *The Journal of Physical Chemistry C* 2010, *114* (8), 3441-3447.

49. Steckel, J.; Coe-Sullivan, S.; Bulović, V.; Bawendi, M., 1.3 μm to 1.55 μm Tunable Electroluminescence from PbSe Quantum Dots Embedded within an Organic Device. *Advanced Materials* 2003, *15* (21), 1862-1866.

50. Klinke, C.; Chen, J.; Afzali, A.; Avouris, P., Charge Transfer Induced Polarity Switching in Carbon Nanotube Transistors. *Nano Letters* 2005, *5* (3), 555-558.

51. Dabbousi, B. O.; Murray, C. B.; Rubner, M. F.; Bawendi, M. G., Langmuir-Blodgett Manipulation of Size-Selected CdSe Nanocrystallites. *Chemistry of Materials* 1994, *6* (2), 216-219.

52. Xu, J.; Ji, X.; Gattás-Asfura, K. M.; Wang, C.; Leblanc, R. M., Langmuir and Langmuir–Blodgett films of quantum dots. *Colloids and Surfaces A: Physicochemical and Engineering Aspects* 2006, *284–285* (0), 35-42.

53. Cordero, S. R.; Carson, P. J.; Estabrook, R. A.; Strouse, G. F.; Buratto, S. K., Photo-Activated Luminescence of CdSe Quantum Dot Monolayers. *The Journal of Physical Chemistry B* 2000, *104* (51), 12137-12142.

54. Gattás-Asfura, K. M.; Constantine, C. A.; Lynn, M. J.; Thimann, D. A.; Ji, X.; Leblanc, R. M., Characterization and 2D Self-Assembly of CdSe Quantum Dots at the Air−Water Interface. *Journal of the American Chemical Society* 2005, *127* (42), 14640-14646.

55. Jasieniak, J.; Smith, L.; Embden, J. v.; Mulvaney, P.; Califano, M., Re-examination of the Size-Dependent Absorption Properties of CdSe Quantum Dots. 2009, *113* (45).

56. Leatherdale, C. A.; Woo, W. K.; Mikulec, F. V.; Bawendi, M. G., On the Absorption Cross Section of CdSe Nanocrystal Quantum Dots. *The Journal of Physical Chemistry B* 2002, *106* (31), 7619-7622.

57. Norris, D. J.; Bawendi, M. G., Measurement and assignment of the size-dependent optical spectrum in CdSe quantum dots. *Physical Review B* 1996, *53* (24), 16338.

58. Brus, L., Electronic wave functions in semiconductor clusters: experiment and theory. *The Journal of Physical Chemistry* 1986, *90* (12), 2555-2560.

59. *MATLAB*, The Mathworks, Inc: Natick, MA, 2009.

60. Kinge, S.; Crego-Calama, M.; Reinhoudt, D., Self-Assembling at Surfaces and Interfaces. *ChemPhysChem* 2008, *9* (1).

61. Franklin, B.; Brownrigg, W.; Farish, M., On the Stilling of Waves by Means of Oil. *Philosophical Transactions* 1774, *64*, 445-460.

62. Pockels, A.; Raleigh, Surface Tension. *Nature* 1891, *43*, 437-439.

63. Langmuir, I., THE CONSTITUTION AND FUNDAMENTAL PROPERTIES OF SOLIDS AND LIQUIDS. II. LIQUIDS.1. *Journal of the American Chemical Society* 1917, *39* (9), 1848-1906.

64. Blodgett, K., Film Structure and Method of Preparation. *USPTO* 1940, *US2220860*.

65. Petty, M. C., *Langmuir Blodgett Films: An Introduction*. Cambridge University Press: Cambridge, 1996.

66. Millipore Water in the Laboratory - A Tutorial. http://www.millipore.com/lab_water/clw4/tutorial (accessed March 13th, 2013).

67. Pashley, R. M.; Rzechowicz, M.; Pashley, L. R.; Francis, M. J., De-Gassed Water Is a Better Cleaning Agent. *The Journal of Physical Chemistry B* 2004, *109* (3), 1231-1238.

68. Oswerhchap, Handbook of Chemical Hazard Analysis Procedures. Federal Emergency Management Agency, U. S. D. o. T., U.S. Environmental Protection Agency, Ed. Federal Emergency Management Agency: Washington, DC, 1990.

69. Kenn, R. M.; Boehm, C.; Bibo, A. M.; Peterson, I. R.; Moehwald, H.; Als-Nielsen, J.; Kjaer, K., Mesophases and crystalline phases in fatty acid monolayers. *The Journal of Physical Chemistry* 1991, *95* (5), 2092-2097.

70. Dabbousi, B. O.; Murray, C. B.; Rubner, M. F.; Bawendi, M. G., Langmuir-Blodgett Manipulation of Size-Selected CdSe Nanocrystallites. *Chemistry of Materials* 1994, *6* (2), 216-219.

71. Lambert, K.; Čapek, R. K.; Bodnarchuk, M. I.; Kovalenko, M. V.; Van Thourhout, D.; Heiss, W.; Hens, Z., Langmuir−Schaefer Deposition of Quantum Dot Multilayers. *Langmuir* 2010, *26* (11), 7732-7736.

72. Xu, J.; Ji, X.; Gattás-Asfura, K. M.; Wang, C.; Leblanc, R. M., Langmuir and Langmuir–Blodgett films of quantum dots. *Colloids and Surfaces A: Physicochemical and Engineering Aspects* 2006, *284–285* (0), 35-42.

73. Ji, X. J.; Wang, C. S.; Xu, J. M.; Zheng, J. Y.; Gattas-Asfura, K. M.; Leblanc, R. M., Surface chemistry studies of (CdSe)ZnS quantum dots at the air-water interface. *Langmuir* 2005, *21* (12), 5377-5382.

74. Gattás-Asfura, K. M.; Constantine, C. A.; Lynn, M. J.; Thimann, D. A.; Ji, X.; Leblanc, R. M., Characterization and 2D Self-Assembly of CdSe Quantum Dots at the Air−Water Interface. *Journal of the American Chemical Society* 2005, *127* (42), 14640-14646.

75. Sui, G.; Orbulescu, J.; Ji, X.; Gattás-Asfura, K.; Leblanc, R.; Micic, M., Surface Chemistry Studies of Quantum Dots (QDs) Modified with Surfactants. *Journal of Cluster Science* 2003, *14* (2), 123-133.

76. Cordero, S. R.; Carson, P. J.; Estabrook, R. A.; Strouse, G. F.; Buratto, S. K., Photo-Activated Luminescence of CdSe Quantum Dot Monolayers. *The Journal of Physical Chemistry B* 2000, *104* (51), 12137-12142.

77. C. A. Schneider, W. S. R., K. W. Eliceiri, NIH Image to ImageJ: 25 years of image analysis. *Nature Methods* 2012, *9*, 671-675.

78. Stalder, A. F.; Kulik, G.; Sage, D.; Barbieri, L.; Hoffmann, P., A snake-based approach to accurate determination of both contact points and contact angles. *Colloids and Surfaces A: Physicochemical and Engineering Aspects* 2006, *286* (1–3), 92-103.

79. Stalder, A. F.; Melchior, T.; Müller, M.; Sage, D.; Blu, T.; Unser, M., Low-bond axisymmetric drop shape analysis for surface tension and contact angle measurements of sessile drops. *Colloids and Surfaces A: Physicochemical and Engineering Aspects* 2010, *364* (1–3), 72-81.

80. Clapp, A. R.; Goldman, E. R.; Mattoussi, H., Capping of CdSe-ZnS quantum dots with DHLA and subsequent conjugation with proteins. *Nat. Protoc.* 2006, *1* (3), 1258-1266.

81. Rabani, E., Structure and electrostatic properties of passivated CdSe nanocrystals. *J. Chem. Phys.* 2001, *115* (3), 1493-1497.

82. Lee, J. R. I.; Whitley, H. D.; Meulenberg, R. W.; Wolcott, A.; Zhang, J. Z.; Prendergast, D.; Lovingood, D. D.; Strouse, G. F.; Ogitsu, T.; Schwegler, E.; Terminello, L. J.; van Buuren, T., Ligand-Mediated Modification of the Electronic Structure of CdSe Quantum Dots. *Nano Letters* 2012, *12* (6), 2763-2767.

83. Dabbousi, B. O.; Rodriguez-Viejo, J.; Mikulec, F. V.; Heine, J. R.; Mattoussi, H.; Ober, R.; Jensen, K. F.; Bawendi, M. G., (CdSe)ZnS Core−Shell Quantum Dots: Synthesis and Characterization of a Size Series of Highly Luminescent Nanocrystallites. *The Journal of Physical Chemistry B* 1997, *101* (46), 9463-9475.

84. Bädeker, K., The electrical conductivity and the thermal power of some heavy metal compounds. *Annalen der Physik* 1907, *327* (4), 749-766.

85. Granqvist, C. G., Transparent conductive electrodes for electrochromic devices: A review. *Appl. Phys. A* 1993, *57* (1), 19-24.

86. Howson, R. P.; Safi, I.; Hall, G. W.; Danson, N., Sputtering of Indium-Tin Oxide. *Nuclear Instruments and Methods in Physics Research B* 1997, *121*, 96-101.

87. Material Certification Sheet. http://www.lesker.com/newweb/deposition_materials/depositionmaterials_CertForm.cfm?partno=EJTITOX404A4.

88. Ocal, T.; Yusuf, S.; Gulnur, A.; Lutfi, O., High quality ITO thin films grown by dc and RF sputtering without oxygen. *Journal of Physics D: Applied Physics* 2010, *43* (5), 055402.

89. Smits, F. M., Measurement of Sheet Resistivities with the Four-Point Probe. *The Bell System Technical Journal* 1957, 712.

90. Matula, R. A., Electrical Resistivity of Copper, Gold, Palladium and Silver. *J Phys Chem Ref Data* 1979, *8* (4).

91. Kunz T, M. J. R. A. S. K. D. W. U., Adhesion of Ni-structures on Al2O3 ceramic substrates used for the sacrificial layer technique. *Microsystem technologies : sensors, actuators, systems integration* 2000, *6* (4), 121-125.

92. Roy, D.; Basu, P. K.; Raghunathan, P.; Eswaran, S. V., DNQ-novolac photoresists revisited: H-1 and C-13 NMR evidence for a novel photoreaction mechanism. *Magnetic resonance in chemistry* 2003, *41* (2), 84-90.

93. Dammel, R., *Diazonaphthoquinone-based Resists*. SPIE Press: 1993.

94. Crofton, J.; Barnes, P.; Williams, J.; Edmond, J., CONTACT RESISTANCE MEASUREMENTS ON P-TYPE 6H-SIC. *Applied Physics Letters* 1993, *62* (4), 384-386.

95. Shipley, Microposit S1800 Series Photo Resists.

96. Lim Woon Chi, J. Metal Contacts to P-Type Gallium Nitride. National University of Signapore, 2005.

97. Lambert, K.; Dendooven, J.; Detavernier, C.; Hens, Z., Embedding Quantum Dot Monolayers in Al2O3 Using Atomic Layer Deposition. *Chemistry of Materials* 2010, *23* (2), 126-128.

98. Puurunen, R. L., Surface chemistry of atomic layer deposition: A case study for the trimethylaluminum/water process. *Journal of Applied Physics* 2005, *97* (12), 121301-52.

99. Sahu, S.; Majee, S. K.; Pal, A. J., Layer-by-layer assembly of capped CdSe nanoparticles: Electrical bistability and memory phenomenon. *Applied Physics Letters* 2007, *91* (14), 143108-3.

100. Zhao, J.; Bardecker, J. A.; Munro, A. M.; Liu, M. S.; Niu, Y.; Ding, I. K.; Luo, J.; Chen, B.; Jen, A. K. Y.; Ginger, D. S., Efficient CdSe/CdS Quantum Dot Light-Emitting Diodes Using a Thermally Polymerized Hole Transport Layer. *Nano Letters* 2006, *6* (3), 463-467.

101. Coe, S.; Woo, W.-K.; Bawendi, M.; Bulovic, V., Electroluminescence from single monolayers of nanocrystals in molecular organic devices. *Nature* 2002, *420* (6917), 800-803.

102. Kim, L.; Anikeeva, P. O.; Coe-Sullivan, S. A.; Steckel, J. S.; Bawendi, M. G.; Bulović, V., Contact Printing of Quantum Dot Light-Emitting Devices. *Nano Letters* 2008, *8* (12), 4513-4517.

103. Somekh, R. E., The thermalization of energetic atoms during the sputtering process. *Journal of Vacuum Science & Technology A: Vacuum, Surfaces, and Films* 1984, *2* (3), 1285-1291.

104. Rossnagel, S. M., Energetic particle bombardment of films during magnetron sputtering. *Journal of Vacuum Science & Technology A: Vacuum, Surfaces, and Films* 1989, *7* (3), 1025-1029.

105. Lambert, K.; Dendooven, J.; Detavernier, C.; Hens, Z., Embedding Quantum Dot Monolayers in Al2O3 Using Atomic Layer Deposition. *Chemistry of Materials* 2010, *23* (2), 126-128.

APPENDIX A: HIGH PRESSURE LANGMUIR ISOTHERMS

As discussed in Chapter 4, stable isotherms were observed up to 35 mN/m, after which further compression did not appreciably increase the measured surface pressure. Furthermore, no more than 5 methanol rinse cycles were possible before the nanoparticles crashed out of solution due to insufficient ligand coverage. On a few occasions, nanocrystal solutions remained suspended after a sixth rinse. While these solutions were somewhat unstable, on two occasions Langmuir isotherms were measured using them as a spreading solution. Figure A.1 shows these two isotherms. These isotherms appear to show a second collapse pressure at 64-65 mN/m and 22-25 nm^2/QD, values much closer to the expected behavior of these films. These pressures were highly unstable however, collapsing to 35 mN/m (the monolayer pressure for pure TOPO) after 20-30 seconds. This seems to suggest that the more highly rinsed films, while having higher QD concentrations, also have QD populations that are unstable on the water surface, perhaps due to a lack of surface coverage.

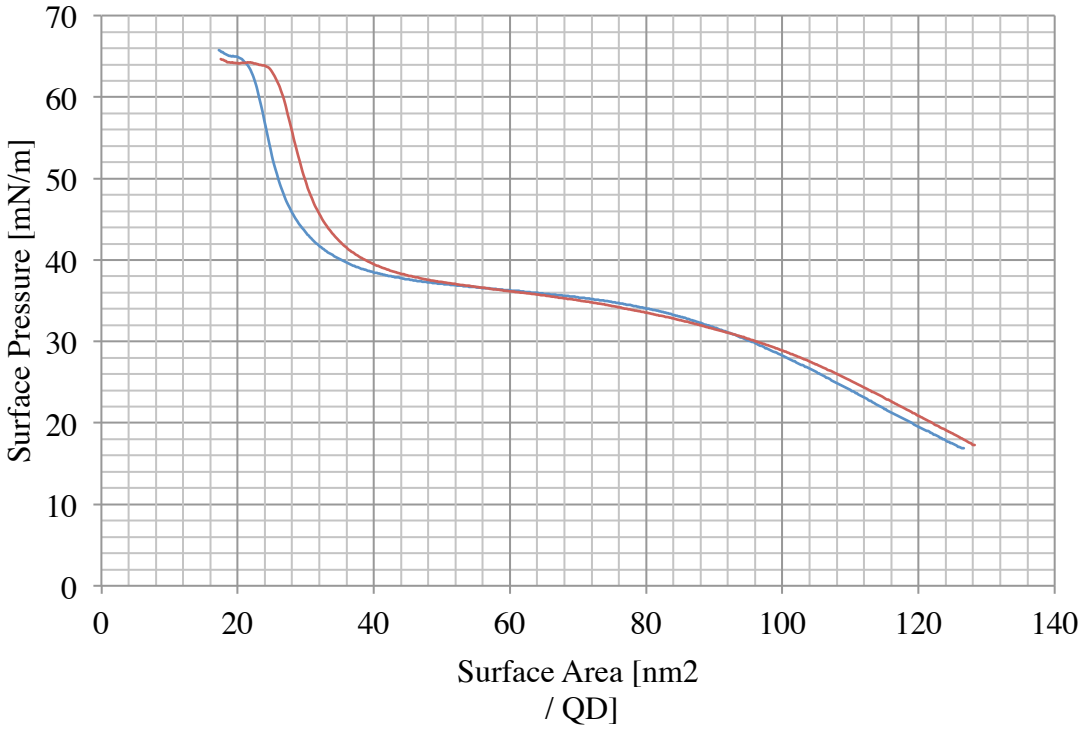

Figure A.1: Langmuir isotherms of TOPO-CdSe QD spreading solutions after six methanol rinse cycles.

APPENDIX B: IN SITU METHANOL RINSING

It became apparent that aggressive rinsing prior to Langmuir film formation was problematic due to insufficient remaining TOPO coverage on the QD surface. That said, free TOPO concentrations remained prohibitively high for film deposition. An approach that allowed for Langmuir film formation with high excess ligand concentration and then removed excess ligands before deposition would be highly desirable. Such an approach, using methanol to rinse the Langmuir films themselves, was explored. In theory the introduction of methanol would solubilize the free TOPO occupying the surface and carry the excess ligand into the water subphase, which methanol is soluble in. The QDs would be unaffected, as they have limited solubility in either methanol or water. Several strategies were pursued, using syringe deposition (similar to how the QD solutions are spread), as well as a misting deposition in order to affect the entire film simultaneously. Furthermore a wide variety of methanol volumes were introduced to these films, from single microliter to 10 milliliter rinses. None of the rinsing procedures had any effect on film properties or isotherms however, which was unexpected.